Fatigue Analysis of a Bicycle Fork

A Major Qualifying Project

Submitted to the Faculty

Of the

WORCESTER POLYTECHNIC INSTITUTE

In Partial Fulfillment of the Requirements for the

Degree of Bachelor of Science

By

_____

Nathaniel A. Jannetti

_____

Bradford L. Lynch

April 29, 2010

_____

Professor Diana A. Lados

_____

Professor James D. Van de Ven

Table of Contents

Table of Figures

Table of Tables

Abstract

Understanding of the heat affected region in welded bicycle forks and proper analysis of the dynamic loading allow for more rapid and effective part design. In addition, the increased demand for lighter bicycle components while maintaining a high level of safety requires an integrated mechanical-metallurgical analysis and validation of a given design and materials-process optimization. This paper presents a methodology for developing the necessary data to enable rapid design iteration of welded bicycle forks that meet current ASTM and CEN standards. Specifically, the paper addresses characterization of the material properties and geometry of the fork, development of a fatigue finite element analysis (FEA), fatigue testing of physical samples in a test fixture, a microstructural fatigue crack growth model to validate the FEA predictions, and ultimately a design iteration leading to an optimal solution. Sectioning of the fork and examining of the microstructure allowed for the identification of the boundaries of the heat affected zone and measurement of local material properties. An FEA model was created utilizing the geometrical characteristics of the fork in combination with the experimentally determined material properties. To validate the model, a testing rig was designed and fabricated to evaluate the forks under dynamic loading. The analytical model and experimental setup are based on the ASTM F2273-03 standard for bending fatigue testing. Further validation of the failure mode/location was completed by fractographically examining the failed forks to determine the crack initiation site and evaluate crack growth rates at various stages. After validation, the FEA model was iteratively used to produce an improved fork design. The proposed methodology can also be used for materials-process design and optimization for performance in bicycle forks or other structural parts and applications.

1 Introduction

1.1 Problem Statement and Motivation

The authors of this Major Qualifying Project are avid cyclists and thus wanted to carry out research related to their passion. Most of the bicycles built today utilize heat treated steel or aluminum or titanium alloy tubing to minimize their weight. The tubes are then welded together to create the desired fork or frame geometry. This welding operation is done at high temperatures, which creates areas of degraded material properties called Heat Affected Zones (HAZ). The analysis and testing of these HAZs are performed in this study.

1.2 Objectives

After seeking out and meeting with several manufacturers of bicycle frames, a Massachusetts based bicycle manufacturer was chosen to serve as the project's industrial partner. The sponsor was selected because of their extensive use of heat treated materials in creating custom frames for both off and on-road riding. The custom frame philosophy is at the heart of the sponsor and truly sets them apart from other high-end manufacturers such as Specialized or Trek. While this principle creates products which are incredibly unique and tailored to their customer's physiology and needs, it does present engineering challenges related to the design, analysis, and testing of their welded products.

Due to their unique approach to building bikes the sponsor is a globally recognized company and serves a wide range of riders from pure recreation to professional mountain bikers. Some customers that were riding their bikes very hard reported cracks forming at the welded joint between the fork blades and steerer tube; the fork and the location of these cracks is detailed in Figure 1-1.

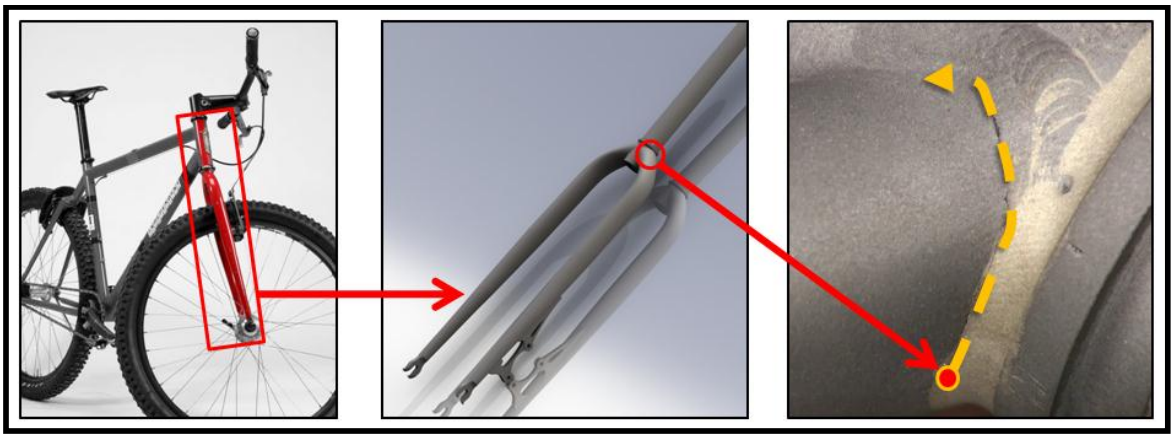

Figure 1-1: Location of the Bicycle Fork, an Isolated Fork, and the Fatigue Crack Location.

The cracks formed in these samples were very small, but indicated to the sponsor that they could improve their design. The project team's first objective was to develop a framework for the design, testing, and analysis of welded tube frames incorporating microstructural analysis of the HAZ, FEA fatigue life modeling, and model validation through experimental fatigue testing. The resulting model can then be used for design optimization. It should be noted that the authors use the word "Frame" here in a general sense referring to any welded load bearing structure. The second objective was to apply this methodology to the sponsor's crack growth problem to devise a solution that would pass ASTM and CEN bending fatigue testing standards.

1.3 Approach and Methodology

The sponsor had observed crack formation during riding and ASTM F2273-03 bending fatigue testing. The first step took by the team was to investigate the fatigue behavior, specifically crack initiation and crack propagation, during loading. Existing forks were then sectioned and the effects of the high temperature welding process on the microstructure of the heat treated materials was characterized for all parts of the fork as shown in Figure 1-2. The geometry of all the pieces was analyzed and used to create a solid model of the fork.

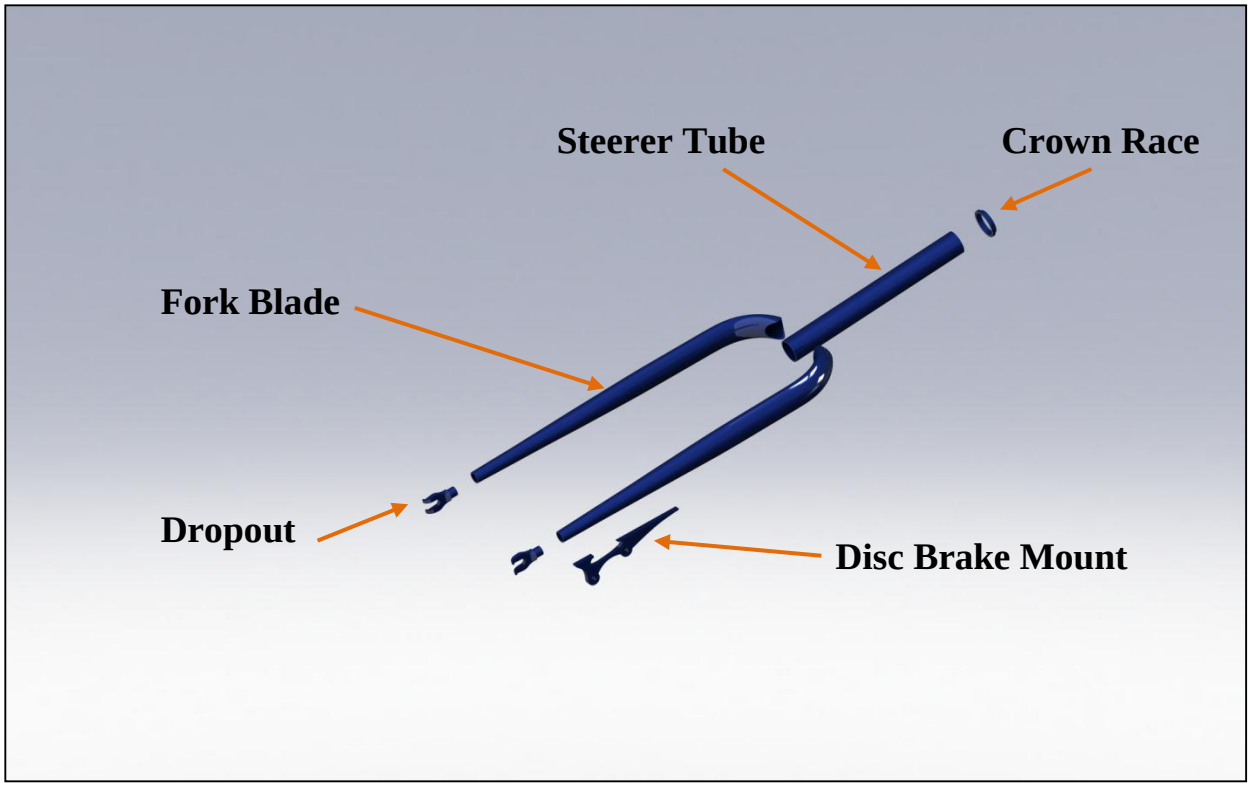

Figure 1-2: The Parts of a Fork Blade.

Investigating the microstructural differences introduced by the welding process allowed the project team to identify the start and end of the heat affected zones. The solid model was then sectioned according to the regions of differing material properties. This geometry was then used to create an ANSYS fatigue life model that incorporated all of the properties that were determined experimentally. Validation of the model through experimental fatigue testing allowed it to serve as a design tool in development of optimized fork geometry, for the sponsor.

2 Materials and Processing Characterization:

The bicycle fork being examined consists of four materials, AISI 4130 chromium-molybdenum (CrMo) steel, AISI 1020 steel, silver brazing filler, and ER70S-2 filler welding wire. AISI 4130 is one of the most commonly used steels in the frame and fork of bicycles. ER70S-2 is also commonly used to weld in aerospace and automotive applications. Determining the actual properties of each material will allow for the creation of an accurate computer model of the fork and realistic failure predictions. Differences in processing are largely accountable for the differences in microstructures, and therefore, mechanical properties. For steel, such as a 4130, with approximately 0.3 wt % carbon, the possible microstructures present, depending on treatment, are ferrite, pearlite, retained austenite, martensite, bainite, or combinations of them. The materials with the properties coming straight from the manufacturer will be discussed followed by an analysis of the Heat Affected Zone (HAZ) that occurs as a result of the welding process done at the bicycle manufacturer.

2.1 Definitions of Processing Terms

Welding: Consists of two materials being melted together and secured using a filler rod. TIG (Tungsten Inert Gas) welding is used to attach all of the pieces made out of AISI 4130. In TIG welding, the weld area is shielded by an inert mixture of gases as well as a deoxidizer. The filler rod can be automatically fed through the nozzle to the weld arc by a small motor. The three types of gas-metal arc welding are spray transfer, globular transfer, and short circuiting (Miller Welds, 2009).

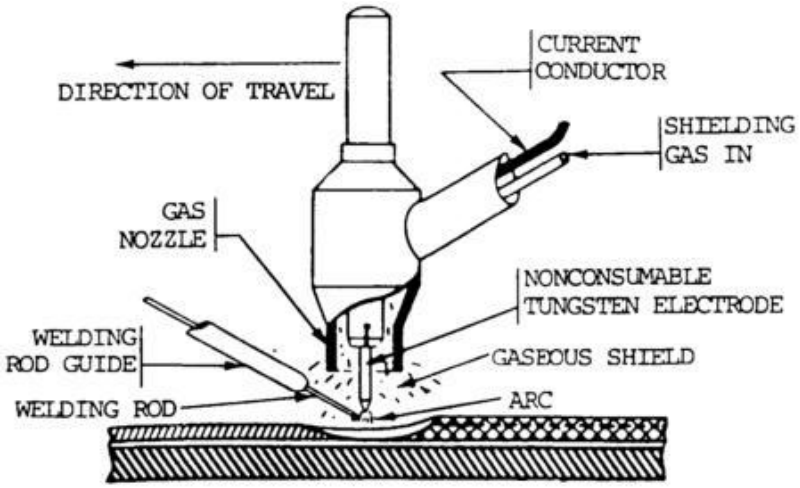

Figure 2-1: Illustration of TIG Welding Technique.

Brazing: A joining process in which a filler metal is placed between two metals and the temperature is raised enough to melt the filler material, but not the other metals. The filler material will solidify and form a relatively strong joint (Lucas-Milhaupt, 2009).

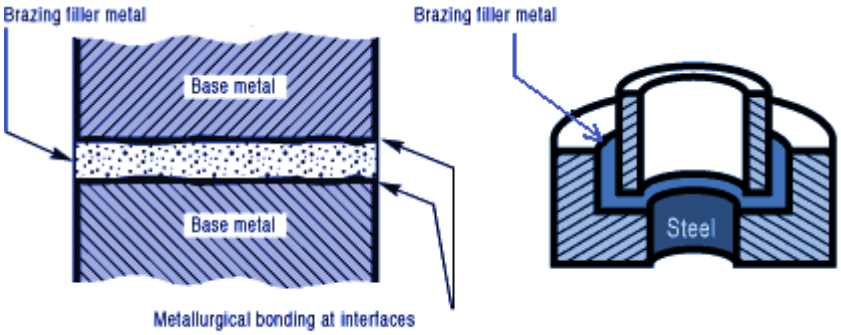

Figure 2-2: Two Metals Being Connected Through Brazing.

Hydroforming: The process of applying fluid pressure inside a tube to obtain a certain shape.

2.2 Fabrication Process

The sponsor has a custom process to make their forks. First, the raw materials from the suppliers arrive, this includes the steerer tubes, fork blades, crown races, quick release dropouts, and brake caliper mounts. The fork blades are then mitered to fit the steerer tubes. Once the steerer tubes and fork blades fit

together properly, based on alignment in a jig, they are TIG welded together. The brake mounts are also welded on at this point in the process. The dropouts are welded to the fork blades and the crown is brazed on. Before these operations can take place, a breather hole is drilled near the end of the fork blades to allow for the escape of expanding air during the welding and brazing process. The forks are then tested for alignment on a special in-shop fabricated fixture. If they meet the requirements they are then primed and painted. Figure 2-4 outlines the entire treatment and assembly.

Figure 2-3 : Fabrication Process. From Left to Right: Fork Blades Arrive in Box, Steerer Tubes Arrive in Box, Parts are Welded, Forks are Primed and Painted.

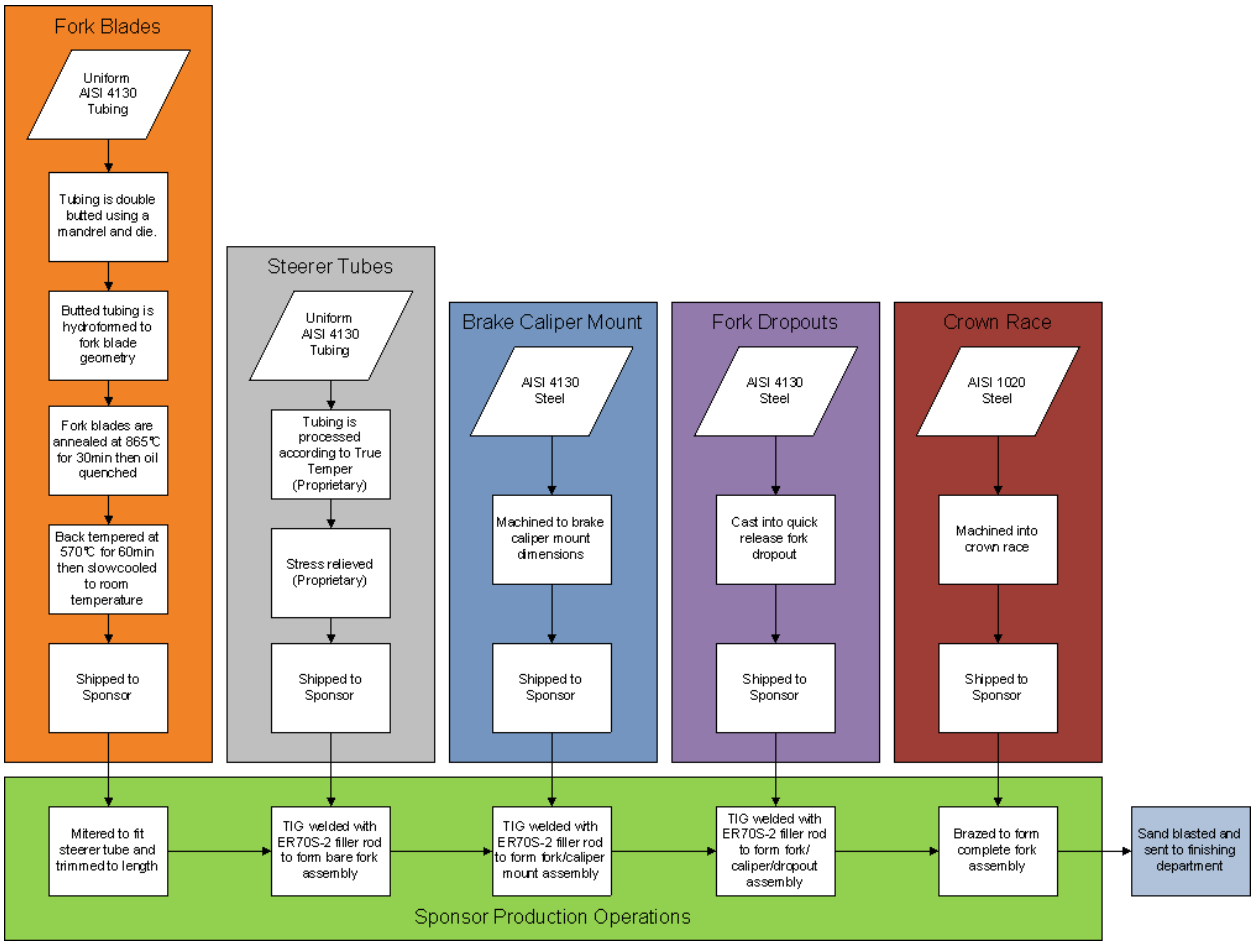

Figure 2-4: Process Flow Chart.

2.3 Testing Procedure

After all the processing information was gathered, it was necessary to conduct physical tests and calculations to see how these different processes impacted the mechanical properties of the materials. For these tests, samples were prepared to reveal the microstructural changes and the characteristic features on the area where the fork had been fracturing. The samples were then prepared, working from a very coarse grit on the grinder to a very fine (0.01µm) grit using the polishing wheels. The samples were then etched using a solution of nitric acid and alcohol (Nital 2%), submerged for 10-15 seconds while being swirled around. Then the samples were examined under the optical microscope to analyze the microstructure and locate and examine the fracture. The results are discussed for each material in the subsequent sections. After the optical microscopy, Knoop microhardness (HK) was taken in each region. Since the materials

were processed differently (for complete process diagram see Figure 2-4), microhardness values were different too. These results, along with the information on processing procedure allowed for a characterization of the materials that were given limited information by the manufacturer, such as the True Temper steerer tube and the crown race. Microhardness values were converted into Vickers hardness and Brinell hardness (HB) using tables and online converters (Efunda, 2010) and then used to calculate the ultimate tensile strength by using the equation below where UTS is the ultimate tensile strength and HB is the Brinell hardness of the material (Callister, 2007).

$$UTS = 3.45HB$$

The SEM was then used to observe the phases in each region. The steerer tube, fork blade, crown, and brazing filler were all examined. EDS tests were also conducted at that time. Samples of the steerer tube and fork blades were bent flat and polished enough to allow multiple spectrographs to be taken. For full results of the spectrographs see Appendix D. X-ray diffraction testing was performed on the welded region, and the results are presented in Appendix E. All the experimental results were introduced into the CAD model and used to create a realistic FEA. Information that was not found experimentally or discrepancies that were found between experimental data and the data supplied by the manufacturer are also noted in the sections below.

2.4 Fork Blades

Material

The fork blades are made out of AISI 4130 Steel, known by the supplier as Reynolds 725 (Reynolds Technology Ltd., 2009). The fork blades are formed to shape by double butting and then hydroforming.

Composition

Figure 2-5 shows the experimental results from the spectrograph compared with the typical range of a 4130 steel. From the chart it is shown that the experimental spectrograph results are not far from specifications.

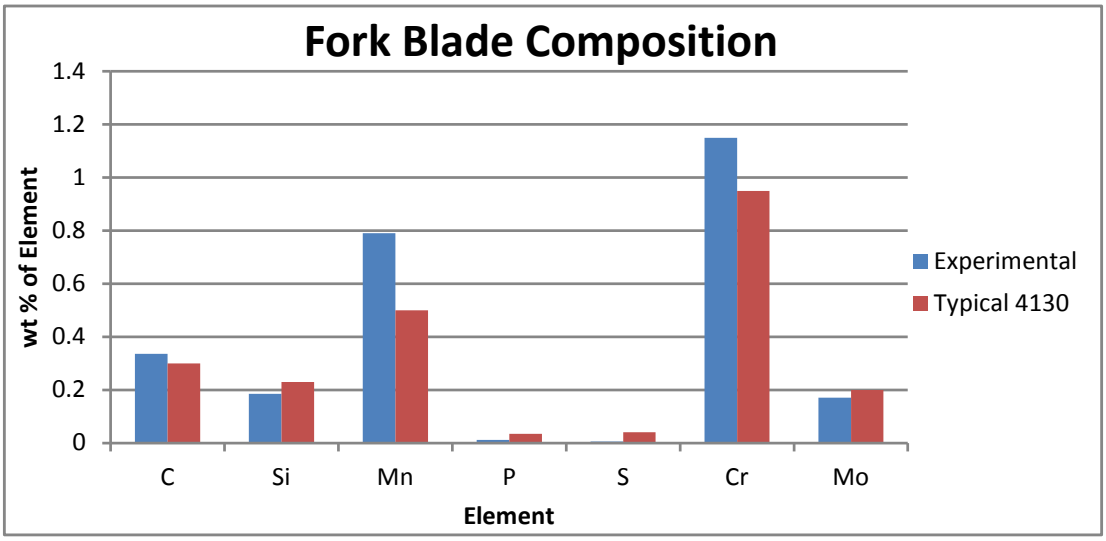

Figure 2-5: Spectrograph of the Fork Blade.

Heat Treatment and Microstructure

The 4130 steel was heat treated and the resulting microstructure is shown in Figure 2-6. The heat treatment was done as follows:

- Heat to a temperature of 865°C for 30 minutes in a controlled atmosphere to avoid decarburization
- Quench in oil to harden the alloy
- Back temper at 570°C for 60 minutes
- Air cool the alloy back to room temperature

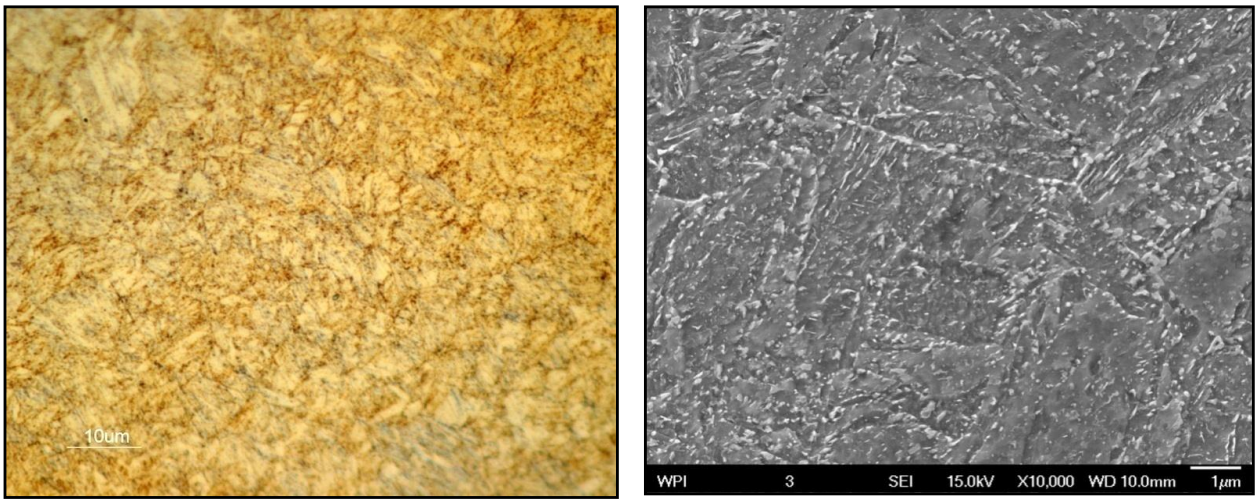

Figure 2-6: Optical (left) and SEM (right) Micrographs of the Fork Blade Material.

The microstructure of the material consists of tempered martensite with small areas of pearlite. The martensitic structure is created when the steel is heated into the austenite zone and then quenched through

a diffusionless transformation (see Appendix F for the Fe-C phase diagram). Back tempering allows some of the carbon to diffuse, forming areas of pearlite. Tempering will restore ductility, but slightly decrease the tensile strength (Kalpakjian & Schmid, 2006).

Mechanical Properties

To determine UTS values from the dropout to the heat affected zone, the fork was sectioned into the pieces shown below in Figure 2-7. An average microhardness value was taken at each piece. Figure 2-8 shows the UTS across the fork blade calculated from the microhardness values. Region 1 is the dropout and Region 7 is the area adjacent to the heat affected zone. The other regions are equally spaced along the fork blade.

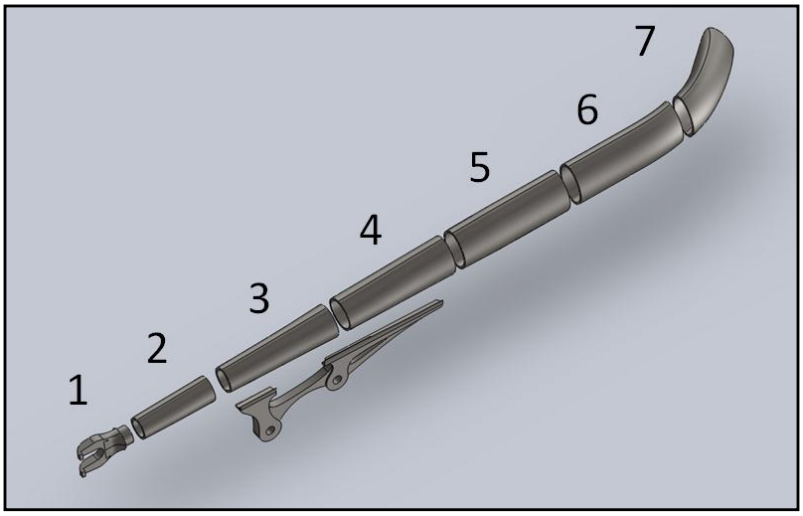

Figure 2-7: Numbered Regions of the Fork Blade.

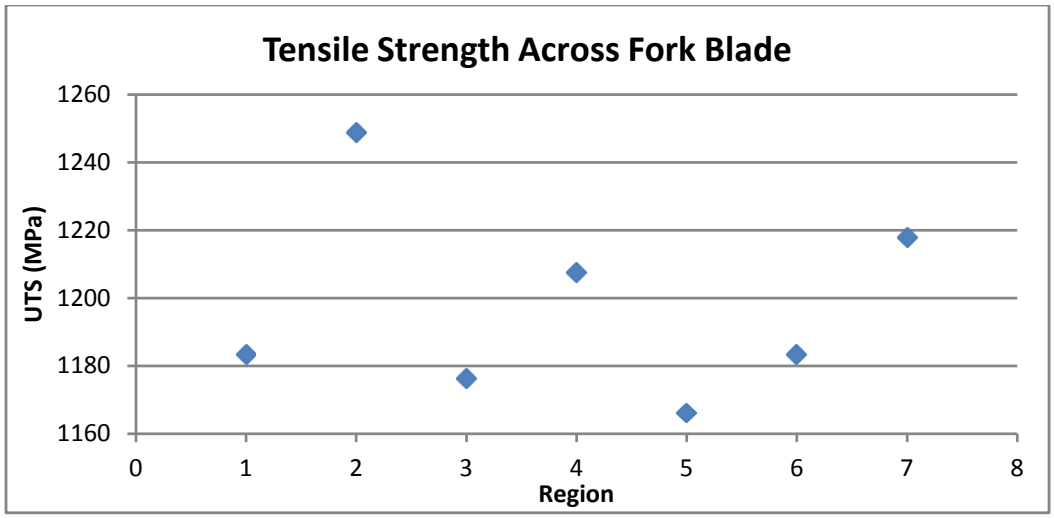

Figure 2-8: Graph of Tensile Strength across the Fork Blade.

Table 2-1: Mechanical Properties of Fork Blades.

Average Hardness	367 HV
Standard Deviation	9.2 HV
Ultimate Tensile Strength	1197 MPa
Yield Strength	800 MPa
Elastic Modulus	201-216 GPa
Percent Elongation	8 %
Poisson's Ratio	0.34

The mechanical properties in Table 2-1 show the experimental results such as the hardness and tensile strength merged with properties supplied by Reynolds. Reynolds specifies minimum mechanical properties in their documentation for this material. The experimental results show that these fork blades are within specification because all properties are greater than the minimum values.

2.5 Steerer Tube

Material

The steerer tube is made out of AISI 4130 steel manufactured by True Temper. The True Temper name for the steel is Versus Steel, and it is formed using a proprietary technique (True Temper Sports, 2009).

Composition

Below are the experimental results from the spectrograph compared with the typical range of a 4130 steel.

Expanded results can be found in Appendix D.

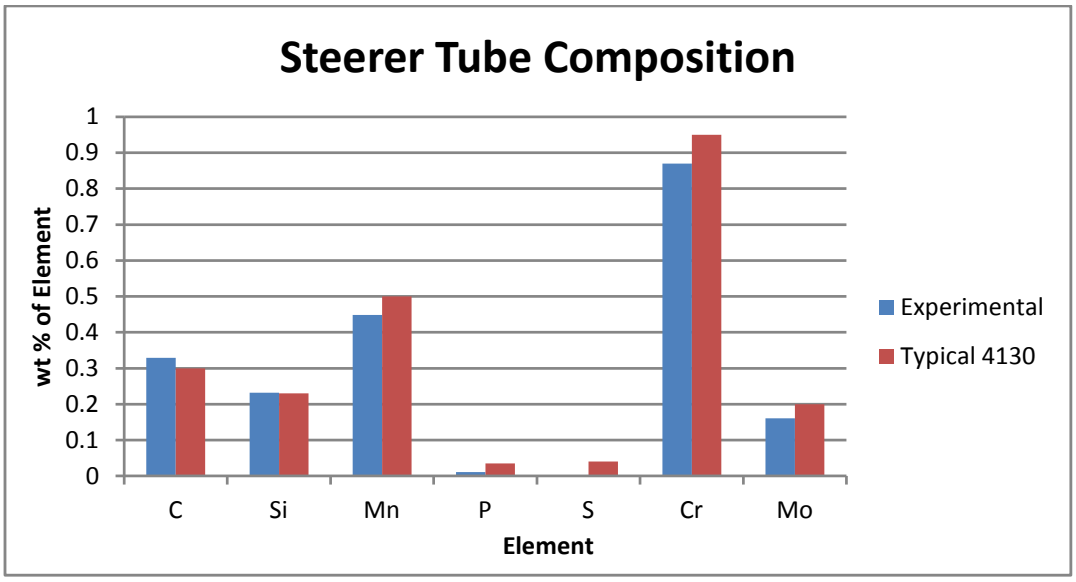

Figure 2-9: Spectrograph Results for the Steerer Tube.

Heat Treatment and Microstructure

The cold worked True Temper 4130 steel is treated by stress relieving. The exact method of stress relieving is a proprietary technique from True Temper. This treatment produces the microstructure shown below in Figure 2-10.

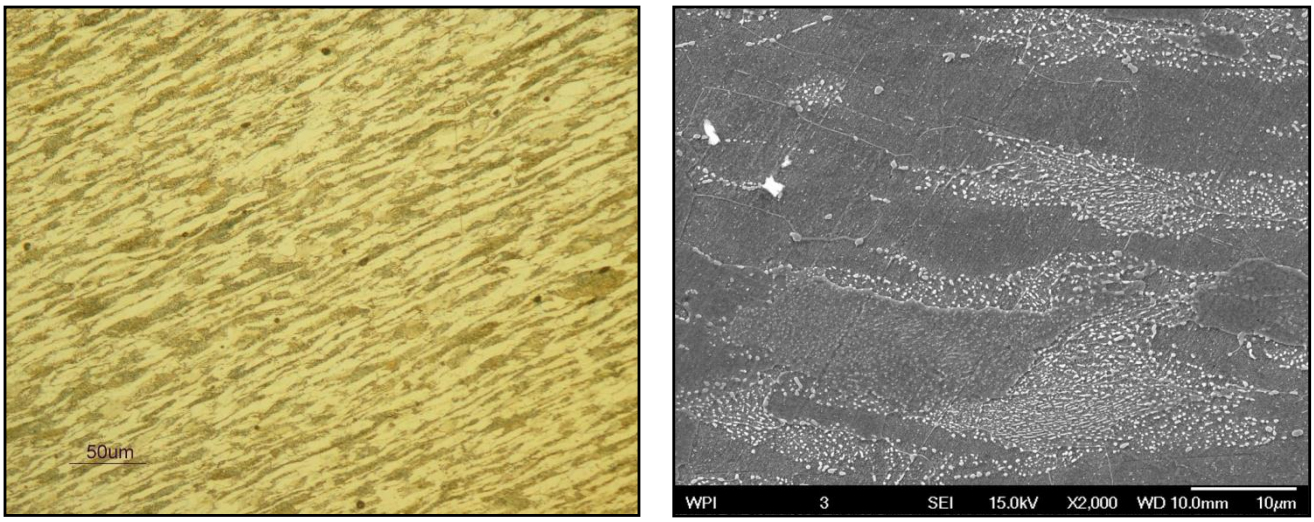

Figure 2-10: Optical (left) and SEM (right) Micrographs of the Steerer Tube Material.

The material above is proeutectoid ferrite and pearlite. The proeutectoid ferrite is the plain dark grey areas in the SEM image. Pearlite is a mixture of ferrite and cementite, the lighter regions in the SEM micrograph.

Mechanical Properties

Because True Temper uses a proprietary treatment process, it was necessary to find the closest mechanical properties from the information that was provided. Information on cold worked 4130 was not available, so using CES Edupack 2009, a steel with possible similar mechanical properties was selected. This steel was "Low alloy steel, AISI 4130, tempered at 650°C and H_2O quenched". Table 2-2 shows typical mechanical properties for 4130 steels together with the experimental hardness and calculated ultimate tensile strength values.

Table 2-2: Mechanical Properties of Steerer Tube.

Average Hardness	285 HV
Standard Deviation	14.22 HV
Tensile Strength	931 MPa
E	201-216 GPa
Shear modulus	77-85 GPa
Elongation	17-27 %
Poisson	0.285-0.295

Microhardness testing indicated a HV of 213 near the end of the steerer tube heat affected zone. Calculating the UTS based on this microhardness gives a value of 697 MPa. These values are in the expected range of the hardness and the UTS values provided by True Temper, and are significantly different from those outside the cracking area because of the cold work.

2.6 Crown Race

Material

AISI 1020 Steel- Paragon Machine Works

Composition

A spectrograph was not possible due to the small size of the crown race. In order to obtain the percent of proeutectoid ferrite and pearlite an image analysis was performed using Adobe Photoshop CS3. According to MatWeb, cold worked 1020 steel typically has a range of 0.17-0.23% of carbon. This leads to 70-80% proeutectoid ferrite. Image analysis resulted in approximately 65% of proeutectoid ferrite, which is a reasonable agreement.

Treatment and Microstructure

The manufacturer of the crown race uses different 1020 steels and was not able to provide information on how the steel was treated before machining. By examining the microstructure of the steel it is likely that the steel was cold worked and then machined from a solid block of 1020 steel. Figure 2-11 shows the micrographs of the crown race.

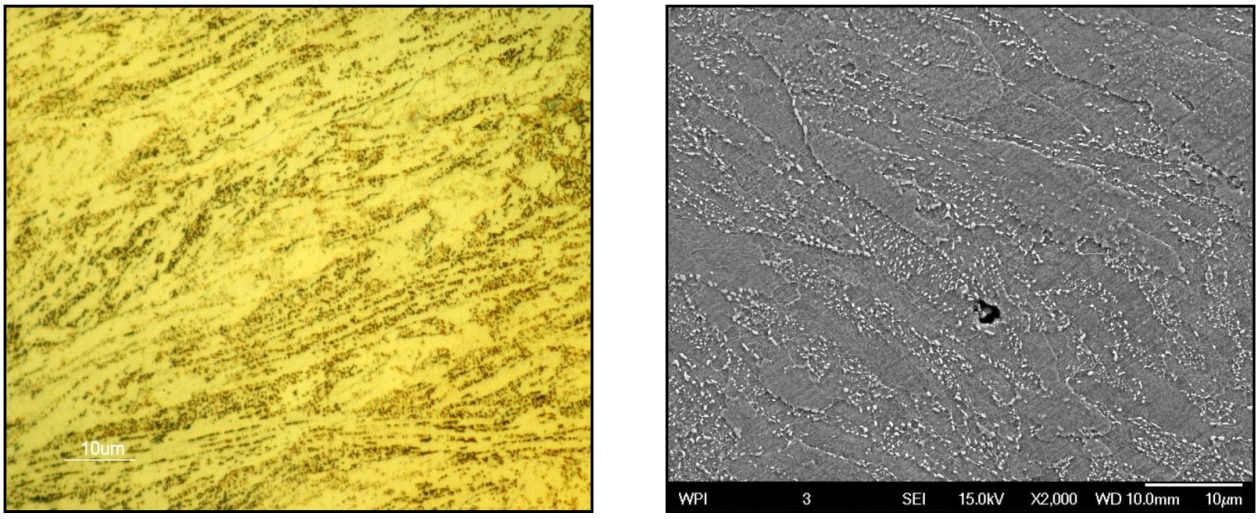

Figure 2-11: Optical (left) and SEM (right) Micrographs of the Crown Race Material.

The microstructure consists of proeutectoid ferrite and pearlite. On the SEM micrograph, the proeutectoid ferrite is the plain dark grey areas and pearlite is a mixture of ferrite and cementite (the lighter regions).

Mechanical Properties

Table 2-3: Mechanical Properties of Crown Race.

Average Hardness	239 HV
Standard Deviation	10.7 HV
Tensile Strength	783 MPa
E	205-215 GPa
Elongation	24 %
Poisson	0.29

Table 2-3 shows the mechanical properties for the crown race. The hardness and UTS were determined experimentally. The elastic modulus, percent elongation, and Poisson Ratio were found in materials databases. The experimental properties matched the minimum specifications given by the manufacturer. However, Paragon Machine Works indicated that the properties will vary slightly between batches and sometimes they substitute AISI 1018 steel for the 1020.

The treatment process for the 1020 steel significantly increases the yield and ultimate tensile strength. According to CES Edupack and MatWeb, the average yield strength for a regular cold rolled AISI 1020 steel is 350 MPa and tensile strength is 420 MPa compared to the experimentally determined tensile strength of 776 MPa. However, the measured UTS matched closely the value provided by Paragon Machine Works.

2.7 Welding Wire

Material

ER70S-2

This is a manufactured material and does not need to be treated as it serves to connect the different parts of the fork.

Composition and Mechanical Properties

Table 2-4 comparing the composition of a generic 4130 steel to the ER70S-2 welding wire.

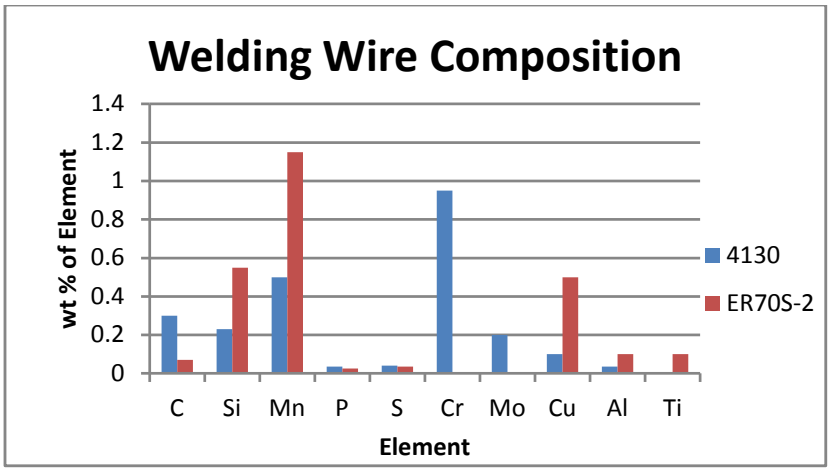

Figure 2-12: Spectrograph Results for the Welding Wire.

The general material properties of ER70S-2 are listed in Table 2-4. The welding wire becomes fused with the other metal, so these properties generally change after welding.

Table 2-4: Mechanical Properties of Welding Wire.

Ultimate Tensile Strength	552 MPa
Yield Strength	450 MPa
Percent Elongation (2")	25 %

2.8 Brazing Filler Metal

The brazing filler metal is extremely soft compared to the metals around it such as the crown race, fork blades, and steerer tube. The material used for this brazing is Harris Safety-Silv 56 brazing filler material (The Harris Products Group). The composition is shown in Table 2-5. The SEM image in Figure 2-13 shows the porous nature of the brazing filler that decreases its microhardness. The microhardness of the brazing filler is less than half of the crown race, steerer tube, and fork blades that it is attached to.

Table 2-5: Composition of the Brazing Filler.

Silver	55-57 %
Copper	21-23 %
Zinc	15-19 %
Tin	4.5-5.5%
Other Totals	0.15%

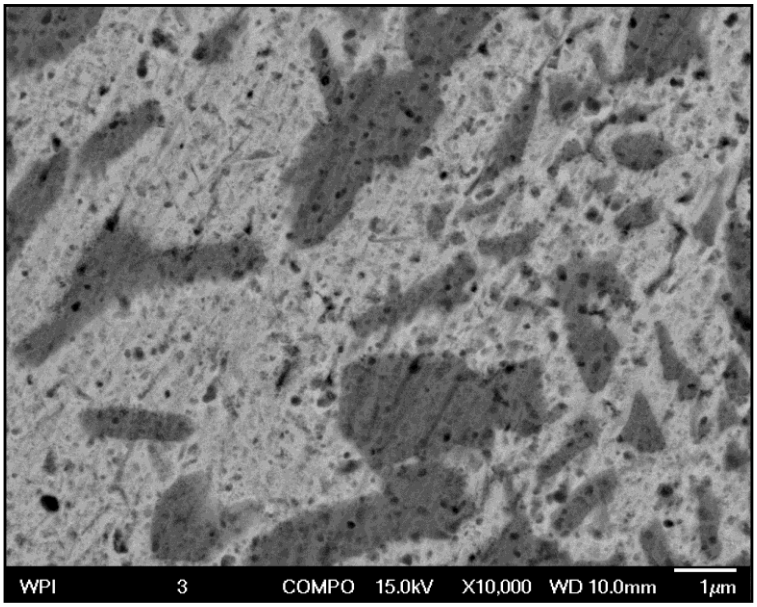

Figure 2-13: Micrograph of the Brazed Region.

2.9 Dropout and Disc Brake Caliper Mount

Given their position in the fork the dropout and the disc brake caliper mount were not analyzed to the extent of the materials that converge in the region where the crack is forming. Both the dropout and the disc brake caliper mount are made of AISI 4130. The dropout is cast, while the disc brake caliper mount is machined from a solid block of the cast metal. The microstructure consists of ferrite and pearlite and the experimentally determined mechanical properties are listed in Table 2-6. Samples did not have spectrographs taken.

Table 2-6: Mechanical Properties of Disc Brake Caliper Mount and Dropout.

Disc Brake Caliper Mount	
Average Hardness	247 HV
Standard Deviation	27 HV
Ultimate Tensile Strength	811 MPa
Dropout	
Average Vickers	215 HV
Standard Deviation	4.2 HV
Ultimate Tensile Strength	700 MPa

2.10 Analysis of the Weld and Heat Affected Zone

The research found in regards to the cause of premature failure in welded tube frames indicated that the welding process itself can be detrimental to the fatigue life of the fork. When welding the fork blades to the steerer tube, very high temperatures are reached from the welding torch. These temperatures can often be tens-of-thousands of degrees Fahrenheit. This heating, along with varying cooling rates can create different microstructures, which can significantly change the mechanical properties of the materials in the region (ASM International, 1990). Figure 2-14 shows the Fe-C phase diagram and how varying temperature can create a difference in grain size and microstructure. The region between the weld material and the material that was not affected by heating is known as the Heat Affected Zone and is referred to as the HAZ in this report. The base material that was not affected by the weld's heat will be referred to as unaffected material. Section 2.2 discusses the welding and assembly processes that the bicycle manufacturer uses to assemble the forks. The HAZ has the greatest potential to become a point of failure due to the unpredictability of the welds and the resulting microstructures.

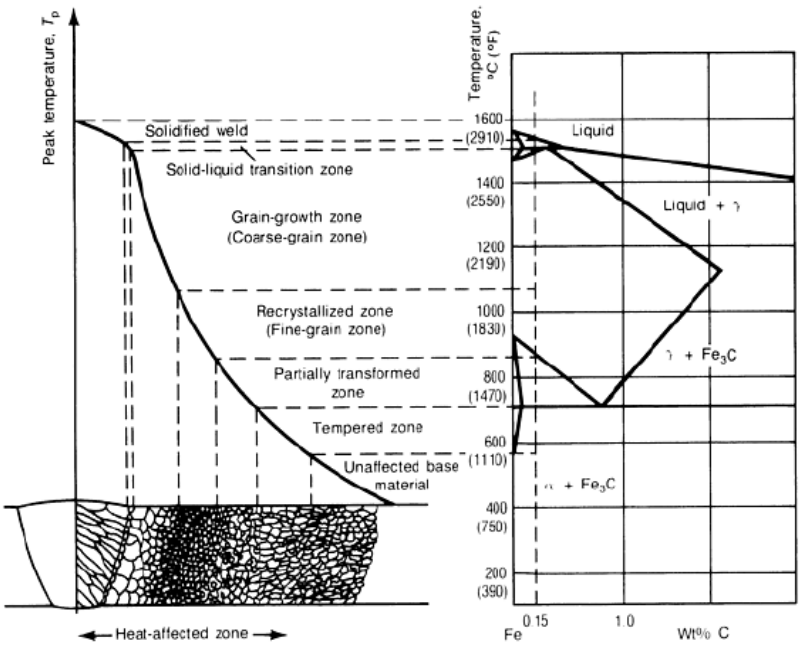

Figure 2-14: HAZ Relationship to the Steel Phase Diagram.

2.10.1 The Regions of the HAZ

Figure 2-15 shows all regions of the heat affected zone. A higher resolution image of Figure 2-15 can be found in Appendix B. Figure 2-15 represents a section across the weld where the fork blade is welded to the steerer tube; its location can be seen in Figure 2-16. The brazing filler metal and the crown race have been masked in order emphasize the fork blade-steerer tube weld region. Due to the welding, distinct regions have developed between the weld and the unaffected materials, which can be seen in both Figures Figure **2-14** and Figure **2-15**. Close to the weld there is an area of large grains; the grains become finer until the unaffected material is reached.

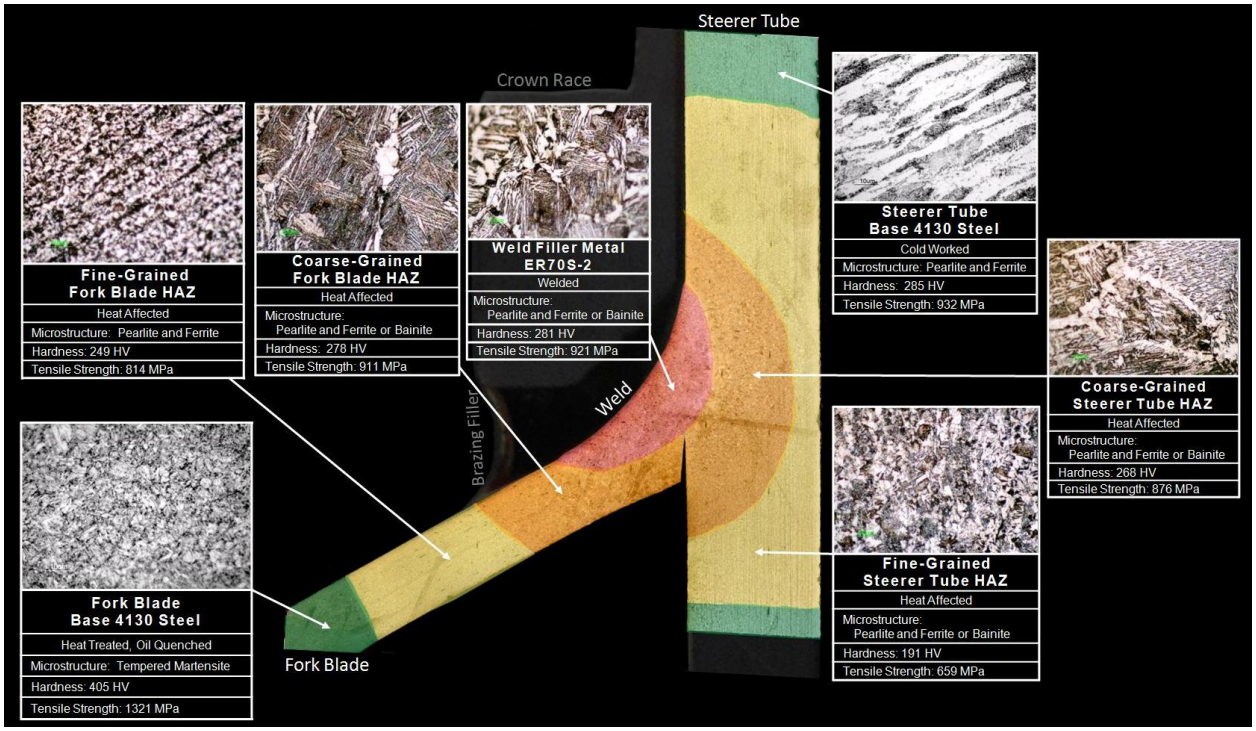

Figure 2-15: Areas of HAZ: Weld (Red), Coarse-Grained HAZ (Orange), Fine-Grained HAZ (Yellow), Unaffected Materials (Green).

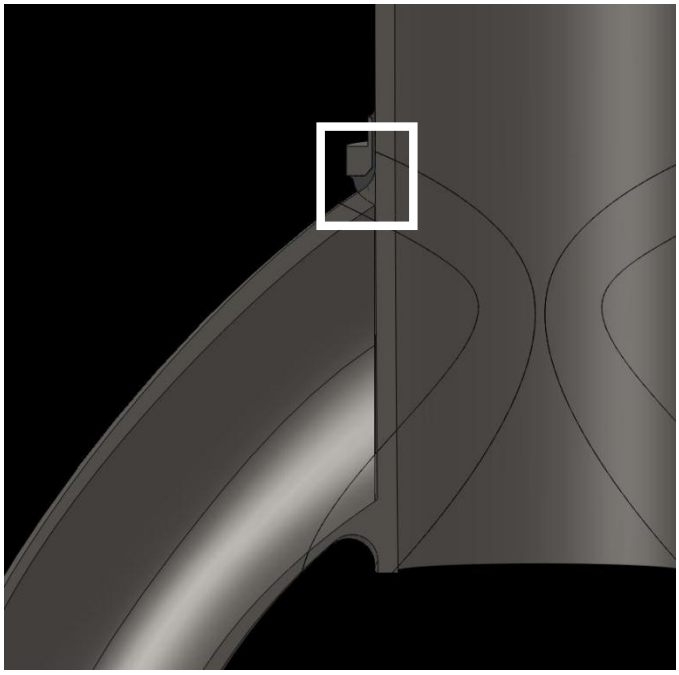

Figure 2-16: Location of sample with HAZ analyzed.

In Figure 2-15 the weld is colored red, the heat affected zone with coarse grains is orange, the heat affected zone with finer grains is yellow, and the unaffected materials are green. Because the steerer tube and the fork blades were treated differently before the welding, the mechanical properties differ between the two, although similar trends were observed in both. This is because of the differences in microstructure that can be seen in the green areas of the map. The pearlite and proeutectoid ferrite microstructure of the steerer tube is not as hard as the tempered martensitic structure of the fork blades. The welding process can introduce various microstructures based on the rate at which the weld and heat affected zone are cooled. It was determined that the HAZ contained a mixture of pearlite and proeutectoid ferrite. The pearlite and proeutectoid ferrite were formed during the slow cooling of the weld. Microhardness measurements were taken across the HAZs for the fork blade and for the steerer tube in order to determine proper tensile strength values to use in the FEA. Areas with low microhardness values are soft and therefore have a low ultimate tensile strength. The graphs in Figures

Figure **2-17** and Figure **2-18** show the changes in ultimate tensile strength from the weld across the heat affected zone for the fork blade and steerer tube.

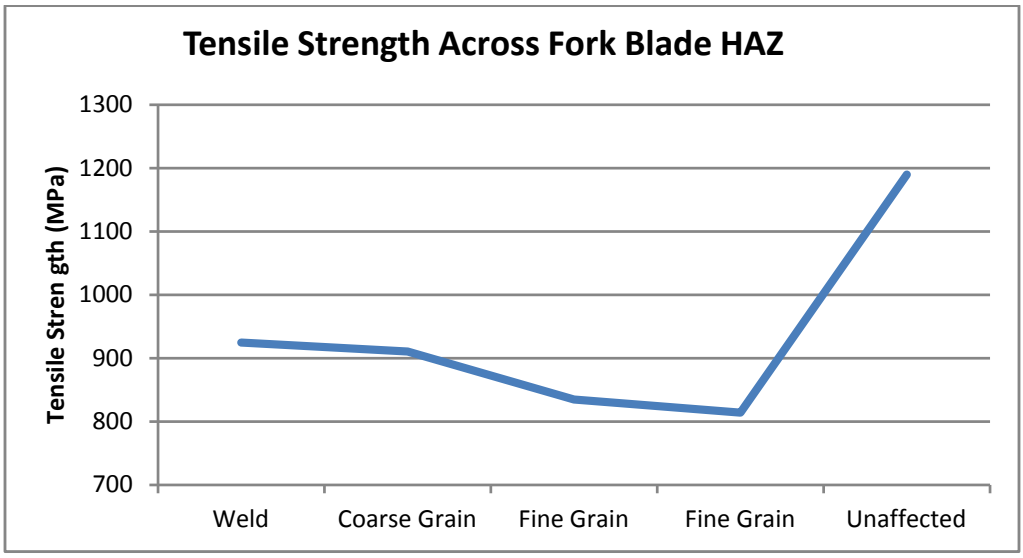

Figure 2-17: Tensile Strength Across the Fork Blade HAZ.

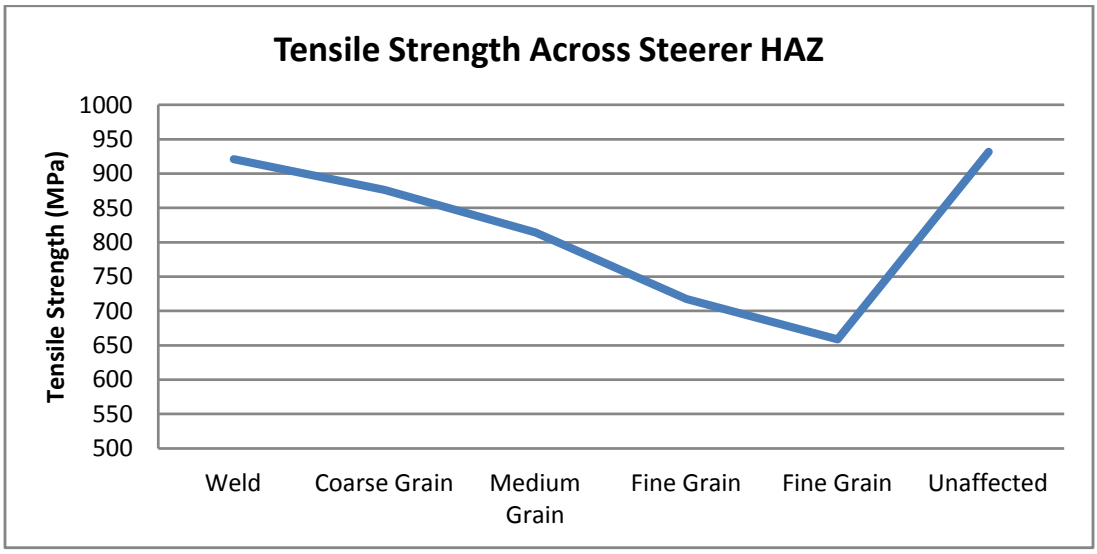

Figure 2-18: Tensile Strength Across the Steerer HAZ.

Figure 2-19 is a sample of the front face of the fork showcasing sections through the welds. Because of the way the sample is sectioned, the fine-grained heat affected zone of the fork blade is not shown, however, the graph (Figure 2-20) shows the transition into the fine grain steerer tube heat affected zone at

point 6, which shows the lowest tensile strength. The results verify those from the literature in that materials will decrease in strength from the weld into the heat affected zones. The conditions of the welding can drastically influence the ultimate tensile strength, although this is a typical trend. Degraded properties in these areas in conjunction with high over-imposed stresses can result in crack initiation and crack propagation under dynamic loading.

Figure 2-19: Sample of the Front of Fork with Regions Labeled.

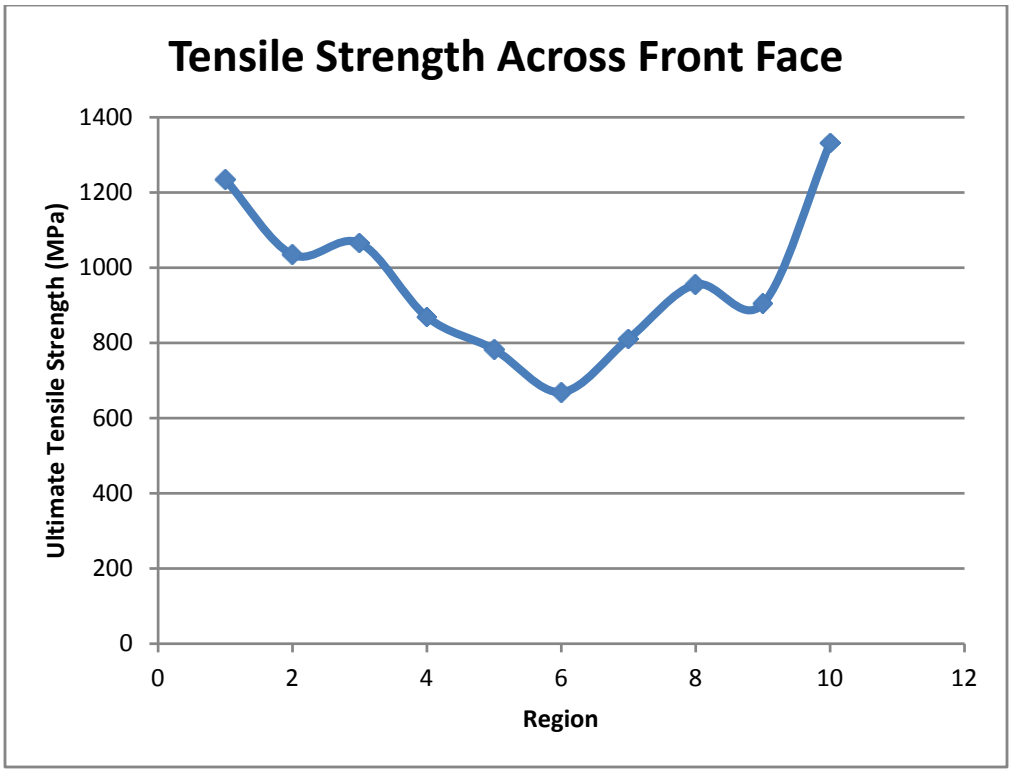

Figure 2-20: Tensile Strength Across Front Face with Welds.

3 Geometry Characterization

3.1 Preliminary Model

3.1.1 Fork Blade Modeling Procedure

3.1.1.1 Understanding the Geometry

The sponsor provided the MQP team with two forks that had been returned to them by customers for inspection. The first step in understanding the geometric contributions to the stress crack formation was to accurately model the bicycle fork geometry. Due to the complex swept surface and variable material thickness of the fork blade, annotations were made along the length of the blade and measurements were taken at each point.

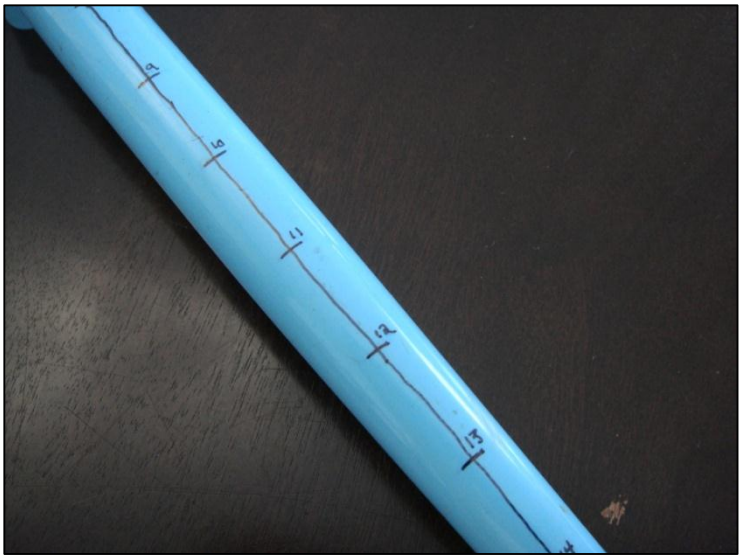

Figure 3-1: Annotated Fork.

The primary design features that needed to be characterized were the cross-section as it changed along the length of the blade, the length of the blades, and the draft angle at which the blades were aligned with respect to the steering tube axis. The approach to this modeling problem was to look at the fork from the front and from the side and input the measured geometry. SolidWorks was chosen as the CAD package to build the model and a 3D sketch was created. A circle to represent the steerer tube was inserted into the sketch and a centerline was created to serve as the steering tube axis. The steering tube axis was assumed to be equidistant from the inner and outer silhouettes of the fork blades. This allowed for the measurements D1 and D2 to be taken and then dividing by two gives the distance of the steering tube axis to the inner and outer silhouettes, respectively. The centerline and left and right silhouettes of the fork blade were inserted into the sketch as splines. These were inserted to use as guides during the creation of the lofted fork blade surface. These measurements were taken every inch for the complex areas of the geometry resulting in the sketch in Figure 3-2.

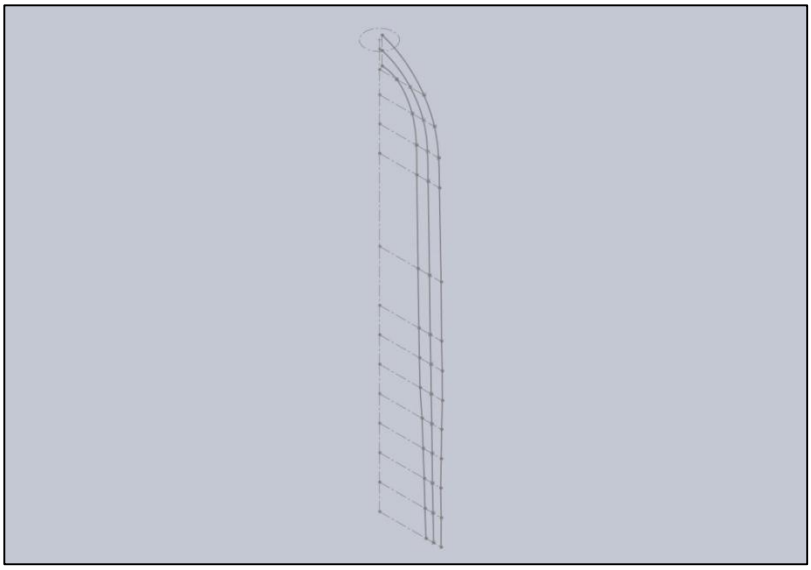

Figure 3-2: Sketch of Fork Geometry in the Front Plane.

The next step was to take measurements from the side view of the fork to characterize the changes occurring in the fork blade profile in the side plane. The width of the fork blade was measured at each plane where measurements had been made in the front plane and inserted into the sketch. More guides were created by representing the front and back silhouettes with splines, resulting in the following sketch in Figure 3-3.

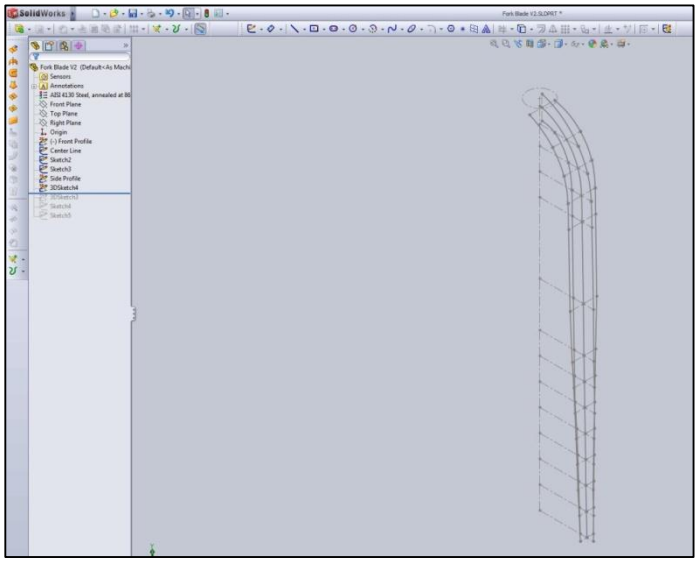

Figure 3-3: 3D Sketch with Geometry from the Side View.

The exact geometry of the cross-section at each spot was not known, only the four points correlating to the width of the fork blade in the front and side planes. Nothing was known about the curvature of the surface between those points. Since this model was created as a preliminary representation of the fork to aid in understanding the problem at hand it was determined that a relaxed spline connecting the four points was an adequate representation of the studied geometry. The resulting sketch is shown in Figure 3-4.

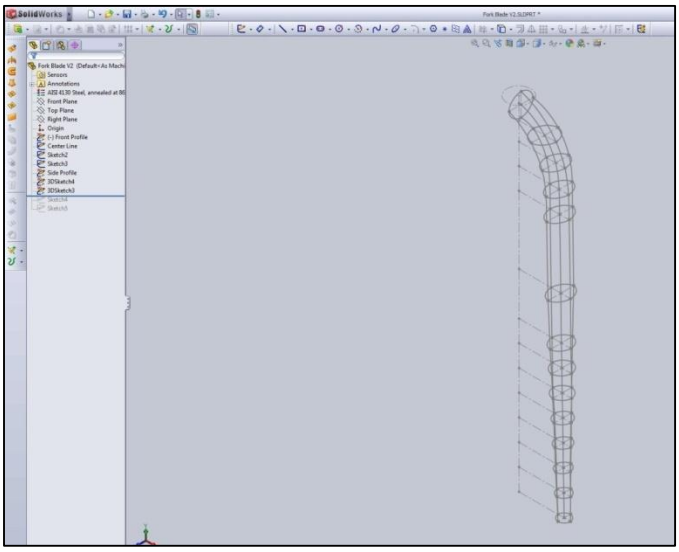

Figure 3-4: 3D Sketch with Cross-sectional Geometry.

3.1.1.2 Creation of the Translated Fork Blade

Now that the geometry was in the CAD model, the next step was to create a solid model to represent the fork blade. Since all of the points were measured from the outer surface of the fork blade a lofted surface was created to represent that geometry. The surface was lofted using each of the relaxed splines representing the cross-sectional geometry using the splines that represent the fork blade silhouettes as guides to eliminate any twist along the loft. The next step was to create an offset surface from the outer surface that would represent the inside of the fork blade. The fork blade was cut up into several pieces and the thickness at each section was measured. Using these data, an accurate representation of the fork blade wall thickness was created. The

two surfaces needed to be joined together in order to create a solid model of the fork blade. At each end of the blade a fill surface feature was created and the geometry was closed to create a solid body. The next step was to cut the fork blade at the top so that it would mate to the steerer tube. The left and right fork blades have the same geometry before cutting. But, since their axes are at some angle α off of the steering tube axis, when viewed from the side plane, two models were created. A plane was created at the top of the fork blade and oriented at α from the top plane about the X-Axis. The only difference between the right and left fork blade models is the direction in which the plane is rotated about the X-Axis, CCW and CW respectively. The fork blade was then cut with a circle of the same diameter as the steering tube sketched on this plane. Figure 3-5 visually depicts this process and the outputs generated from the CAD package throughout each step of the modeling course.

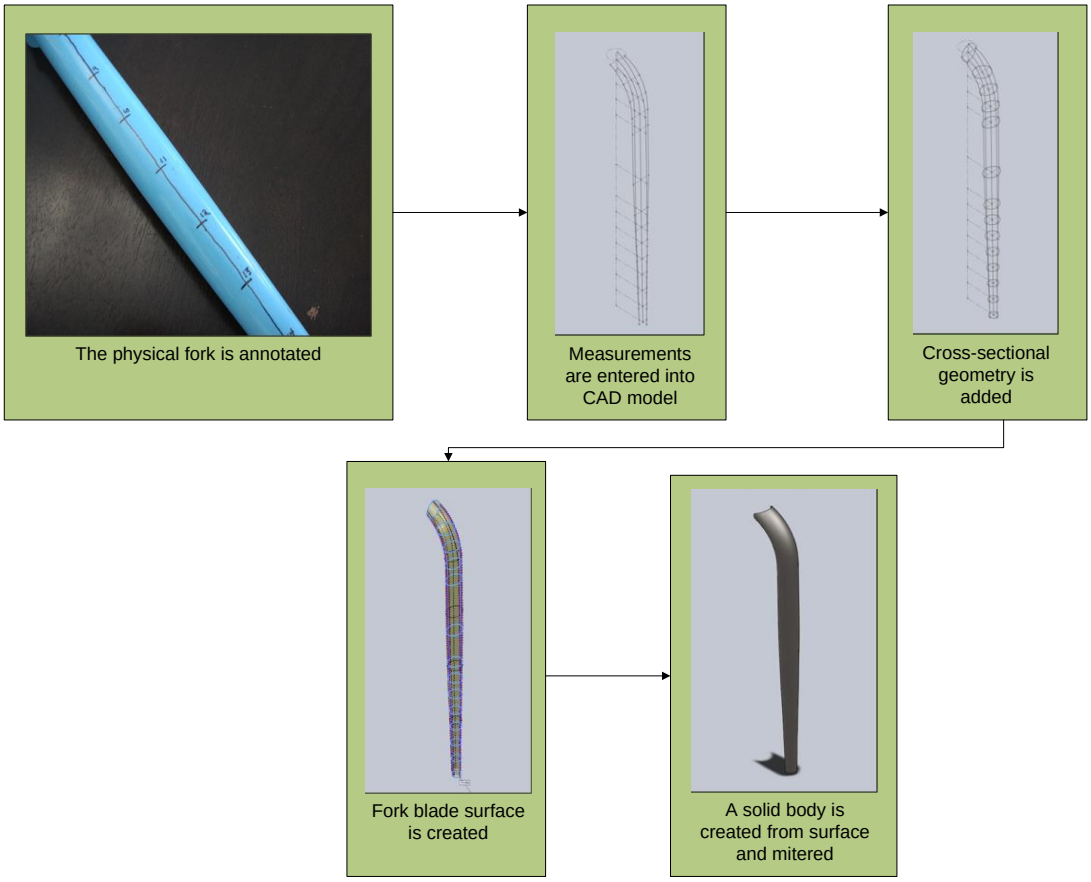

Figure 3-5: Fork Blade Modeling Process.

3.1.2 Steerer Tube Modeling Procedure

The steerer tube was modeled by creating a sketch with two concentric circles. The measured inner diameter of the steerer tube was used as the diameter for the inside circle on the sketch. The outside circle on the sketch was assigned the value of the measured outer diameter of the steerer tube. The tube was then extruded to the appropriate measured length.

3.1.3 Crown Modeling Procedure

The crown was modeled by creating a sketch with two concentric circles. The diameter of the inner circle was assigned the value of the outer diameter on the steerer tube. The diameter of the outer circle of the crown was measured using calipers. The sketch was then extruded to a measured value to create a small tube.

3.1.4 Disc Brake Mount Modeling Procedure

Due to the fact that the features on the disc brake mount were relatively complex, a photograph of the mount was used to ensure the proper scale and geometry of the splines. The picture was taken perpendicular to the face of the most complex side of the mount. First, the image of the mount was imported into SolidWorks.

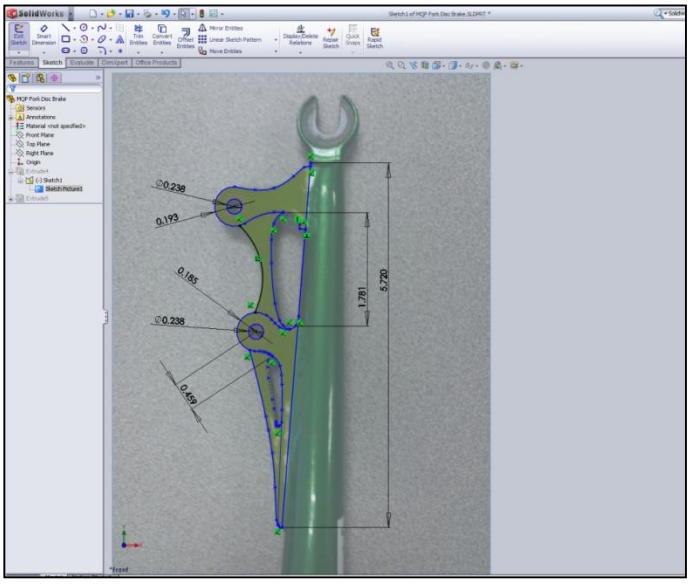

Figure 3-6: Photograph with Sketch Overlay.

The non-complex shapes were then outlined on the image and measured using calipers. Using these measurements, the image was resized to the correct scale, allowing accurate dimensioning by "tracing" certain features as seen in Figure 3-6 using splines. The face was sketched and then the selected areas were extruded to the appropriate height (Figure 3-7). Another sketch was created on the top of the extruded surface and regions from the initial sketch were transferred over to the newer sketch. This sketch was then extruded cut back per a specific depth. During each sketch, measurements were taken on the brake mount with calipers to ensure that the scaling was still accurate.

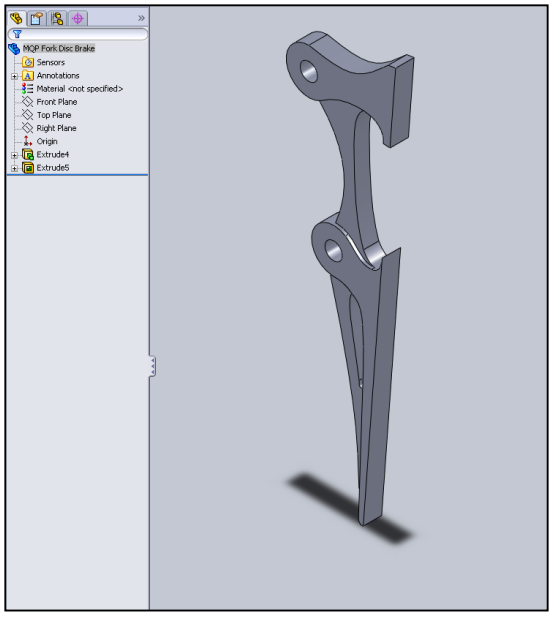

Figure 3-7: Finished Disc Brake Mount.

3.1.5 Dropout Modeling Procedure

Measurements of the inner and outer diameter of the dropout as well as the lengths of both sides were taken using calipers, and a simple horseshoe shape was sketched on the right plane due to the orientation of the assembled fork. The sketch was extruded to the correct measured length allowing extra material that would be cut off later in the modeling process.

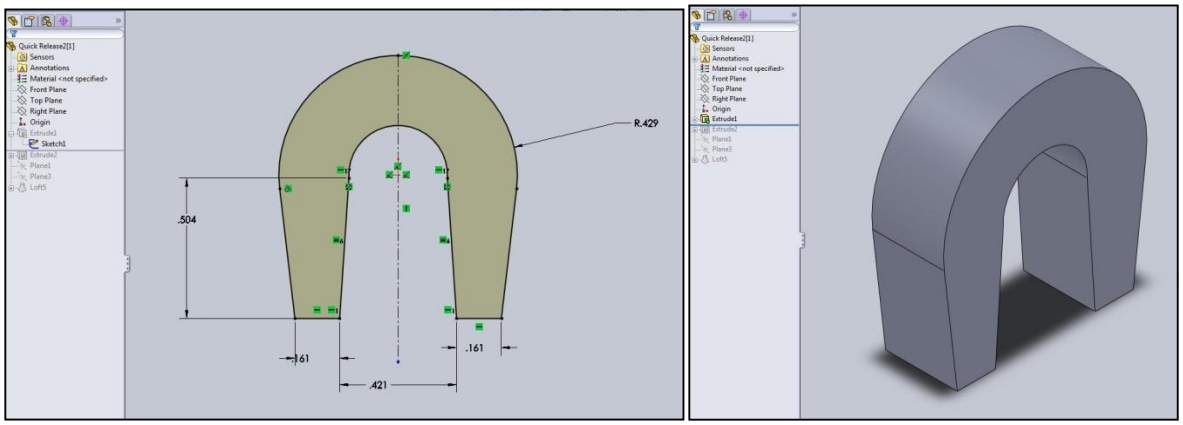

Figure 3-8: Sketching the Preliminary Shape and Extruding.

Another sketch was created on the front plane. The rectangle was drawn to measurements taken using the calipers. Three points that could be precisely measured were inserted into the sketch and a spline was drawn to connect them. An extruded cut was then taken to remove the areas in yellow as seen in Figure 3-12.

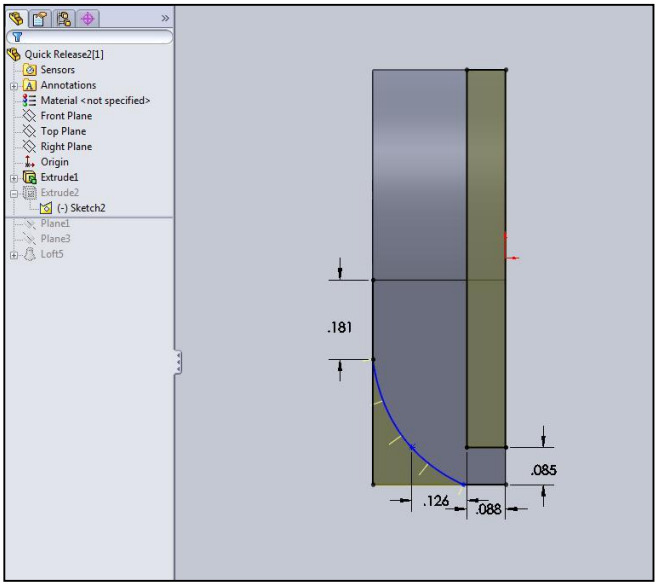

Figure 3-9: Sketch on the Front Plane.

The result of the extruded cut created a base model for the dropout. The next few steps explain how this model was attached to the end of the fork blade. First, measurements of the bottom of the fork blade were taken to give dimensions of the oval shape that the model of the dropout would have to connect to. A plane was then inserted at a certain offset from the horseshoe shaped model, and the oval was sketched onto it as seen in Figure 3-13.

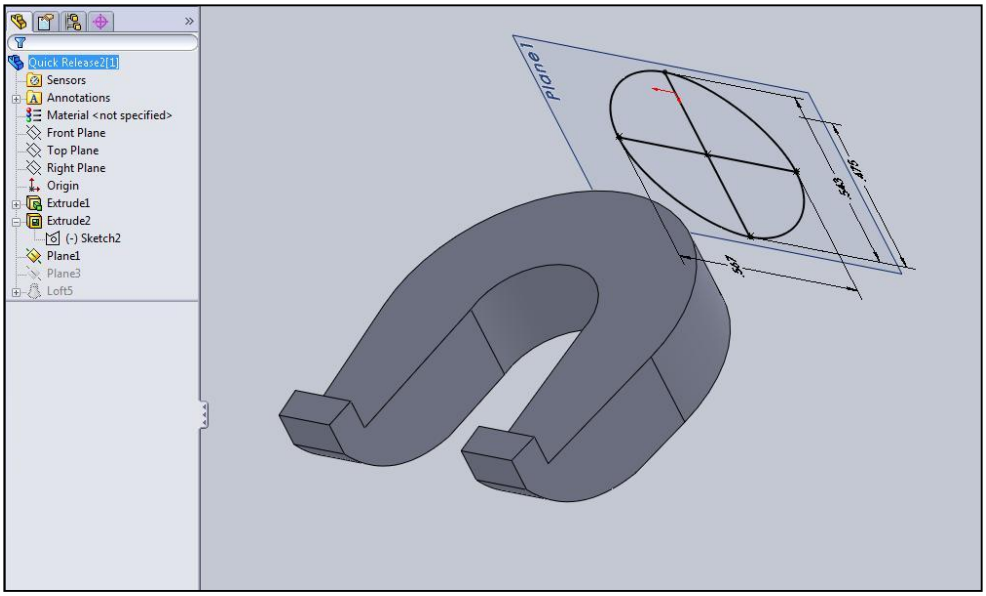

Figure 3-10: The Inserted Plane with the Oval sketch.

A 3D sketch was then used, and a plane was drawn per specific measurements in order to define points on the model that would connect to the top, bottom, left, and right sides points of the oval. Splines were drawn connecting the midpoints of the rectangular plane to the appropriate points on the oval as seen in Figure 3-14. These splines served as the template for the loft.

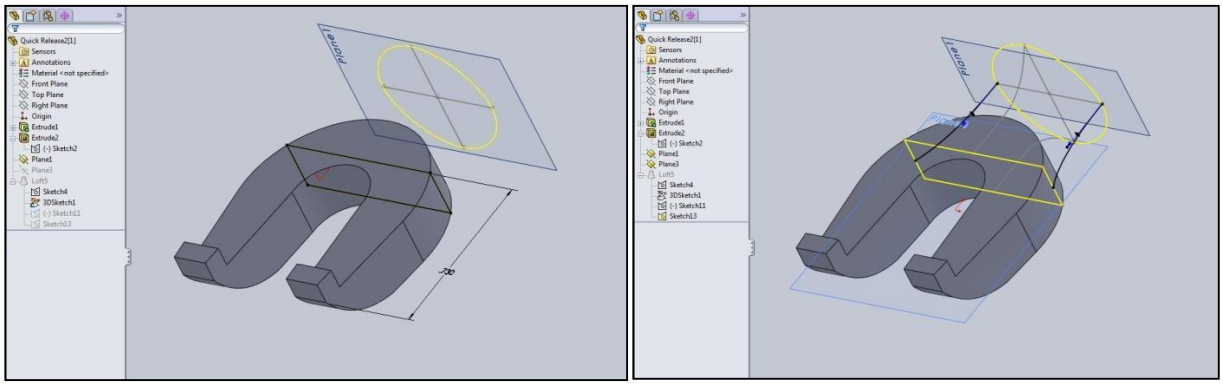

Figure 3-11: Creating a 3D Sketch to be the Template of the Loft.

Once the 3D sketch was complete, the Loft feature was used and adjusted by selecting the newly created splines. The feature was accepted and the result of the finished model is shown in Figure 3-15. This model was attached to the bottom of the fork blades in the assembly.

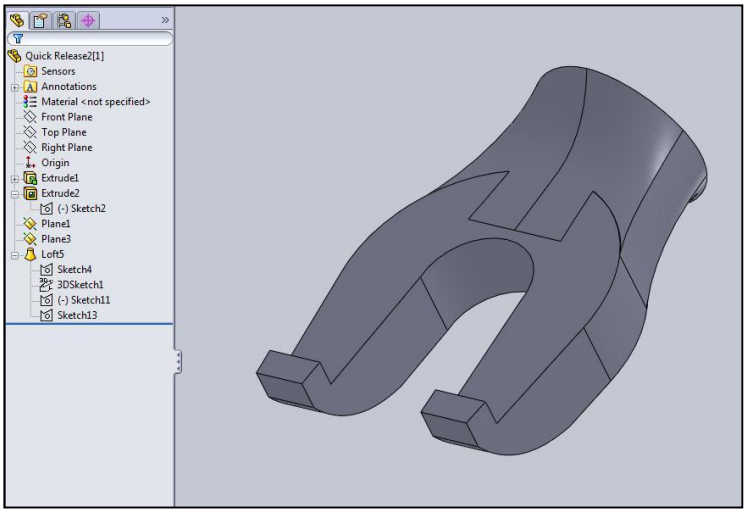

Figure 3-12: Finished Model of the Dropout.

4 Fork Analysis, Testing, and Optimization

The crack in the fork has been shown to form both during off-road riding and ASTM F2273-03 compliant testing. For the initial step towards understanding the stresses created during the ASTM test a finite element analysis was created in SolidWorks Simulation. The results of this analysis led to the development of a fatigue model in ANSYS and an in-house fatigue testing solution to validate the FEA model. This section explores the methodology used and the team's findings.

4.1 Fatigue Testing

Currently the sponsor sends their forks to be tested at a lab in California which charges a considerable amount due to the length of the test and the turnaround time is not as good as they would like. An in-house testing solution was created as part of this MQP to solve these issues. The first step in designing and building the test machine was to understand the ASTM standard. For full test outline see Appendix A.

4.1.1 ASTM F2273-03 Fatigue Test

4.1.1.1 Testing Setup and Procedure

The ASTM fatigue test is an industry standard for testing the strength of bicycle forks during their lifetime to ensure that they will not fail prematurely in the field. Figure 4-1 illustrates the fork position in the testing apparatus and the direction of loading.

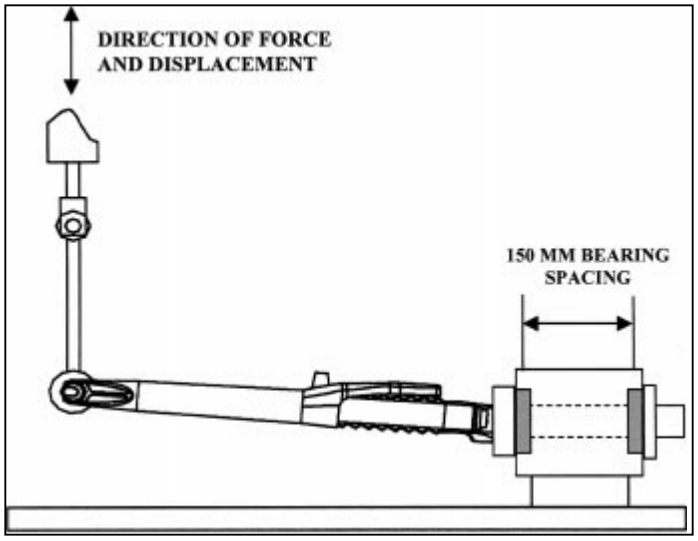

Figure 4-1: ASTM F2273-03 Bending Fatigue Test Loading Scenario.

The fork is secured to a table or other rigid body by inserting the steerer tube into two bearings spaced 150 mm apart. A connecting rod is attached to the actuator and a reinforced axle which is fixed to the quick release dropouts of the fork. The connecting rod is free to rotate about the pin on the actuator and about the axle. A fully reversed cyclic load is applied via the actuator and is monitored to verify that it is within +5.0% of the specified 685 N.

The fork is then tested with the prescribed sine wave for 2000 cycles and the maximum upper and lower deflections are recorded. The limit of displacement is then set to ±0.76 mm from the maximum upper and lower deflections, respectively. The fork is also examined for cracks at this point and if any cracks are visible then the entire group of forks fails the test. If there were no visible cracks then the fork is cycled until the limits are tripped or 250,000 cycles. If the fork is tested for 250,000 cycles without tripping the limits then the individual fork passes and the next fork from the group is tested. If the limit is tripped then the number of cycles is recorded and the fork is inspected for cracks. If the fork has visible cracks and the total number of cycles is less than 50,000 then the fork group fails. If the total number of cycles is greater than 50,000 then the number of cycles is recorded and the fork passes. If there were no visible cracks and the limit has been tripped less than three times then the fork is cycled for 1000 times, the upper and lower max deflections are recorded, and the limits are set to ±0.76 mm from the maximum upper and

lower deflections, respectively. The testing then reverts back to the previous state of this procedure where it is tested until the limits are tripped or 250,000 cycles. If it was the third time that the limit had been tripped then the number of cycles is recorded and the next fork from the group is tested.

4.1.1.2 Passing the Test

Once testing of all 5 forks in a group is completed, statistical analysis of the group is done. As long as the group passes statistical analysis and no individual forks had less than 50,000 cycles to failure, the entire group passes.

4.2 Finite Element Analysis

4.2.1 First Analysis of Fatigue Test

The first step in understanding the stresses created during the ASTM fatigue testing procedure was to take the solid model of the fork, created during the preliminary geometry characterization, and perform a Finite Element Analysis of two loading conditions: static loading of 685N upward and static loading of 685N downward. For this preliminary analysis SolidWorks Simulation was chosen as the CAE package.

4.2.1.1 Analysis Setup and Development

In order to simulate the ASTM test, a new assembly was created. In addition to the fork assembly, two bearings made of bronze were inserted as well, mated to the steerer tube so that the fork was still free to rotate about and translate along the steerer tube axis, and spaced at the specified 150mm apart. SolidWorks Simulation allows for the rapid development of FEA models. The model was brought into the CAE package and the upward static loading study was created. The outer surface of the bronze bearings are constrained to have zero degrees of freedom and the 685N force was spilt across the upper faces of the quick release dropouts. The fork was meshed with a standard draft element size and the simulation was run. The setup and results are shown in Figure 4-2.

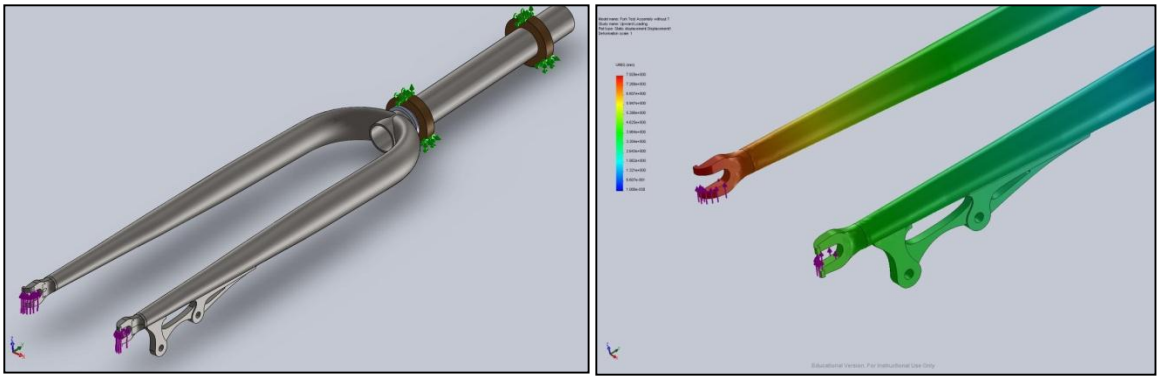

Figure 4-2: Loading scenario and resulting displacement of initial FEA.

As can be seen from Figure 4-2, the displacement of the quick release drop out on the blade without the brake caliper mount is nearly twice that of the blade with the mount. In the actual ASTM test the two dropouts are loaded by an actuator attached to a heavy-duty axle which spans the between the quick release dropouts. This analysis therefore does not accurately model the ASTM standard but it does provide some important insight into just how much the brake caliper does in stiffening the fork blade. In order to move closer to the ASTM test a model, deemed the "Loading T", of an axle with a rod intersecting the axle perpendicularly was created. This was then inserted into the fork test assembly and the static study was redesigned.

The introduction of the loading T aimed to solve the issue of non-uniform displacement of the fork blade dropouts but it also introduced several issues. The first issue dealt with the boundary conditions at the loading T-dropout contact area. It was determined that the T was free to rotate about the axle axis and translate along the loading axis, no frictional forces at the contact area were considered. Another issue was the possibility of excessive deformation of the loading T that would skew results. A quick analysis was run with a draft quality mesh. Investigating the results showed that the dropouts had nearly uniform displacement and that any deformation in the loading T was minimal. The meshing was refined to a curvature based mesh to ensure a high level of accuracy in the more complex areas of the fork model. This improved setup and the mesh in the fork blade and steerer tube joint area is detailed in Figure 4-3.

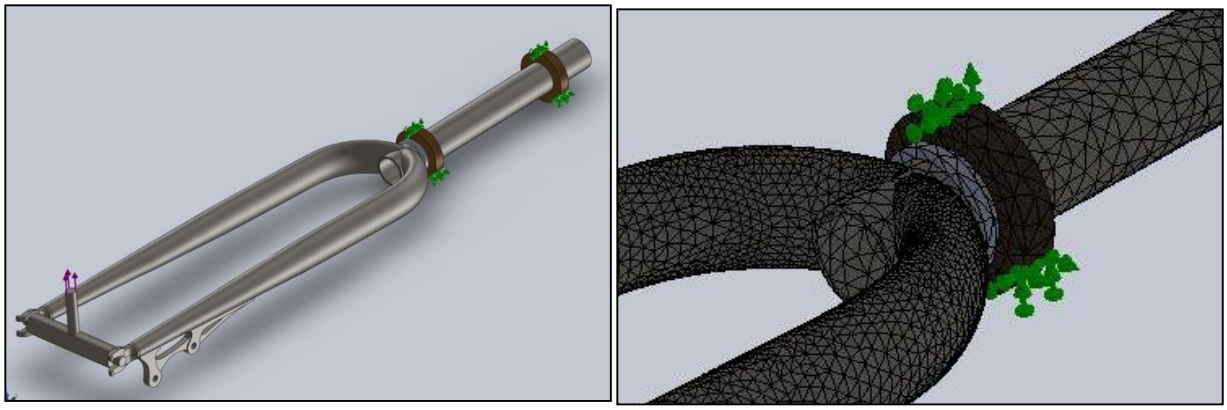

Figure 4-3: Improved FEA Analysis Setup and Mesh.

4.2.1.2 Analysis Results

The study was run and the output was analyzed. A plot of the stress in the fork shows stress concentrations in two areas both of which near the fork blade and steerer tube joint. One is below the fork blade and the other is near the top in the steerer tube, between the fork blade and crown race. These concentrations are highlighted in Figure 4-4 and are of magnitude 46ksi and 44ksi, respectively.

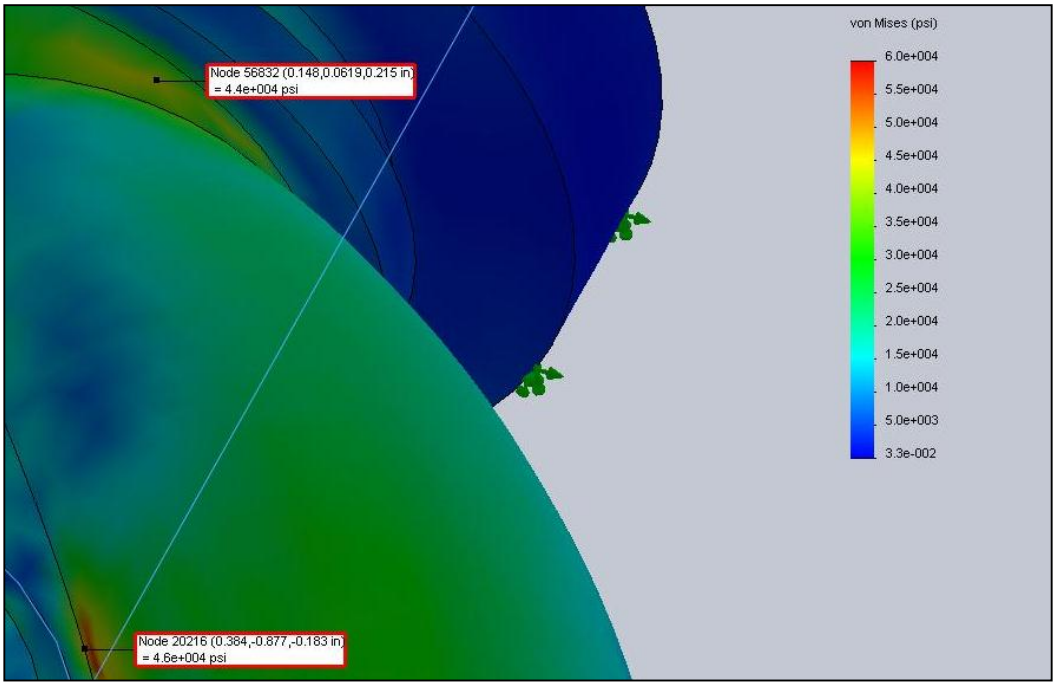

Figure 4-4 Stress Concentrations in Improved Analysis.

Figure 4-4 shows the upper stress concentration region on the front side of the fork. This region continues to the back side of the fork and is on the side of the steerer tube, centered above the fork blade.

Only the forks that have cracked as a result of heavy riding have been investigated by the MQP team, but this area of stress concentration does coincide with the area in which the cracks developed during actual riding. Figure 4-5 shows changes in the magnitude of the stress from the front to the back of the fork. Node #3771 lies on the steerer tube centered directly above the fork blade.

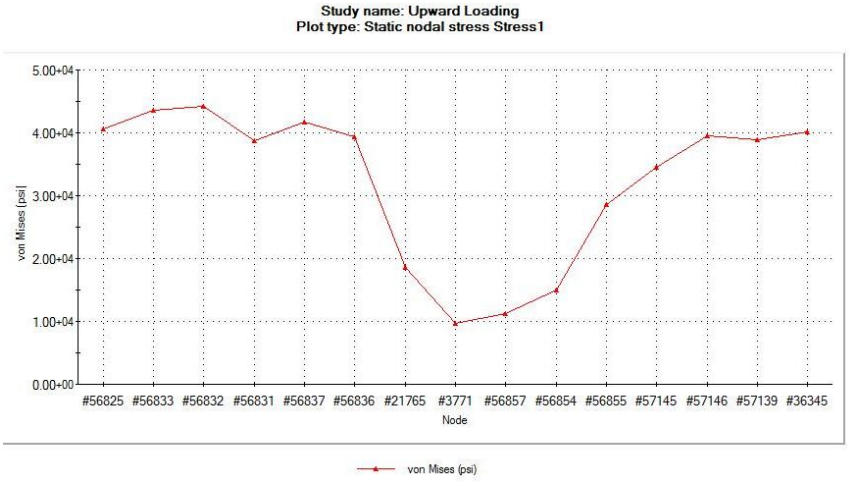

Figure 4-5 Variation of Stress through the Nodes in the Upper Stress Concentration.

The yield and ultimate tensile strengths for this 4130 alloy are 52.2ksi and 81.2ksi respectively; both are greater than the maximum stress in the model as predicted by this simulation. The maximum stress during static loading of the force specified in the ASTM standard does not allot for a factor of safety much greater than 1.1 before plastic deformation occurs, and not more than 1.8 before failure occurs. The study was carried out with the same loading scenario and mesh, but with the loading direction reversed. The stress concentrations were in the same area as in the upward loading, Figure 4-6 shows the stress distribution through the stress concentration that is located above the fork blade. Node #61457 is centered above the fork blade in this study.

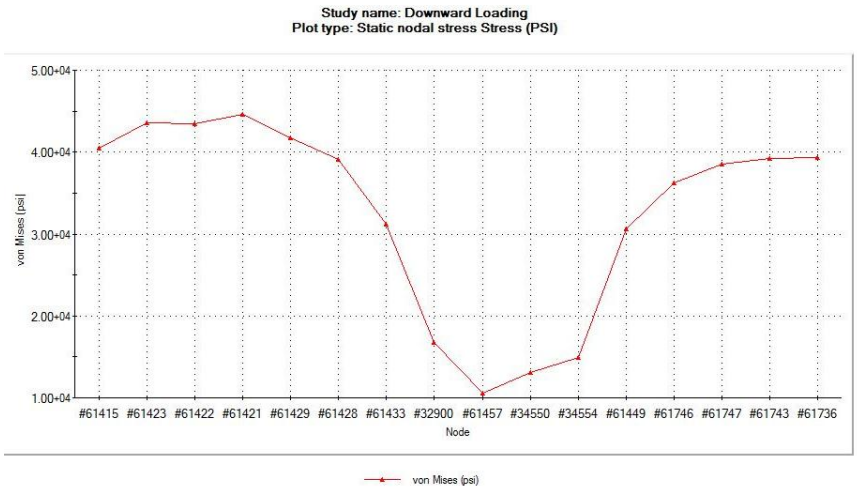

Figure 4-6 Variation of Stress through the Nodes in the Lower Stress Concentration.

As expected, in the downward loading scenario the maximum stress occurred above the fork blade-steerer tube joint and was 45ksi in magnitude. The maximum stress in the stress concentration located below the fork blade was 41ksi. Again, these are both below the yield and tensile strengths of the material, but provide very little factor of safety.

4.2.1.3 Preliminary Analysis Conclusions

The stress concentrations in the FEA model are located in the region where the actually ridden bike forks have developed cracks. This lends itself to prove some level of validity in our model. In order to develop a strong correlation a better solid model built from the geometry of an unpainted fork, modeling of the weld area, and the inspection of a fork that has failed the ASTM test were needed. Once these were obtained, a second set of static analyses and a true fatigue analysis to correlate cycles to failure between the ASTM test and the simulation were conducted. This set of studies also included the geometry of the weld and braze region to further improve the accuracy of the model. Once a strong statistical correlation was developed the fork blade geometry was modified to find an optimized solution for the sponsor. Development of this model allows for rapid testing of different fork blade geometries, and then, selection of the best suited designs.

4.2.2 Final Analysis of Fatigue Test

The results of the preliminary analysis indicated that the loading of the fork according to the ASTM standard could likely result in stresses which would exceed the yield strength of the material. The next step was to confirm these results with a more thorough analysis incorporating the brazed, welded, and heat affected regions. ANSYS V11 was chosen for its accuracy and ability to develop a fatigue life model as well as the static stress situations already explored. The process flow for creating an ANSYS fatigue model is shown below in Figure 4-7.

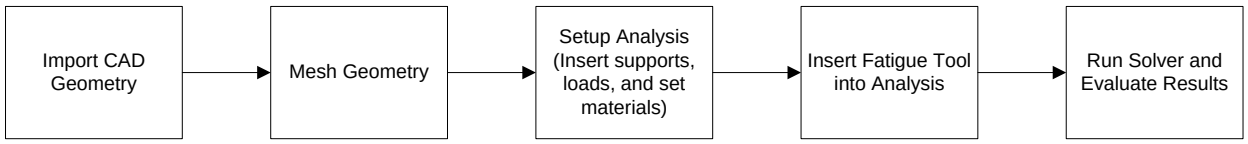

Figure 4-7: ANSYS Fatigue Life Model Creation.

This section details the analysis creation, setup, and corresponding results.

4.2.2.1 Determination of the Mechanical Properties for FEA

In order to create an accurate FEA model it was necessary to input the correct material properties and fatigue curves into ANSYS. Since there is a very limited amount of information on fatigue properties of 4130 steels that have been treated the same way as the ones used in the bicycle fork, it was necessary to estimate the shape of the fatigue curves. An engineering "rule of thumb" was used that allows the fatigue curves to be estimated by the ultimate tensile strength. This is done by calculating three values, S_m, S_e, and the fatigue limit. Calculation of S_m and S_e uses the simple relations shown below where S_m is the degraded stress after 10,000 cycles, S_e is the degraded stress after 1.0E7 cycles, and the UTS is the ultimate tensile strength.

$$S_m = 0.9UTS$$

$$S_e = 0.5UTS$$

In order to obtain a more accurate curve, fatigue curves for a 4130 steel from CES Edupack were used. Values were obtained by using the values that were calculated from the UTS, and then, they were extrapolated based on the model fatigue curves.

4.2.2.2 Brazed, Welded, and Heat Affected Regions

By sectioning the CAD model of the fork into specific regions the respective material properties of each region could be applied enabling a more accurate model. The fork was sectioned along the boundaries of the HAZ. The boundaries were determined through microstructural analysis. Figure 4-8 shows the various regions.

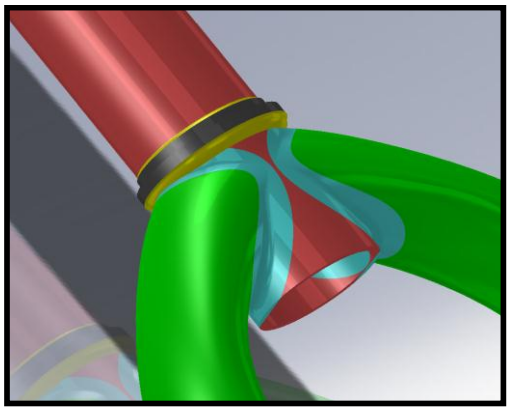

Figure 4-8: Steerer Tube (Red), Heat Affect Zone (Light Blue), and Fork Blades (Green).

Coincident nodes and bonded contacts were used to ensure that the strain was equal at the boundaries. In addition, the materials data that are determined experimentally are incorporated into the model. A complete listing of the material properties used is available in Appendix H.

4.2.2.3 Mesh Refinement

ANSYS automatically generated a coarse mesh of the model which was then refined to improve the accuracy of the model in the primary area of interest; where the cracks have been observed to form. This

was along the welded region between the fork blades and steerer tube. Controls were added to the model to refine the mesh in this area. Figure 4-9 illustrates the results of this refinement. The resulting mesh was coarse outside the welded and brazed region, fine within the welded region, and the meshing at the boundary areas is matched node-to-node.

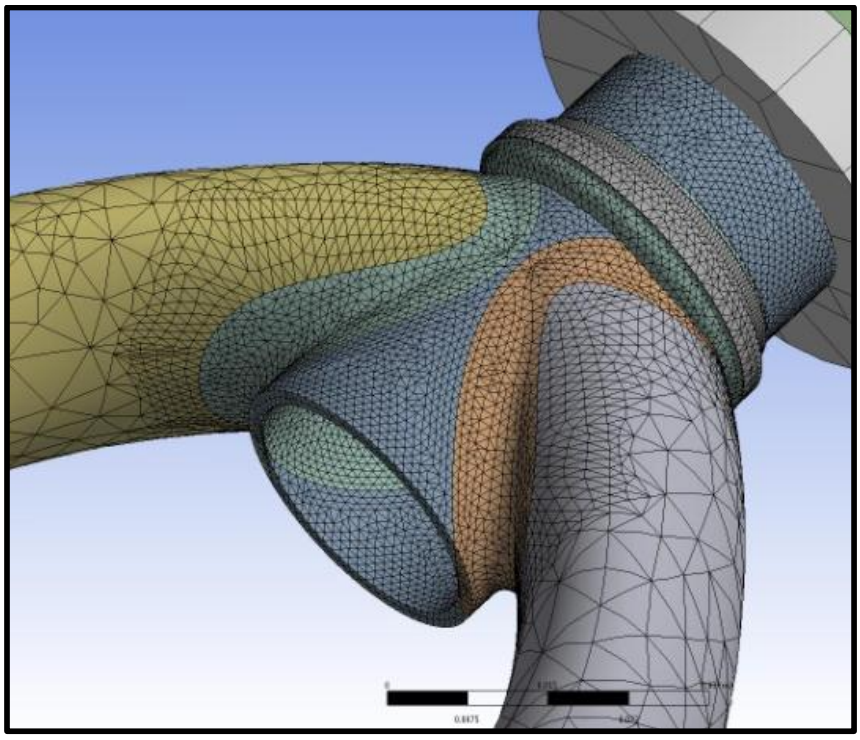

Figure 4-9: Refined Mesh in ANSYS.

The resulting mesh was coarse outside the welded and brazed region, fine within the welded region, and the meshing at the boundary areas is matched node-to-node.

4.2.2.4 Static Structural Analysis Setup and Results

The ANSYS fatigue tool requires that an analysis be created with the desired loading conditions. It then takes the stresses determined at each node, interpolates between them, and compares the stress to a curve of the degraded ultimate tensile strength of the material at that node. The life of the part at a given node is determined as the number of cycles after which the stress at that node exceeds the degraded UTS.

Several Static Structural analyses were created based on the ASTM test and our in-house fatigue testing solution. These analyses served as the basis of the ANSYS fatigue model. The different parameters for the analyses are shown in Table 4-1 and the loading direction is defined in Figure 4-10. High stress scenarios were considered to be 100% of the CEN specified load, which is greater than the ASTM specified load, while low stress cases were 10% of the CEN specified load.

Table 4-1: Loading Scenarios in ANSYS Analyses of Original Geometry

Analysis	Loading Direction (Parallel to)	Load Magnitude (N)
Upward Loading High Stress	Positive Y-Axis	685
Upward Loading Low Stress	Positive Y-Axis	68.5
Downward Loading High Stress	Negative Y-Axis	685
Downward Loading Low Stress	Negative Y-Axis	68.5

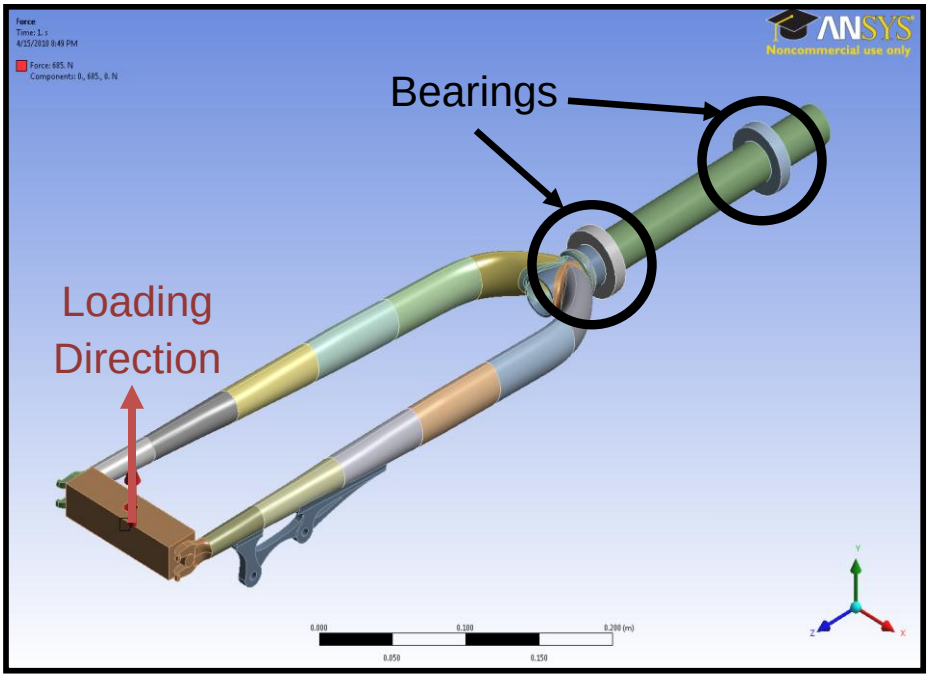

Figure 4-10: Loading Direction (Shown in red, along the +Y axis) and Support Bearings.

The Y axis is defined to be collinear to the steerer tube axis, the X axis is parallel to the dropout axis and orthogonal to the Y axis, and the Z axis is normal to both the X and Y axis. The fatigue analysis only considers the stresses resulting from a static analysis and does not account for differences in the magnitudes of the part stresses due to fully reversed loading (i.e.: Greater stresses as the fork is loaded in the positive Z direction versus the negative Z). As a result, the upward and downward portions of the fatigue cycling were investigated separately. The effects of lower loading stresses on part life were also explored. The bearings shown in Figure 4-10 were fixed to ground and the steerer tube was allowed to rotate about the Y axis - these constraints correspond to the setup in the experimental testing.

4.2.2.5 Fatigue Life Analysis

The degraded property curves for the various fork materials were determined as described in Section 4.2.2.1. Table 4-2 shows the resulting minimum stress, maximum stress, and fatigue life of the HAZ area of the fork blade from the initial analyses that were carried out.

Table 4-2: Results from ANSYS Analysis of Original Geometry.

Loading Direction	Minimum Stress (MPa)	Maximum Stress (MPa)	Fatigue Life (cycles)
+Y Loading	7.78e6	5.02e8	24,900
-Y Loading	7.76e6	4.96e8	25,200

Comparing the max stress in the HAZ to the properties of the degraded materials in the weld area, it is apparent that they are of similar magnitude. As a result, the model is extremely sensitive to the inputted curve. Further testing of the material properties in this area could improve the accuracy of the model. The equivalent stress throughout the HAZ and the fatigue life of the HAZ are shown in Figure 4-11 and Figure 4-12, respectively.

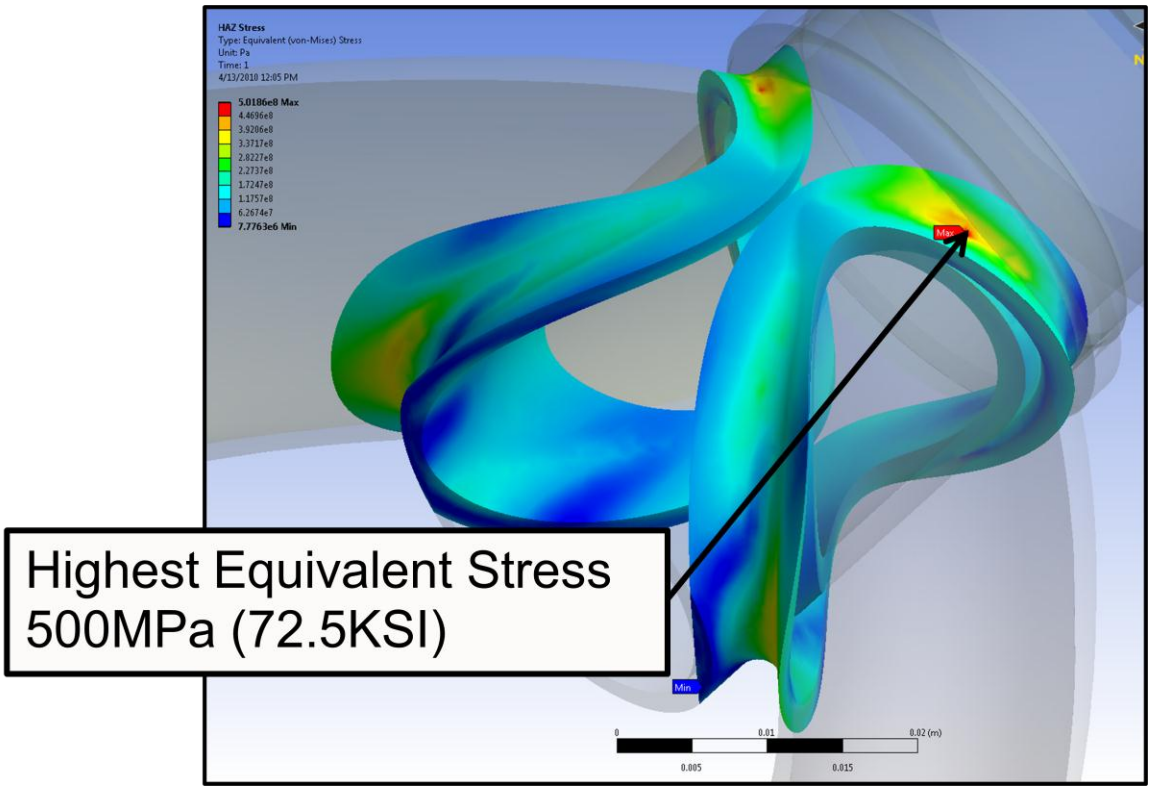

Figure 4-11: Equivalent Stress in Heat Affect Zone.

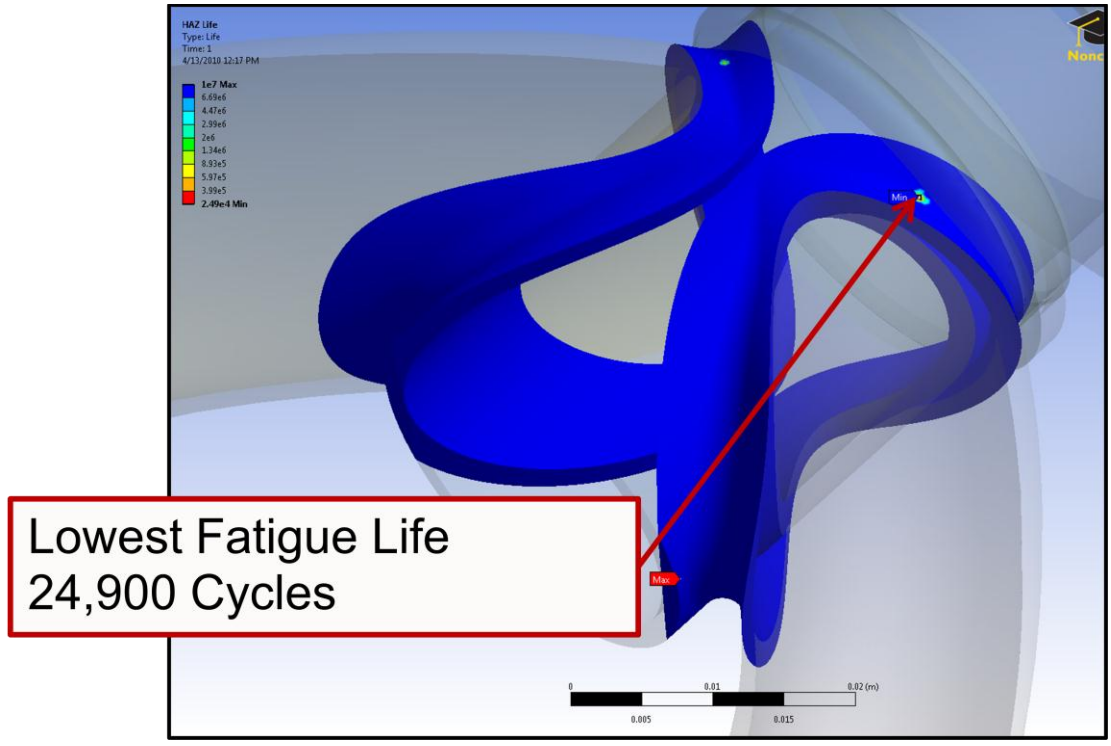

Figure 4-12: Fatigue Life of Heat Affect Zone.

4.3 FEA Model Validation

4.3.1 Custom Fatigue Testing Solution - Design and Fabrication

In order to utilize the FEA model as a design iteration tool its results needed to be validated by correlation to experimental testing data. Due to the size and the relative magnitude of the loads and displacements required, a custom fatigue testing machine was designed, built, and employed in the FEA model validation.

4.3.1.1 Task Specifications

In order for the testing machine to carry out the test per the ASTM standard it must meet the following task specifications:

1. The machine shall be rigid to ensure that the fork was the primary source of deflection and not the fixture.
2. The machine shall be able to withstand the cyclic loading itself. (Carry out a minimum of 12 100,000 cycle fatigue tests without performance degradation)
3. The machine shall be rigid so that it doesn't require excessive fixturing to a rigid table.
4. The machine shall be portable. (Weigh less than 60 lbs)
5. The machine shall be small enough to fit onto a 3 ft by 8 ft lab bench.
6. A double acting single ended pneumatic cylinder will be used to load the fork.
7. The pressure supplied to each side of the pneumatic cylinder must be regulated separately so that greater pressure can be supplied to the piston with less area.
8. The machine shall be operable on commonly available air pressures and flow rates when carrying out the ASTM specified fatigue loading of 685N at a rate of 1Hz. (Less than 120PSI at 22CFM)
9. The dimensions of the fork holding mechanism shall meet the bearing spacing detailed in the ASTM standard. (150mm center to center)
10. That load shall be verified to be within +5% of 685N, the number of cycles recorded, and the maximum upper and lower deflection measured.

11. The machine must be able to count the cycles and report out this datum.
12. Limit switches must be used to stop the machine in the event of fork failure.
13. The noise created by the machine must be tolerable when at a distance of 6 ft with ear plugs in.

4.3.1.2 Load Application System Design

Many different methods of load application were considered before choosing pneumatic actuation. Regulation of the air pressure supplied to the cylinder allowed for simple control over the magnitude of the applied load. Figure 4-13 shows the pneumatic circuit designed to control the loading of the fork.

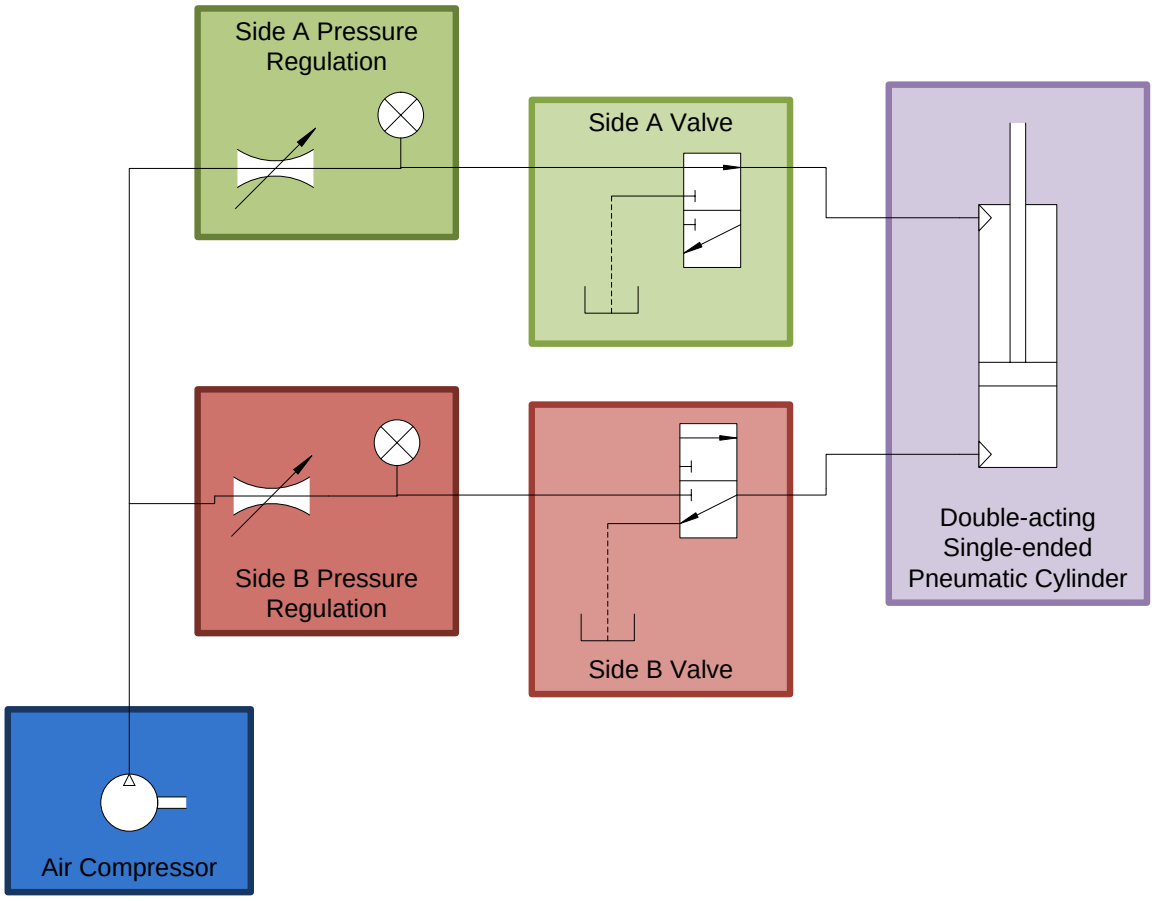

Figure 4-13: Fatigue Testing Machine Pneumatic Circuit.

A double-acting single-ended pneumatic cylinder was chosen to create the fatigue loading. This setup required two pressure regulation circuits in order to supply a higher pressure to the side of the cylinder with the rod end. Two three-way two position solenoid valves were used to control which side of the

cylinder was supplied with air pressure. One concern was whether choking of the air inlets and outlets would occur as one side of the cylinder was raised to high pressure and the other vented to atmosphere given the loading frequency of 1Hz. An analysis of several common inlet sizes was conducted to determine the minimum required diameter to achieve acceptable fluid velocities through the system based on the specified pressure and load application frequency. A 3/8in NPT size was chosen based on availability and suitable fluid dynamics, the complete analysis of the system is shown in Appendix I. A 1.75in diameter pneumatic cylinder was selected so that the machine would be able to run at the commonly available shop air pressures of 110 psi.

4.3.1.3 Machine Structure Design

Every bicycle that the sponsor constructs is a custom build for each individual customer. In order to ensure that the fatigue testing machine would be able to test the various forks made by the sponsor and others, an adjustable, modular design was conceived. This is show in Figure 4-14.

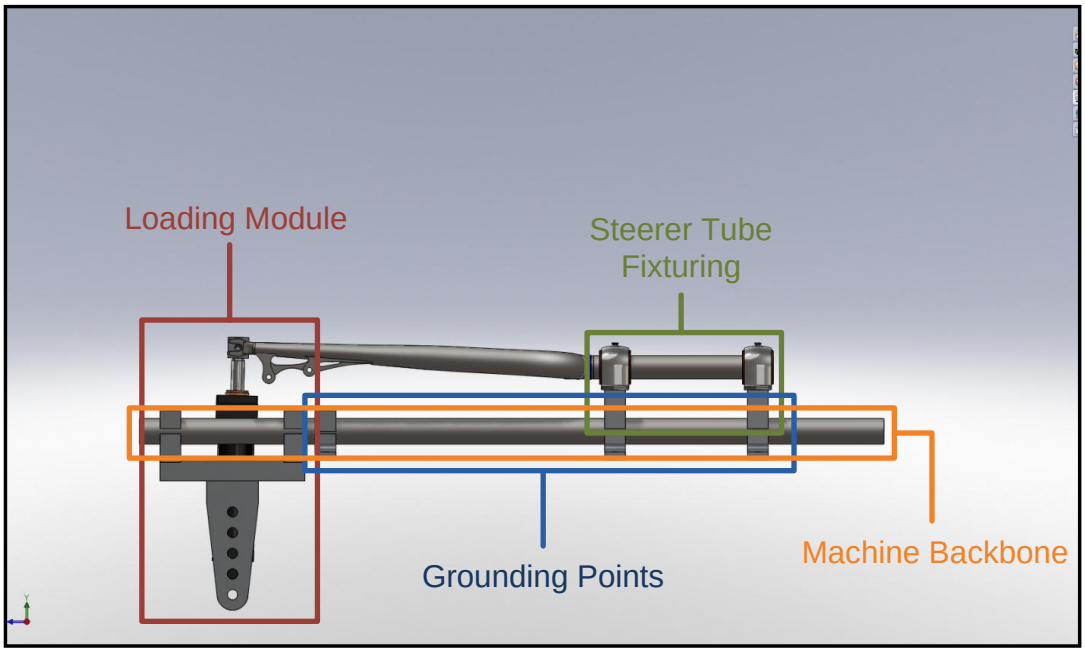

Figure 4-14: Modular Design of Fatigue Testing Machine.

The primary structural element of the fatigue testing machine is the backbone, shown in orange in Figure 4-14. Round steel tubing was selected to reduce potential stress risers and maximize the life of the

machine. The backbone allows for a modular design where the steerer tube fixturing, loading module, and ground points are separate entities that can be translated along the length of the backbone maximizing adjustability of the machine. The predicted peak-to-peak displacements of the fork during testing were less than 4in. Since the air in the pressurized side of the cylinder would have to be vented to atmosphere once every second it was desirable to have a cylinder with as short a stroke as possible. This being the case, the loading module was designed so that the pneumatic cylinder could be moved up and down based on the rake of the fork blades. This allowed for the implementation of a cylinder with a shorter stroke. The steerer tube fixturing allows for easy interchange of different holders for steerer tubes of varying diameters. Figure 4-15 shows the assembled model of the loading module.

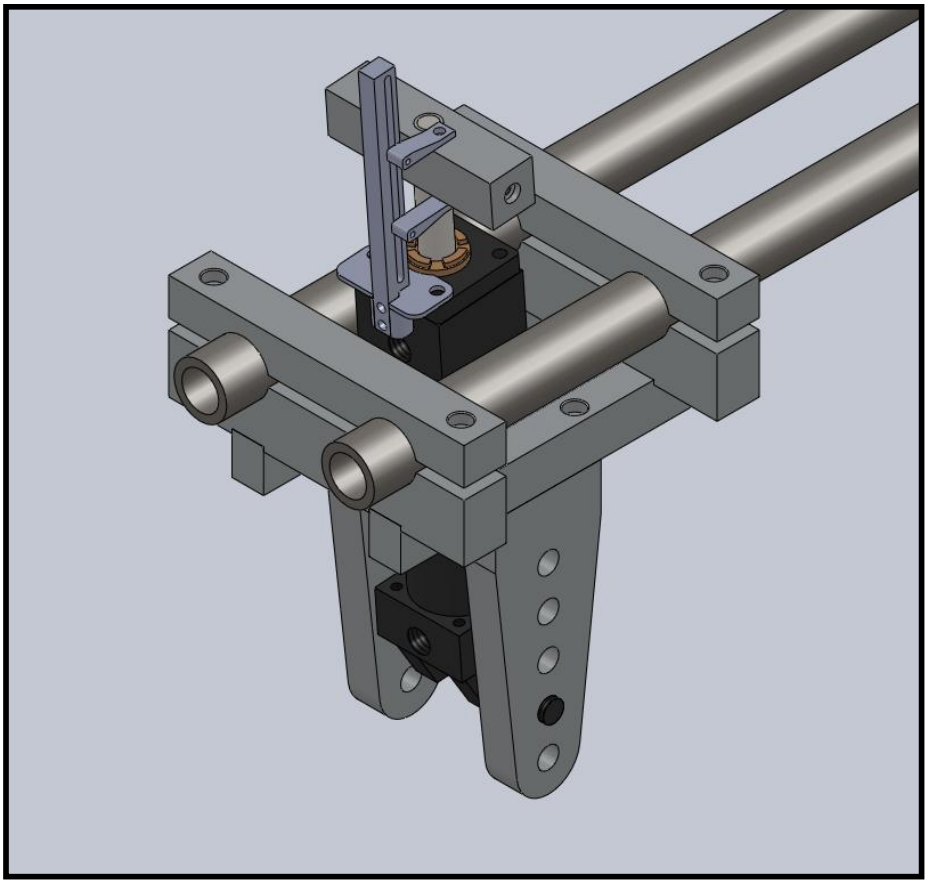

Figure 4-15: Fatigue Testing Machine Loading Module.

Each of the individual parts was designed so that they could be fabricated in no more than 3 machining operations. This consideration of the manufacturing process minimized the amount of time spent building

the machine. The regulator and valve assembly designed to control the pneumatic cylinder is show in Figure 4-16. This assembly is very similar to the system depicted in Figure 4-13 with the exception that the valves are actually five-way two position valves. By plugging the unneeded valve passages the more complex valve becomes the equivalent of a tree-way two position valve.

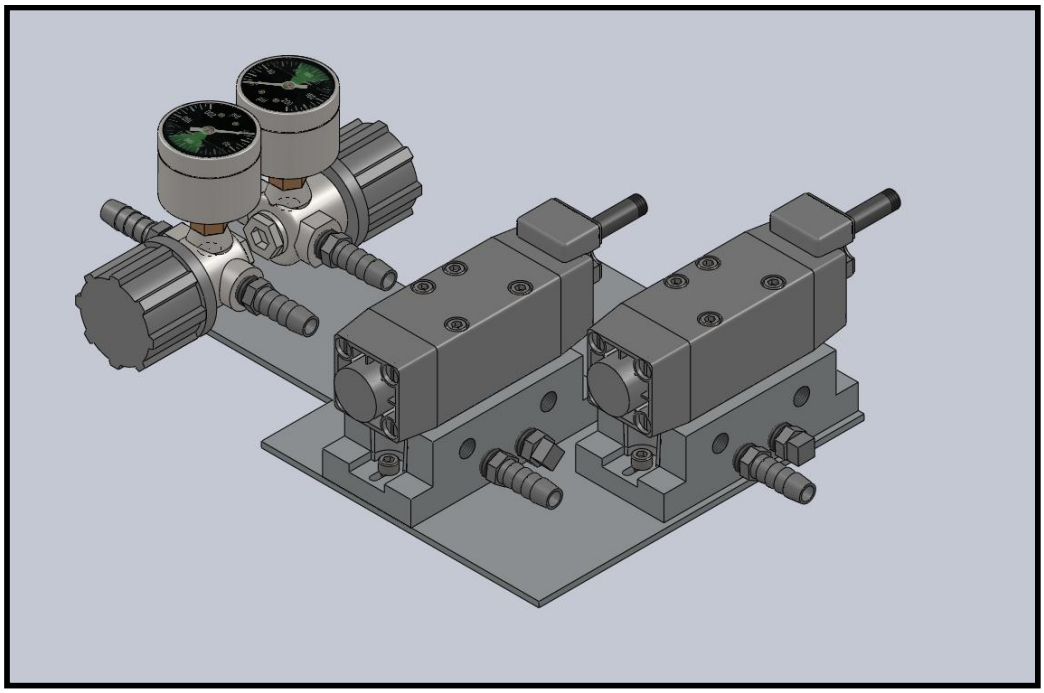

Figure 4-16: Pressure Regulators and Solenoid Valves.

4.3.1.4 Machine Fabrication

The parts for all modules were CNC machined in the HAAS technical center. This minimized the labor required to build the machine, and also allows future users of the machine to rapidly fabricate replacement parts if needed. Esprit 2009 was used to generate the tool paths used to control the CNC machines. Figure 4-17 shows the finished CAM work for a tube clamp part.

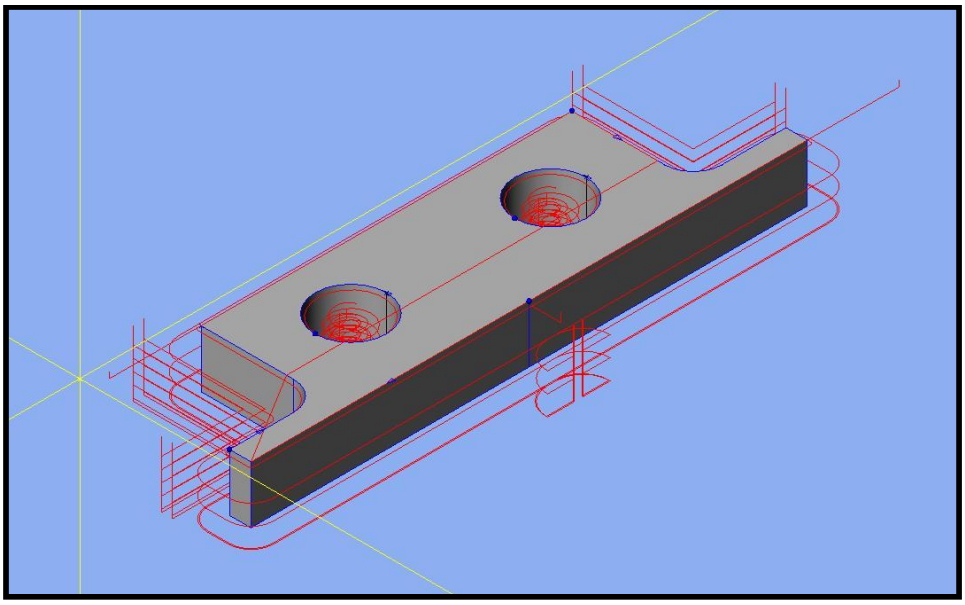

Figure 4-17: Tool paths created by Esprit 2009 to cut part.

Due to the simple design of the parts for our fixture, complex paths and tool movements are eliminated allowing for low cycle times. Figure 4-18 shows a tube clamp part in the HAAS MiniMill after a completed machining operation.

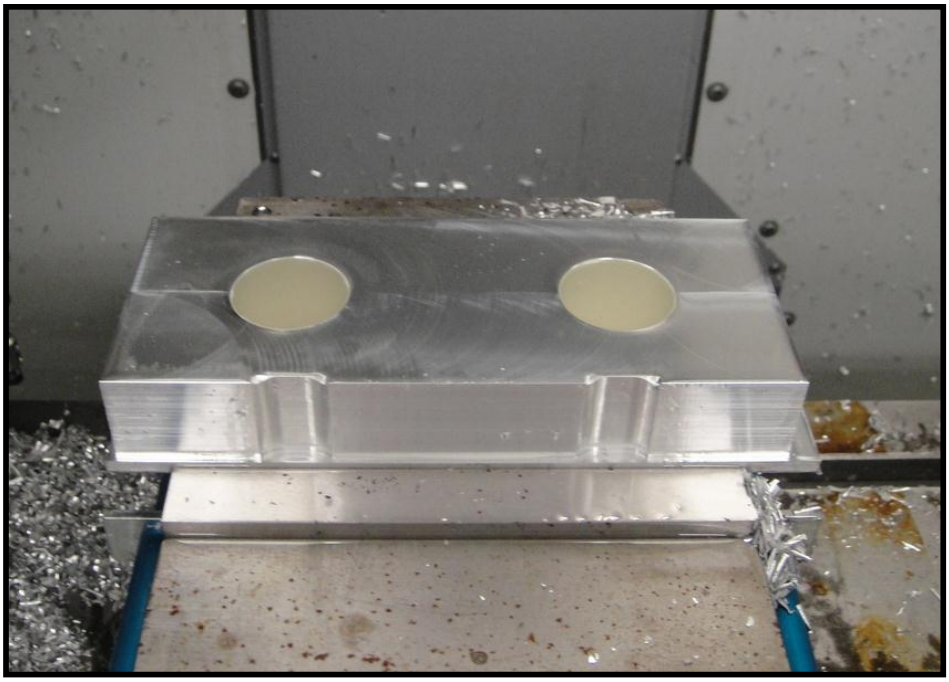

Figure 4-18: One of the Tube Clamps that Supports the Pneumatic Cylinder.

As the parts were manufactured, the machine was gradually assembled and the parts fit checked; this is show in Figure 4-19.

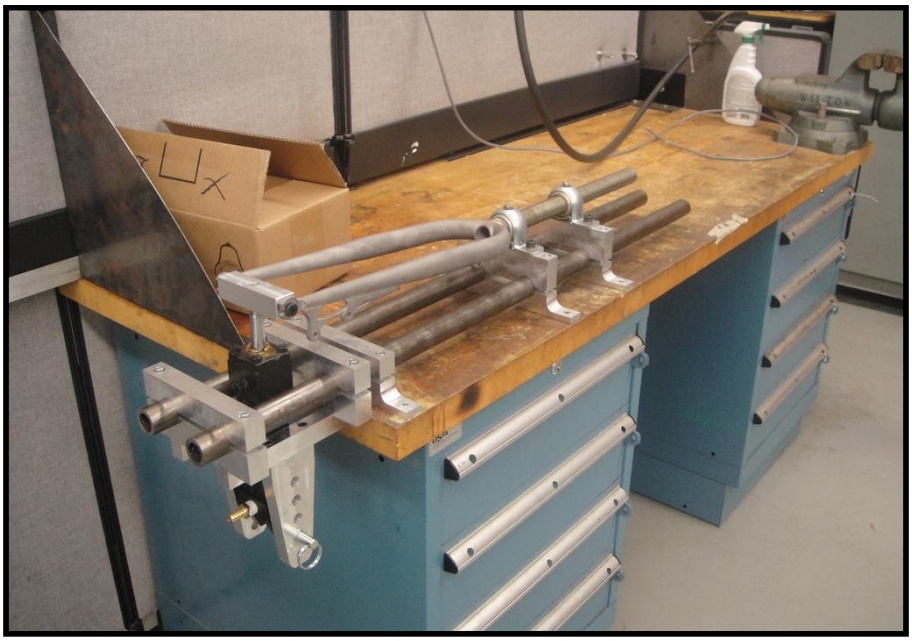

Figure 4-19: Testing the Fit of the Mechanical Pieces.

4.3.1.5 Machine Control System

The five-way two position valves were controlled by 24V solenoid valves. In order to control the actuation of the solenoids and carry out data logging during testing, two paths were explored. The first was the use of a LabView system. A simple virtual instrument within LabView could be constructed which would interface with a USB data acquisition unit to run the control circuit and data logging. The second option was to use a microcontroller to carry out these tasks. Since the machine needed to be as standalone as possible and would run for hours on end, the Arduino microcontroller was selected to control the fixture thus eliminating the need for a computer at the bench.

Actuation of the solenoids required that they be supplied with 24VDC. The Arduino, and most other common microcontrollers, cannot supply this high a voltage or the required current to actuate a solenoid of this size. In order to overcome this, the control circuit in Figure 4-20 was designed and employed. The digital input/output pin was tasked to control the solenoids by leaving the relay in state one where

Side B of the cylinder was being pressurized or activating the MOSFET and thus flipping the relay and pressurizing Side A of the cylinder.

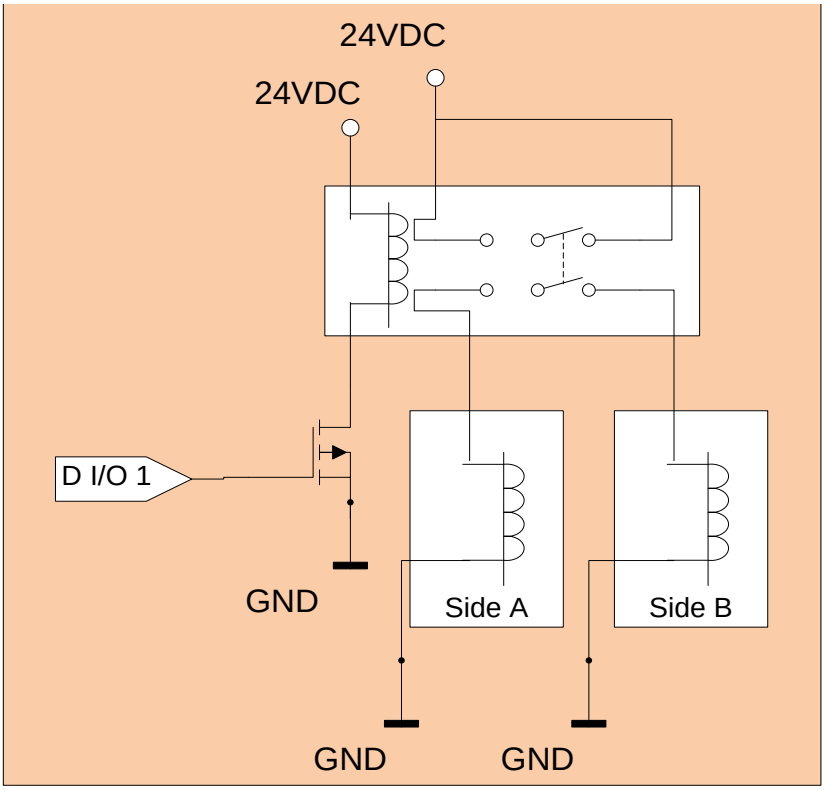

Figure 4-20: High Pressure Pneumatic Circuit Control.

Limit switches were used to stop the machine once the specified max and minimum displacement were reached. The switches were attached to an adjustable armature allowing for the specified increases in the limit according to the ASTM standard. In addition, the armature was designed to swing out of the way in case of total failure of a fork during testing. This prevented any damage to the switches if this were to occur. The control circuit for the switches is shown in Figure 4-21.

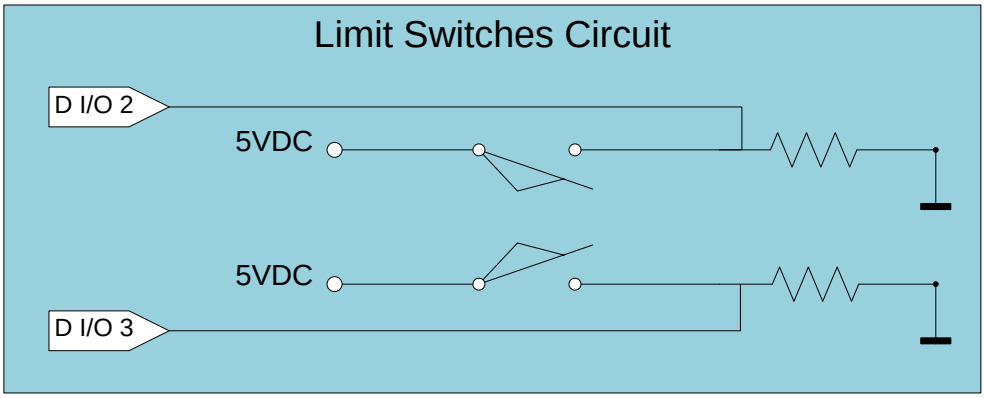

Figure 4-21: Limit Switches Circuitry.

4.3.2 Custom Fatigue Testing Machine - Setup and Operation

Since a limit of three forks were available for testing, care was taken to setup the fatigue tests the same way for each test. The goal was to ensure repeatability and minimize the variation in our results. The setup procedure is detailed below:

1. Using calibrated pressure gauges, adjust the pressure regulators to provide the desired load to the fork.
    a. In our case the load was 685N, the pneumatic cylinder had a diameter of 1.75in, and the rod end had a diameter of 0.625in and was attached to only one side of the piston. This correlated to a pressure of 105.5psi for the side without the rod end and 87.2psi for the side with the rod end.
2. Loosen the bolts clamping the loading module to the machine backbone and the bearing block bolts.
3. Clean the steerer tube, dropouts, and force application block with degreaser.
4. Slide the steerer tube through the bearing blocks until the crown race is resting in contact with the face of the first bearing.
5. Install a shaft collar on the far side of the second bearing block thus prevent translation along the axis of the steerer tube.
6. Thread the force application block onto the rod end of the pneumatic cylinder.

7. Connect the fork dropouts to the force application block with shoulder bolts, abstain from fully tightening them.
8. Slide the force application module along the axis of the machine backbone until axis of the pneumatic cylinder is orthogonal to the axis of the steering tube. This should be checked with a square.
9. Tighten and check all bolts.
10. Install limit switches to stop test in the event of catastrophic failure of the fork.
11. Setup video camera for a macro view of the failure region. The video footage was used to determine the number of cycles require to propagate the crack to a specified length. This allowed determination of crack initiation through SEM examination of the striations on the fracture surface.
12. Begin testing.

During operation the machine was checked regularly. The video camera also provided a live magnified view of the area in which the cracks had been observed to form.

4.3.3 Location of Fatigue Failure

During the fatigue testing the propagation of a crack was recorded. On a macroscopic scale, the crack appeared to initiate in the fork blade heat affected zone as in Figure 4-22. The crack then proceeded to grow towards the front of the fork (Figure 4-23) through the heat affected zone as discussed in Section 2.10.1. Future research could test different brazing filler or another attaching material to see if there is a heat affected zone created by the low temperature brazing. Multiple tests confirm the location of crack initiation. Tests showed that the crack can initiate on the top of either the left or the right fork blades suggesting inconsistencies in the comparative quality of welds on different forks.

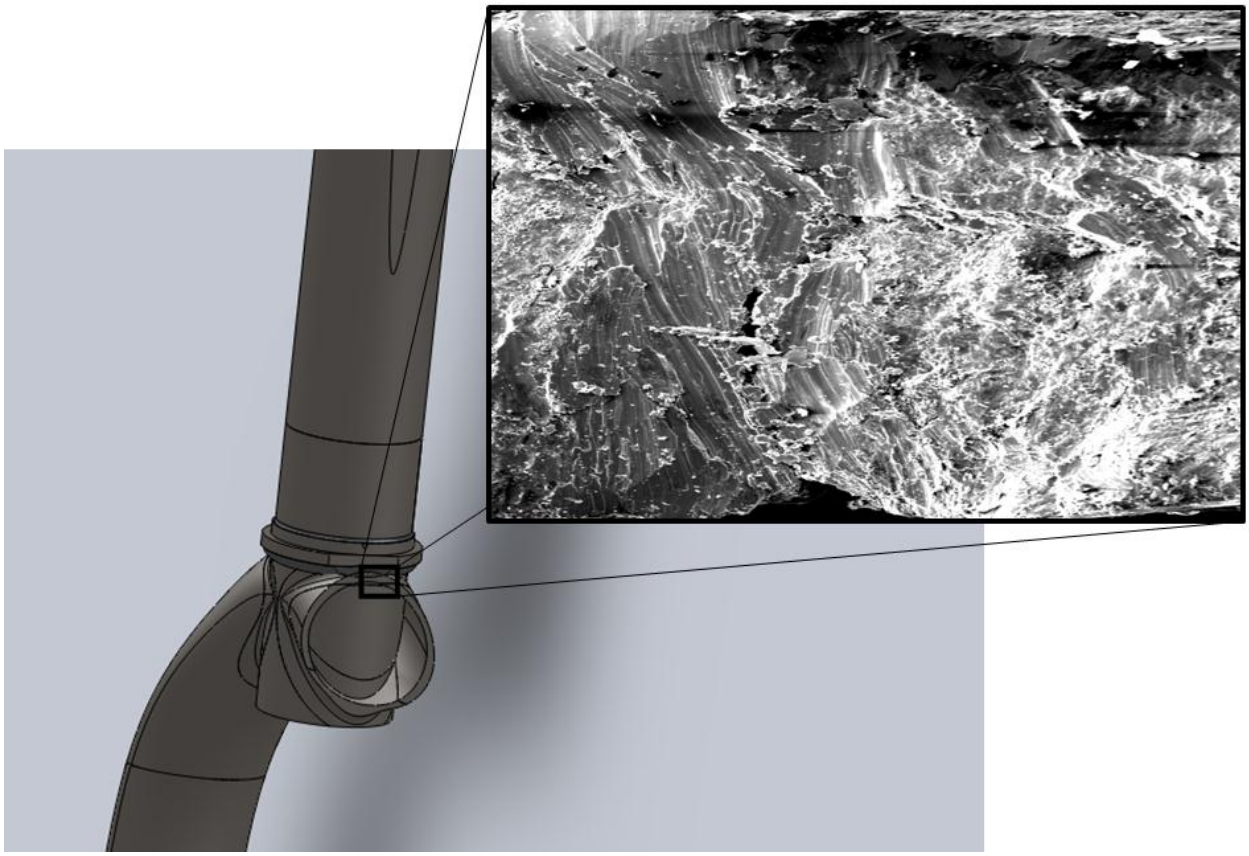

Figure 4-22: SEM Micrograph of Crack with Location on Fork.

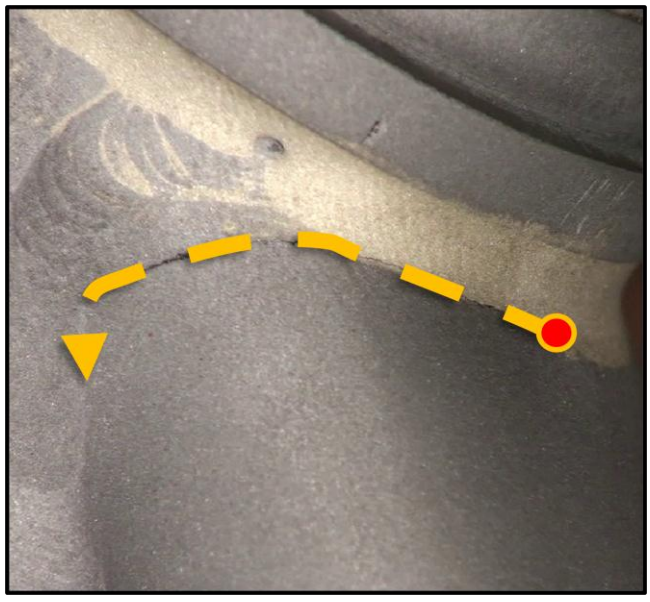

Figure 4-23: The Path of Crack Growth as Observed During Fatigue Testing.

4.3.4 Evaluation of Fatigue Crack Initiation and Propagation

Since the brazing filler covers the area where the crack first begins and propagates it was necessary to back-calculate the crack propagation rate to find out how many cycles it took for the applied stress to cause enough material damage for the crack to initiate. The calculation of this number of cycles could allow for the validation of the fatigue life model that was developed in ANSYS. In order to do this, the first fork that was failed in the fatigue testing machine was sectioned to extract the small piece that showed the fracture surface. This sample was cleaned with acetone and analyzed with the SEM. Micrographs with up to 1800x magnification were taken at the original point of failure and along the fracture surface. This fracture surface can be seen in Figure 4-24. A higher resolution image can be found in Appendix C.

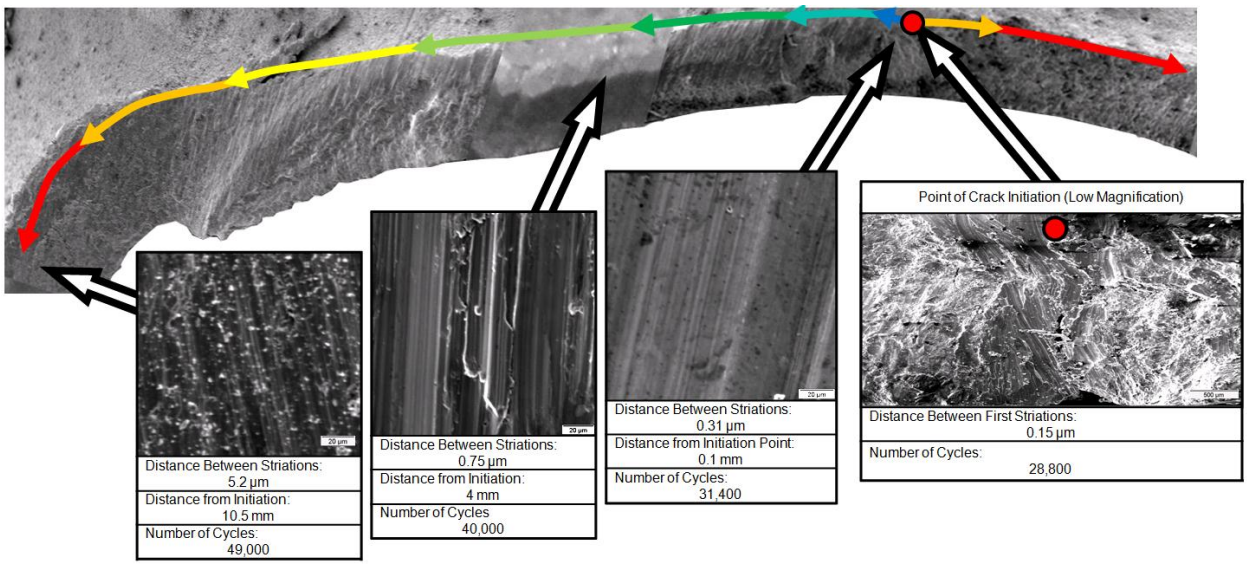

Figure 4-24: Images of Various Regions on the Fracture Surface.

The fractographs showed the striations that could be used to calculate crack propagation rates. Each striation spacing indicates the advance of the crack per one loading cycle in the fatigue testing machine. It was necessary to first determine the point of crack initiation before the analysis of the surface could be conducted. It was determined that the crack initiated at the surface as shown by the red circle in Figure 4-24.

For each point recorded by a micrograph a total crack length from the original point of failure was taken. The striation spacings were measured at various stages of crack growth.

The applied stress was also determined at each point by using the corresponding points in ANSYS from the FEA model. The stress intensity factor (K_{IC}) was then calculated using an equation relating it to the applied stress, σ, and the crack length, a.

$$K_{IC} \approx \sigma\sqrt{\pi a}$$

The change in the number of cycles (dN) was calculated by dividing the change in crack length (da) by striation spacing at each point along the fracture surface where a micrograph was taken. Since there were only a limited number of points taken along the fracture surface, it was assumed that measurements of the distance between the striations were constant from the point where it was measured to half way between that point and the previous and next point, as shown in Figure 4-25.

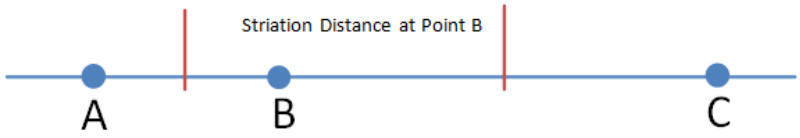

Figure 4-25: Method for Determining $\frac{da}{dN}$.

With $\frac{da}{dN}$ and K_{IC} a graph for the rate of crack growth based on the stress intensity factor was generated and is shown in Figure 4-26. The measured total crack length determined by the total number of cycles is shown in Figure 4-27. The data that generated these figures are shown in Table 4-3.

Table 4-3: Experimental Data for Fracture Surface Calculations.

Total Crack Length (m)	Distance Between Striations (m)	N (cycles)	dN	Applied Stress (MPa)	K (MPa*m^1/2)	d K	da/dN
5.00E-05	1.50E-07	0	667	157	1.967204362	0.297369	2.94E-08
1.00E-04	3.17E-07	3033	2366	158	2.799767133	0.752755	3.62E-06
1.50E-03	8.90E-07	5786	2753	165	11.32385756	0.484482	9.43E-07
4.00E-03	7.40E-07	11191	5405	196	21.96599554	0.49453	2.22E-06
8.50E-03	7.40E-07	18623	7432	266	43.45661791	0.055483	1.03E-06
1.50E-02	5.17E-06	19735	1112	212	46.00937296	0.283898	4.46E-05
2.00E-02	8.50E-06	20735	1000	143	35.83569729	-0.12196	1.25E-05

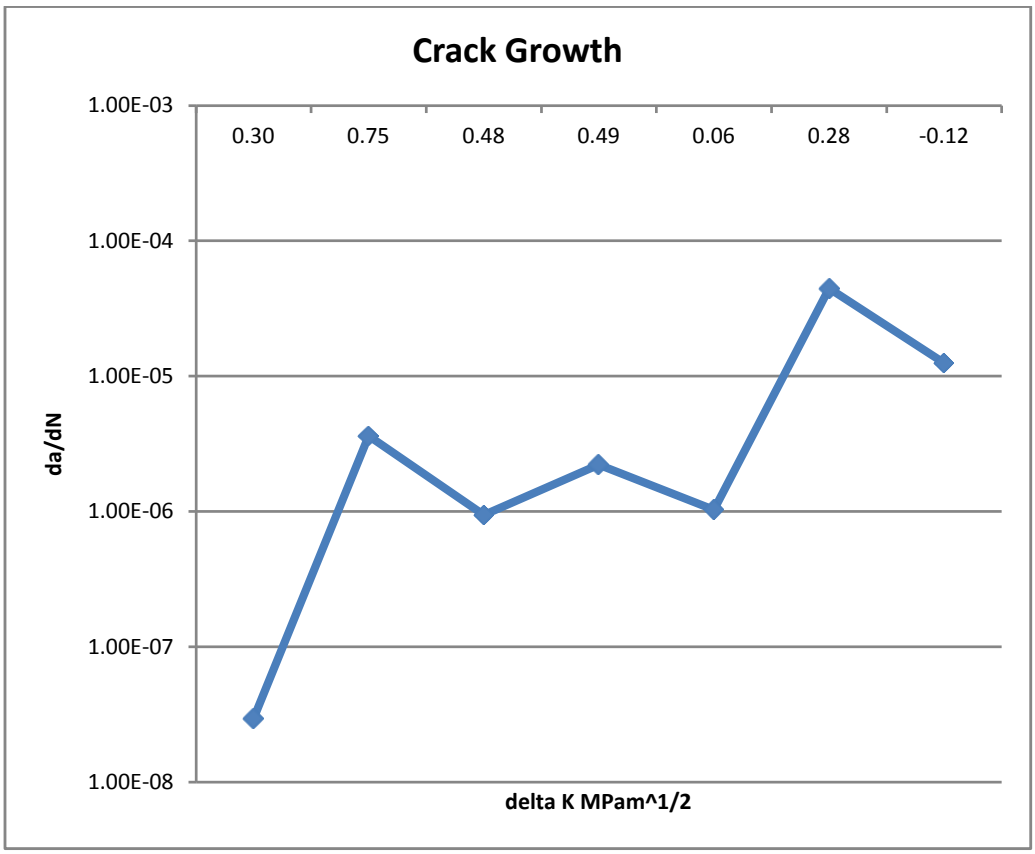

Figure 4-26: Crack Growth Based on Total Crack Length.

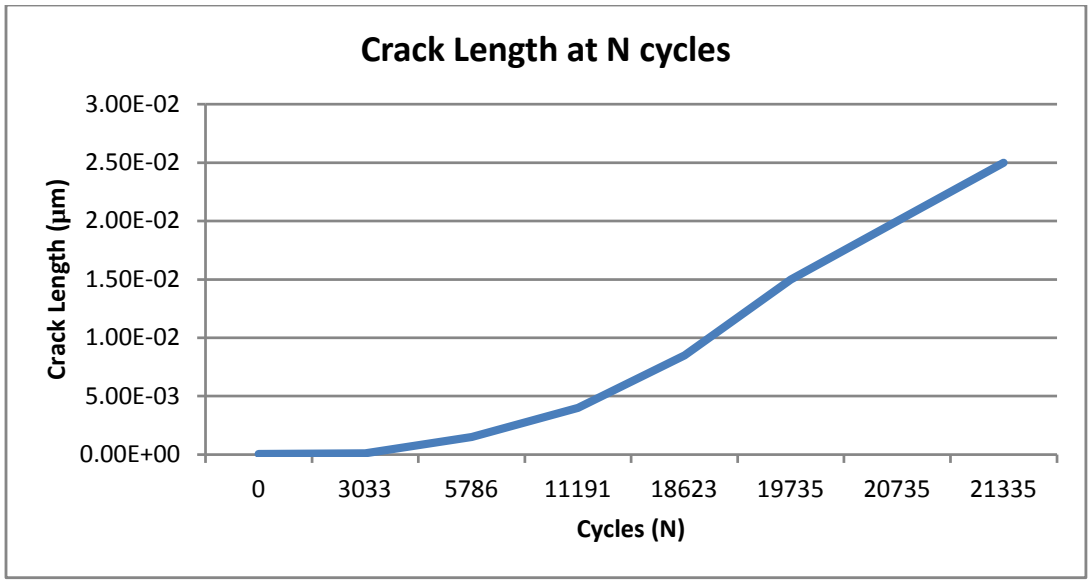

Figure 4-27: Crack Length with Increasing Number of Cycles.

From calculations using striation measurements it was determined that the crack reaches a point 8.5mm from the crack initiation site where it splits from the brazed region at 18,600 cycles. A high definition video camera was borrowed from the WPI Academic Technology Center and recorded the entire fork fatigue test. Each fatigue test generated approximately 120 GB of data. Using the video of the crack propagation it appears that the crack reaches this same point after approximately 47,400 cycles. From these observed results it can be inferred that the fork withstood around 28,800 cycles before the applied stress causes the crack to start propagating. It is also observed from the analysis discussed in Section 2.10.1 that the crack initiated in the HAZ of the fork blades. Once the crack initiates it propagates towards the front of the fork. When the crack breaks away from the brazing filler the rate rapidly increases and the fork fails completely. At this time, the crack also propagates on the other side of the initiation point and goes down the fork blade. In the future, more detailed SEM work can be done to determine whether or not a surface defect had an impact on when and how the crack initiated.

4.4 Fork Optimization

Utilizing the knowledge gained through microstructure analysis of the HAZ, the fracture surface, and the validated FEA fatigue life model, the project team set out to redesign the fork geometry, optimizing its fatigue life. This was done through design iteration in CAD, selection of a viable solution, and then experimental testing of its fatigue life.

4.4.1 Optimization Goals

In optimizing the fork, the primary goal was to ensure that the final product would pass the ASTM and CEN standards for bending fatigue testing of bicycle forks. In addition, our industry partner wanted to develop a solution that would not require them to alter their manufacturing process, ruling out any post welding heat treatment. It was expected that the fork would increase in weight, but minimization of this increase was also kept in mind. These goals led to the exploration of geometrical changes that would not only minimize the mean stress in the HAZ but, more importantly, move the stress concentration away from the HAZ, and possibly reduce the weight.

4.4.2 Fork Geometry Optimization

The front view of the fork along with the major parameters that could be changed to optimize the design are shown in Figure 4-28.

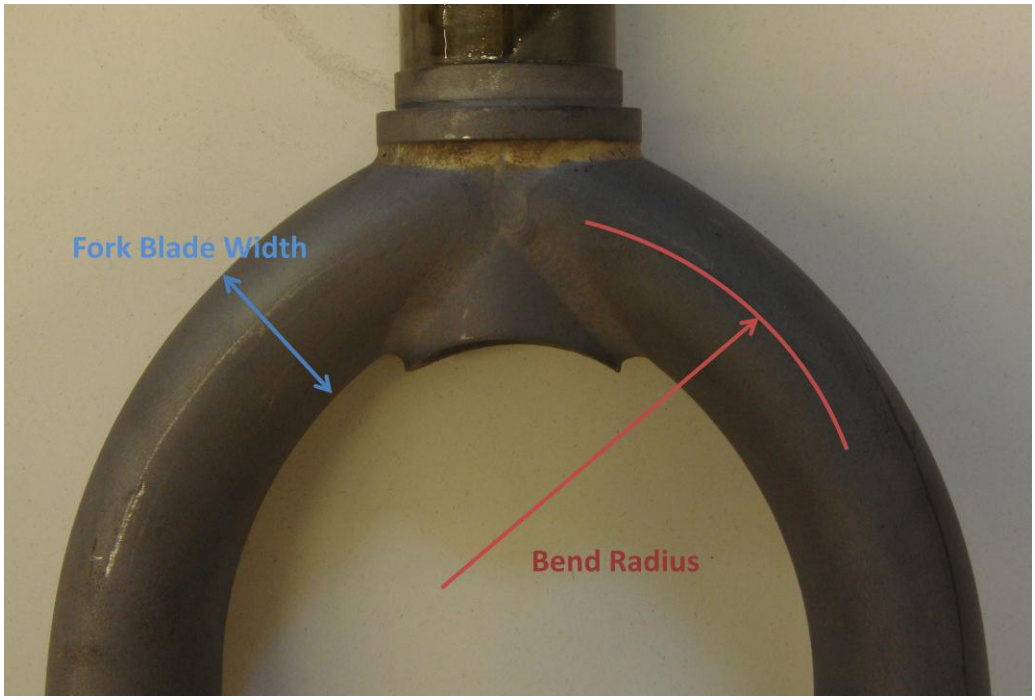

Figure 4-28: Fork Blade Width and Bend Radius.

The original fork geometry has a relatively small bend radius providing a poor loading path and creating additional stress in the HAZ. After speaking with the fork blade supplier, four options for wall thickness were selected. Two options were thinner than the current thickness and the other two were thicker. The supplier was also able to increase the diameter of the fork blade so two larger diameters were explored as well. Geometries for every combination of bend radius, wall thickness, and fork blade diameter were created and analyzed in our ANSYS fatigue life model. The results of the analyses were reviewed and a final geometry selected. The results for the final geometry, crack initiation at 95791 cycles, are shown in Figure 4-29.

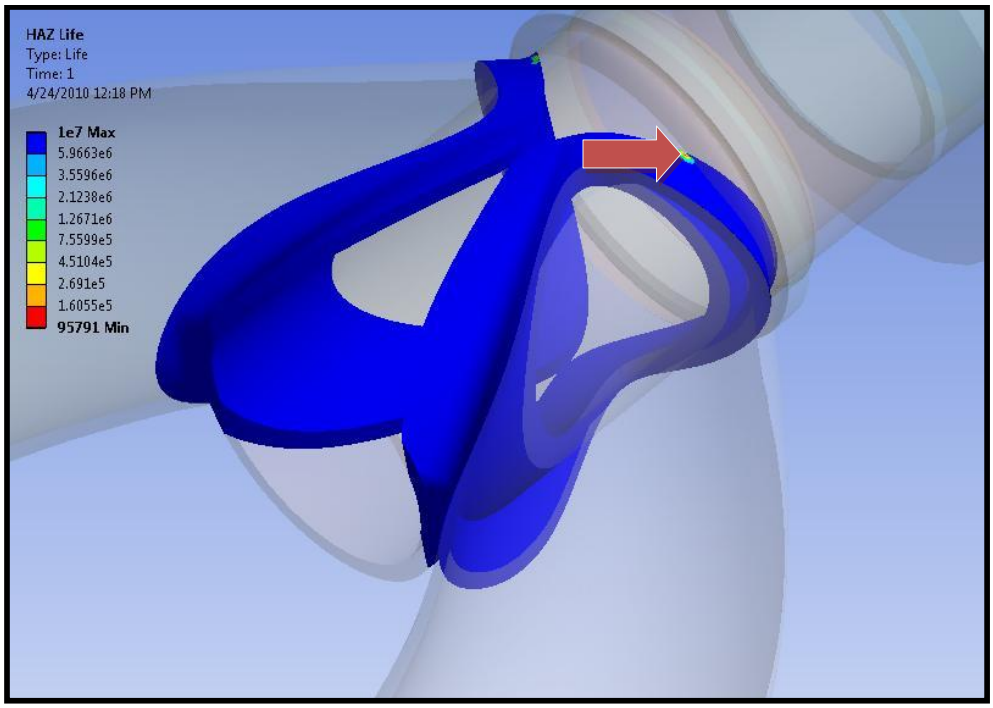

Figure 4-29: Fatigue Life Results of Optimized Geometry, Crack Initiation at 95791.

The fatigue life prediction was less than the 100,000 cycles required to pass the ASTM and CEN tests but, the model had been conservative in its prediction of the original geometry's life, and it was also predicting crack initiation, not when a visible crack would form. The optimized geometry uses a thinner wall than the original, which makes it a lighter design. Figure 4-30 shows a comparison of the original and optimized geometries in the front plane.

Figure 4-30: Comparison of Original and Optimized Geometry

4.4.3 Testing of Optimized Fork Geometry

The sponsor took the project team's recommendations and manufactured prototype forks of the optimized geometry. Upon receipt of the forks, they were tested to validate the redesigned geometry. Experimental testing showed that a crack did develop in the HAZ, but not until 136,000 cycles, well past the required 100,000 cycles for ASTM and CEN standards. Testing to final failure occurred in the steerer tube at 153,000 cycles before the crack in the HAZ could propagate through the fork blade. The optimized geometry has a fatigue life three times that of the original and has been recommended to the sponsor. They have now implemented the design and production forks are on their way for one last round of testing.

4.5 Material Solutions to Improve Fatigue Life

After looking at all the data it is evident that the welding process results in a weaker area in the HAZ, where a crack can form and propagate. Although the optimized geometry allowed the fork to pass the required tests, materials solutions could be implemented as well to further enhance the fatigue life. In order to induce more uniformity in the properties through the heat affected zone and the transition to the unaffected materials, post-weld treatment is necessary. There are various post-weld treatments, but the three most viable options to treat the fork are stress relieving, normalizing, or rapid-cooling heat treatment (Callister, 2007).

Stress relieving reduces residual stresses caused by the welding process. It involves heating the steel to a relatively lower temperature (below the eutectoid temperature) followed by air cooling. The entire fork could be stress relieved in a furnace, or an oxy acetylene torch can be used to stress relieve only the areas that were directly affected by the welding. Welding tradesmen that were consulted on this fork cracking problem suggested that the greatest chance to prevent the cracking was to stress relieve the heat affected region using an oxy acetylene torch at a temperature around 650°C (Carey, 2010). Normalizing would involve heating the 4130 steel to a temperature greater than 880°C. This results in a fine-grained pearlite in the heat affected zone and optimal toughness. The downside of normalizing is that if the entire fork is

normalized, the martensitic structure that is intended to be present in the fork blade would be replaced by the pearlite (Callister, 2007). If only the heat affected zone was normalized, there would be a sharp transition from the fine-grained pearlite to the tempered martensite. This transition would increase the probability for crack initiation and propagation. Normalizing is recommended over full annealing because full annealing would result in a coarse pearlite which would be too ductile for the bicycle application.

Rapid-cooling heat treatment, such as in water or oil would likely result in a martensitic structure that would have a very high UTS, but perhaps not be ductile enough to absorb the shocks from the bumps in the road. This would create a harsh ride for the cyclist, and if the fork was to fracture, it would most likely fracture catastrophically.

From research stress relieving, either for the entire fork or only around the heat affected zone, would be the most effective way to maintain the mechanical properties while decreasing the probability of crack formation. Introducing some of these improved tensile strengths into the FEA model predicts a new fatigue life of 10^6 - 10^7 cycles. However, further testing of all these options is necessary in order to draw a definitive conclusion.

5 Conclusions and Future Work

Table 5-1 shows the improvements made to the original fork resulted from the optimization of the geometry. By following the methodology put forth in the introduction, we were able to investigate the fatigue behavior of the failing bicycle fork, characterize the effects of the welding process on the materials' microstructures and properties for all of the fork components, and create and validate an FEA fatigue life prediction model of the fork utilizing experimentally determined materials data. This methodology allows for a framework for the design, analysis, and testing of the fatigue behavior of welded tube frames that can be used in many applications beyond bicycles. The fatigue life of the

material was improved by a factor of three allowing the new fork to meet the ASTM and CEN standards. The new forks have been set into production by our industry partner, and the fatigue testing machine will be used to test new bicycle forks of different materials and fabrication techniques.

Table 5-1: Comparison of Original Fork to Optimized Fork.

	Original Fork (cycles to)	**Optimized Fork (cycles to)**
FEA Predicted Crack Initiation	24,900	95,800
Crack Initiation Based on Striations	28,800	NA
Visible Crack (Exp. Testing)	47,400	136,000 (In HAZ)
Complete Failure (Exp. Testing)	62,800	154,000 (Steerer Tube Failure)

Future work with the optimized fork would include examining the fracture surface to revalidate the FEA model for the optimized geometry. Other future work would include the post-welding material treatment discussed in Section 4.5. More geometry refinement or consideration of different materials could further enhance the fatigue life of the forks.

6 Acknowledgements

We would like to thank the follow people for helping us make our project such a success:

Our Sponsor

Professor Diana Lados

Professor James Van de Ven

Torbjorn Bergstrom

David Botelho

Anastasios Gavras

Adriana Hera

Professor Boquan Li

Ellen Lincourt

Siamak Najafi

Professor Robert Norton

Randy Robinson

Adam Sears

Professor Richard Sisson

7 References

ASM International. (1990, December). ASM Metals Handbook Volume 1 - Properties and Selection: Irons Steels and High Performance Alloys. *I*(10th Edition).

AZoM. (2001, June 8). *Hydroforming Techniques*. Retrieved October 12, 2009, from AZoM™ - The A to Z of Materials and AZojomo - The "AZo Journal of Materials Online": http://www.azom.com/details.asp?ArticleID=540

Callister, W. D. (2007). *Materials Science and Engineering* (7th Edition ed.). New York, New York: John Wiley & Sons.

Carey, J. (2010, February 8). Post-welding Treatments. (N. Jannetti, Interviewer)

Efunda. (2010). *Vickers Hardness; Diamond Pyramid Hardness Converter*. Retrieved March 25, 2010, from Efunda: http://www.efunda.com/units/hardness/convert_hardness.cfm?HD=HV&Cat=Steel#ConvInto

Ho, A. (2007). *Temperature of a TIG Welder*. Retrieved March 25, 2010, from Hypertextbook: http://hypertextbook.com/facts/2007/AnthonyHo.shtml

Kalpakjian, S., & Schmid, S. R. (2006). *Manufacturing Engineering and Technology.* Upper Saddle River, NJ: Pearson Education.

Lados, D. (2010). Fatigue Crack Growth of Long and Small Cracks in Structural Materials. Worcester, Massachusetts, United States of America.

Lucas-Milhaupt. (2009). *How Brazing Works*. Retrieved April 24, 2010, from LucasMilhaupt: http://www.lucasmilhaupt.com/en-US/brazingfundamentals/howbrazingworks/

MatWeb. (2010). *AISI 1020 Steel, cold rolled.* Retrieved March 25, 2010, from MatWeb, Material Property Data: http://www.matweb.com/search/DataSheet.aspx?MatGUID=10b74ebc27344380ab16b1b69f1cffbb&ckck=1

Metal Suppliers Online, L. (n.d.). *4130 Alloy Steel Material Property Data Sheet*. Retrieved October 12, 2009, from Suppliers Online: http://www.suppliersonline.com/propertypages/4130.asp

Metals, A. F. (n.d.). *Low Alloy Wires*. Retrieved October 12, 2009, from Amfiller: http://amfiller.com/files/low_alloy_wire/lowalloywires.pdf

Miller Welds. (2009). *The GTAW (TIG) Process.* Retrieved March 25, 2010, from Millerwelds: http://www.millerwelds.com/resources/TIGhandbook/pdf/TIGBook_Chpt1.pdf

Minerals Management Service. (2010, March 10). *Cape Wind Project*. Retrieved April 5, 2010, from MMS: http://www.mms.gov/offshore/RenewableEnergy/CapeWind.htm

Reynolds Technology Ltd. (2009, May 5). Evaluation of Tube Materials.

Rusmee, P. (2005). *Fatigue Crack Growth*. Retrieved March 25, 2010, from The University of Utah: http://www.mech.utah.edu/~rusmeeha/labNotes/fatigue.html

Stanford University. (n.d.). *Steel Phase Diagram.* Retrieved March 25, 2010, from Stanford: http://bdml.stanford.edu/twiki/pub/Rise/SteelSelectionandTreatment/SteelPhaseDiagram.jpg

The Harris Products Group. (n.d.). *Technical Specifications Sheet: HARRIS SAFETY-SILV® 56 BRAZING FILLER METAL.* Retrieved March 25, 2010, from Harris products group: http://www.harrisproductsgroup.com/pdf/spec/BrazeAlloys/032008/Safety-Silv_56.pdf

The Lincoln Electric Company, Welding Services. (2000, June). *TIG WELD 4130!* Retrieved October 12, 2009, from Lincoln Electric: http://www.lincolnelectric.com/knowledge/articles/content/chrome-moly.asp

The University of Liverpool. (2000). *Transformation diagrams (CCT & TTT)*. Retrieved March 25, 2010, from Matter: http://www.matter.org.uk/steelmatter/metallurgy/7_1_2.html

True Temper Sports. (2009). *Tubing Specs - Versus*. Retrieved October 12, 2009, from True Temper Sports: http://www.truetemper.com/performance_tubing/verus.asp

University of Vermont. (2003). *ME 124 Experiment #7: The ASTM Tensile Test.* Retrieved March 25, 2010, from UVM: http://www.uvm.edu/~dhitt/me124/TensileTestNotes-II.pdf

Welding Accessories Technology. (2009). *Technical Details of Welding Normalized 4130 Chrome Moly (Chromoly) Steel for Race Cars*. Retrieved March 25, 2010, from WA Technologies: http://www.netwelding.com/4130_Tech_Details.htm

Welding Accessories Technology. (2009). *Welding "Heat Treated" 4130*. Retrieved March 25, 2010, from WA Technology: http://www.netwelding.com/Heat_Treated_4130.htm

Appendix A: ASTM Standard Test Methods for Bicycle Forks

Next Page

Designation: F 2273 – 03

An American National Standard

Standard Test Methods for Bicycle Forks[1]

This standard is issued under the fixed designation F 2273; the number immediately following the designation indicates the year of original adoption or, in the case of revision, the year of last revision. A number in parentheses indicates the year of last reapproval. A superscript epsilon (ε) indicates an editorial change since the last revision or reapproval.

1. Scope

1.1 These test methods describe mechanical tests for determining the following performance properties:

1.1.1 Compression Load,

1.1.2 Bending Load,

1.1.3 Impact Resistance, and

1.1.4 Fatigue Life.

1.2 The values stated in SI units are to be regarded as standard.

1.3 *This standard does not purport to address all of the safety concerns, if any, associated with its use. It is the responsibility of the user of this standard to establish appropriate safety and health practices and determine the applicability of regulatory limitations prior to use.*

2. Referenced Documents

2.1 *ASTM Standards:*

E 4 Practices for Force Verification of Testing Machines[2]

F 2043 Classification for Bicycle Usage[3]

3. Terminology

3.1 *Definitions of Terms Specific to This Standard:*

3.1.1 *bicycle fork (fork)*—the mechanism between the head tube and the front axle, including the steerer tube, crown, triple clamps, shock absorbers, lower tubes, and upper tubes.

3.1.2 *steerer tube*—the structural fork component typically housed inside the bicycle head tube, connected to the fork crown. The steerer tube transmits steering inputs from the rider to the fork and connects the fork to the bicycle frame by means of headset bearings.

3.1.3 *fork crown (crown)*—the primary structural fork component responsible for connecting the steerer tube to the fork upper tube(s) or fork blades.

3.1.4 *lower triple clamp*—See *fork crown*. The lower crown of a two-crown suspension fork.

3.1.5 *upper triple clamp*—the secondary structural fork component responsible for connecting the steerer tube to the upper tube(s).

3.1.6 *dropout*—the fork component used to support the front wheel(s) at the axle(s).

3.1.7 *dropout centerline*—the front hub mounting axis that passes through both right and left dropouts.

3.1.8 *tire clearance*—the distance between the top surface of the tire and the bottom surface of the fork crown with no compressive force applied to the fork.

3.1.9 *crown-to-axle clearance*—the distance between the fork axle centerline and the bottom surface of the crown with no compressive load applied to the fork.

3.1.10 *head set*—the bearing cup, cones, and other supporting components for allowing rotation of the fork about the steering axis.

3.1.11 *limit trip or stop*—a deflection of the fork, which exceeds the allowable displacement values and causes the machine to stop running.

4. Summary of Test Methods

4.1 *Compression Load Test*—This test method compresses the fork. The distance from the bottom surface of the crown to the axle centerline is measured.

4.2 *Bending Load Test*—This test method restrains a fork by the steerer tube and applies a load perpendicular to the steerer tube axis at the point on the dropout centerline centered between the two dropouts. The deflection at the dropout centerline perpendicular to the steerer tube axis is measured.

4.3 *Impact Resistance Test*—This test method restrains a fork by the steerer tube in horizontal orientation; a weight is dropped from a prescribed height onto a fixture attached to the fork dropouts in line with the dropout centerline. Permanent deflection at the dropout centerline perpendicular to the steerer tube axis is measured. The ability of the connection between the steerer tube and crown to support torque applied about the axis of the steerer tube is also checked.

4.4 *Fatigue Test*—This test method restrains a fork by the steerer tube and applies a fully reversed load perpendicular to the steerer tube axis at the point on the dropout centerline centered between the two dropouts. The test is stopped either at failure as defined by the criteria below or at 250 000 cycles, whichever come first. The number of cycles is recorded.

5. Significance and Use

5.1 These tests are used to determine the performance of a bicycle fork.

---

[1] These test methods are under the jurisdiction of ASTM Committee F08 on Sports Equipment and Facilities and is the direct responsibility of Subcommittee F08.10 on Bicycles.

Current edition approved July 10, 2003. Published July 2003.

[2] *Annual Book of ASTM Standards*, Vol 03.01.

[3] *Annual Book of ASTM Standards*, Vol 15.07.

6. Apparatus

6.1 *Compression Load Test*:

6.1.1 A fixture similar to Fig. 1 will be required.

6.1.2 The application of the load shall be applied to the top of the crown and along the centerline of the steerer tube (Fig. 1).

6.1.3 If necessary, then either a roller or linkage system shall be used to allow translation of the dropouts while the fork is compressed.

6.1.4 The distance from the dropout centerline to the nearest surface of the crown on steerer tube centerline shall be measured (Fig. 1).

6.2 *Bending Load Test*:

6.2.1 A fixture similar to that shown in Fig. 2 will be required to position a fork such that the steerer tube axis is horizontal and such that the fork is restrained by the steerer tube using bearings.

6.2.2 Bearing separation shall be 150 mm as shown in Fig. 2. Forks that require bearing installation not consistent with Fig. 2 shall be constrained in a manner consistent with their normal use.

6.2.3 The load shall be applied at the dropout centerline in a direction perpendicular to the steerer (Fig. 2).

6.2.4 The dropout centerline shall be free to translate parallel to the steerer tube with either a roller or linkage system.

6.2.5 Deflection at the dropout centerline shall be measured perpendicular to the steerer tube.

6.3 *Impact Resistance Test*:

6.3.1 A fixture similar to that shown in Fig. 2 will be required to position a fork such that the steered tube axis is horizontal and such that the fork is restrained by the steerer tube using bearings. The fork shall be constrained so that it cannot rotate about the steerer tube axis and the dropout centerline is maintained horizontal.

6.3.2 Bearing separation shall be 150 mm, as shown in Fig. 3. Forks that require bearing installation not consistent with Fig. 3 shall be constrained in a manner consistent with their normal use.

6.3.3 The application of the impact shall be perpendicular to the steerer tube axis at the dropout centerline, centrally located between the dropouts (Fig. 2).

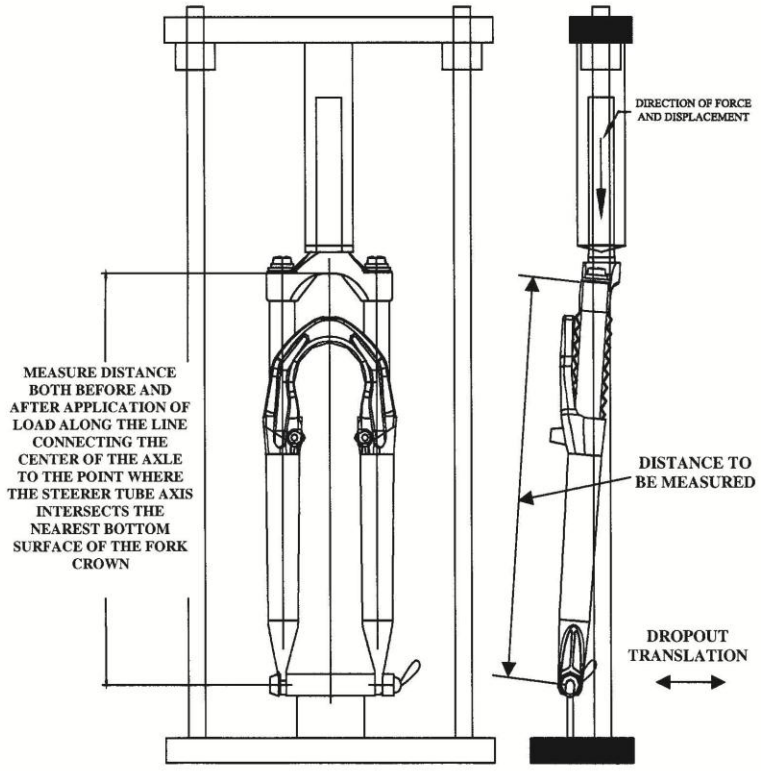

NOTE—For some fork designs, a dropout support that allows translation may be required.

FIG. 1 Typical Compression Test Apparatus

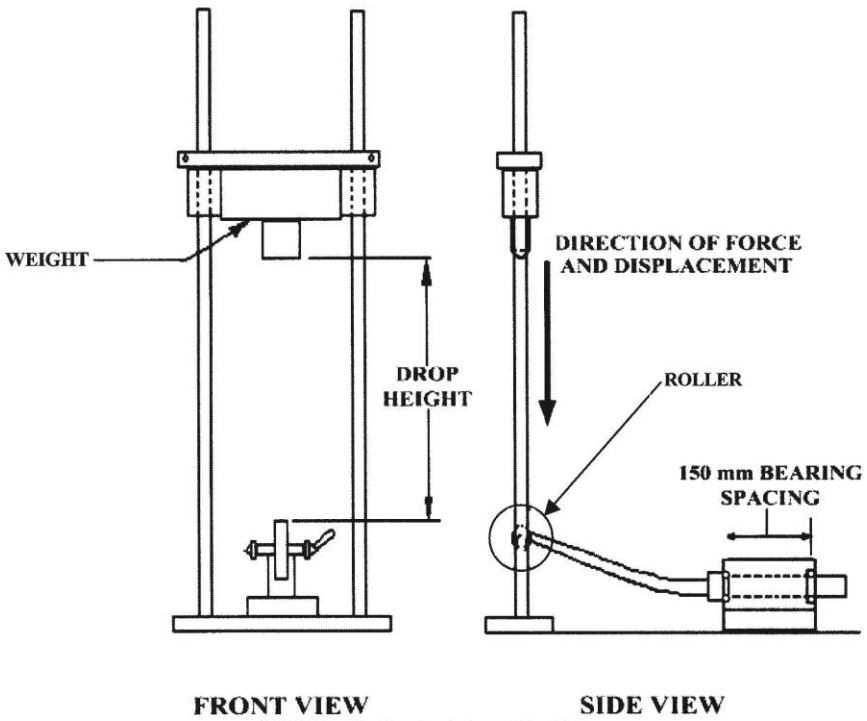

FIG. 2 Bending Load and Impact Test Setup

6.3.4 A roller is required (Fig. 2) and must be of sufficient diameter to ensure that the impactor comes to rest on the roller following impact.

6.3.5 The height of the roller above the support base should be such that the roller does not contact the base during the test.

6.3.6 Deflection at the dropout centerline in a direction perpendicular to the steerer tube axis shall be measured.

6.3.7 An apparatus capable of checking whether the connection between the steerer tube and crown can support a prescribed torque applied to the steerer tube about its axis is also required.

6.4 *Fatigue Test*:

6.4.1 A fixture similar to Fig. 3 will be required to restrain the suspension fork by the steerer tube using bearings as shown.

6.4.2 Bearing separation shall be 150 mm as shown in Fig. 3. Forks that require bearing installation not consistent with Fig. 3 shall be constrained in a manner consistent with their normal use.

6.4.3 The force shall be applied at the dropout in a direction perpendicular to the axis of the steerer tube. An actuator that is capable of providing a fully reversed force of constant amplitude will be used.

6.4.4 The dropout centerline shall be free to translate perpendicular to the direction of load application.

6.4.5 The ability of the actuator to produce the required amount of force shall be verified per Practices E 4.

7. Test Specimens

7.1 *Preparation of Specimens*:

7.1.1 The forks shall be set to the maximum fully extended length.

7.2 *Fork Adjustment*:

7.2.1 The fork shall be tested with the standard spring rate and all preload and damping shall be adjusted to the minimum settings.

7.2.2 All fasteners shall be assembled to manufacturer's specifications.

8. Calibration and Standardization

8.1 The direction of load application shall be within ±2°.

8.2 The accuracy of load application shall be within −0 % to +5 % of the specified value unless specified otherwise.

8.3 The accuracy of all distance and displacement measurements shall be within ±1 mm unless specified otherwise.

9. Conditioning

9.1 Tests are to be performed within the temperature range of 18 to 35°C.

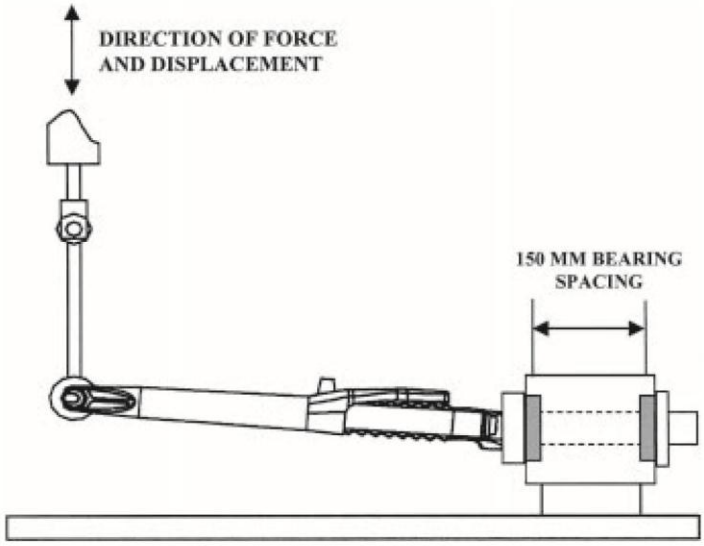

FIG. 3 Fatigue Test Setup

9.2 All tests are to be performed on new forks with production stock settings except as noted.

10. Procedure

10.1 *Compression Load Test*:

10.1.1 Adjust spring preload and damping to the minimum settings.

10.1.2 Install fork into the compression fixture.

10.1.3 Measure the distance from the axle centerline to the nearest bottom surface of the crown on the steerer tube centerline and record.

10.1.4 Apply a specified compression load and hold for measurement.

10.1.5 Remeasure the distance from the dropout centerline to the bottom of the crown and record.

10.2 *Bending Load Test*:

10.2.1 Adjust spring preload and damping to the minimum settings.

10.2.2 Install the fork into the restraining fixture and adjust the preload on the headset bearings as installed normally.

10.2.3 Apply an initial load of 100 N. Zero the deflection measurement apparatus.

10.2.4 Apply an increasing load at a rate not to exceed 100 N/s until a specified bending load is obtained. If manual loading is used, then the weight must be applied in at least ten equal increments.

10.2.5 Measure the deflection at the dropout centerline between 60 to 90 s after the specified bending load is applied.

10.2.6 Remove the load until a load of 100 N is obtained.

10.2.7 Measure and record the fork deflection at the dropout centerline (permanent set) perpendicular to the axis of the steerer tube.

10.3 *Impact Resistance Test*:

10.3.1 Install the fork in the fixture using typical headset bearings. Slight over tightening of the bearings is acceptable to prevent the fork from freely rotating.

10.3.2 Install the roller in the fork.

10.3.3 Rest the weight on the roller.

10.3.4 Zero the deflection measurement apparatus.

10.3.5 Raise the weight a specified drop height number one above the roller in the unweighted position.

10.3.6 Release the weight, letting it freely fall and impact the roller. The weight will bounce on the roller until it comes to rest. If the roller contacts the support base, then the test is invalid.

10.3.7 Measure and record the permanent deflection perpendicular to the steerer tube with the weight resting on the roller.

10.3.8 Repeat the test at a specified drop height number two. If the roller contacts the support base, then the test is invalid.

10.3.9 Check the connection between the steerer tube and crown by applying a specified torque about the axis of the steerer tube with the crown restrained. Record whether or not the steerer tube rotated in the crown and if so, then the torque value that initiated rotation.

10.4 *Fatigue Test*:

10.4.1 Install a typical headset into the Head Tube Apparatus (Fig. 3).

10.4.2 Install a typical headset crown race onto the fork.

10.4.3 Install the fork/crown race assembly into the head tube/headset assembly.

10.4.4 The headset shall be adjusted using typical bicycle assembly practices. The bearings shall allow free rotation of the fork without any looseness or free play.

10.4.5 Connect actuator mechanism to fork dropouts (Fig. 3).

10.4.6 Begin applying a specified fully reversed sinusoidal load at 1 Hz and measure the peak displacements after 1000 cycles. If desired, then gradually increase the frequency until the running peak displacements determined as the peak displacements after an additional 1000 cycles of loading are within ±3 % of the displacement at 1 Hz. (See Fig. 4.)

10.4.7 The load shall be monitored to an accuracy of −0 %, +5.0 % through either strain gages attached to the fork or a load cell. Likewise, the displacement shall be monitored to within 5 %.

10.4.8 The test shall be stopped when failure occurs. In using force control to perform the test, failure is determined through a multistep procedure.

10.4.8.1 The first running peak displacements are determined as the peak displacements achieved after the first 1000 cycles of load. When either of the peak displacements increase by 0.76 mm compared to the corresponding first running peak displacements, the test is stopped.

10.4.8.2 The test is restarted to determine second running peak displacements achieved after the first 1000 cycles of additional load. During this period, a visual inspection is performed. If any cracks in structural components are apparent, then the test is stopped and the number of cycles to failure is recorded as the total number of cycles to reach the first stop. If no cracks are apparent, then the test is continued and stopped when either of the peak displacements increase by 0.76 mm compared to the corresponding second running peak displacement.

10.4.8.3 The test is restarted to determine third running peak displacements achieved after the first 1000 cycles of additional load. During this period, a visual inspection is performed. If any cracks in structural components are apparent, then the test is stopped and the number of cycles to failure is recorded as the total number of cycles to reach the second stop. If no cracks are apparent, then the test is continued and stopped when either of the peak displacement increases by 0.76 mm compared to the corresponding third running peak displacement. Failure is recorded as the total number of cycles to reach the third stop.

10.4.9 The test may be suspended at 250 000 cycles if this number of cycles is achieved before failure occurs.

10.4.10 If the machine is shut down for any reason before a stop is reached, then no settings should be changed when the test is resumed.

10.4.11 Record the peak displacements after 1000 cycles at 1 Hz; the running peak displacements after an additional 1000 cycles if the frequency of the test is greater than 1 Hz; the total number of cycles to each of the stops; the results of the visual inspection following each of the stops; and the number of cycles to failure.

11. Report

11.1 A test report shall be prepared to include the following:

11.1.1 Applicable Test Method Specification,

11.1.2 The manufacturer of the fork(s) tested,

11.1.3 The model, year, and serial number of the fork(s) tested,

11.1.4 The date and location of the test,

11.1.5 The name of the person and entity conducting the test,

11.1.6 A description of all instruments used to make load and distance or displacement measurements including identifying information such as the serial number or model number, or both,

11.1.7 Either the calibration record or a reference to such a record of all instruments used to make load and displacement measurements,

11.1.8 All measurements required by the test method and the results of those measurements, and

11.1.9 A detailed description of any failure including the specific component that failed and the location of failure.

12. Rationale

12.1 The compression test was conceived for suspension forks so that if the springs, dampers, or other components fail during high compression loads, then the tire shall not contact the fork crown. Although this test is primarily for suspension forks, this test should be conducted on all forks since rigid forks can fail under high compression loads as well.

12.2 The bending test was created to assure that the fork could withstand a specified bending load developed during a nonimpact situation. In such a situation, the fork should neither permanently deform nor break from normal static riding loads.

12.3 The impact test is to assure an energy absorbing capacity of the fork without fracture when encountering impact loads that could occur during either intended or unintended bicycle maneuvers. The fork should permanently deform a specified amount as it absorbs impact loads without having any components either break or separate. The test to check for torque supported by the steerer tube is to prevent loss of steering control caused by an impact that has loosened the press fit of the crown and steerer tube joint.

12.4 The fatigue test is to assure that the fork can tolerate a specified number of repetitive load cycles without component failure as indicated by the formation of cracks. Inasmuch as riding over either paved or unpaved surfaces can develop time varying loads that occur repeatedly as a result of inertial accelerations imposed by surface irregularities, assuring a specified lifetime in a fatigue environment is important to maintaining the structural integrity of the fork.

13. Precision and Bias

13.1 Precision and bias evaluations have not been conducted for these test methods. When such data becomes available, a precision and bias section will be added.

14. Keywords

14.1 bending load test; bicycle forks; compression load test; fatigue test; impact resistance test

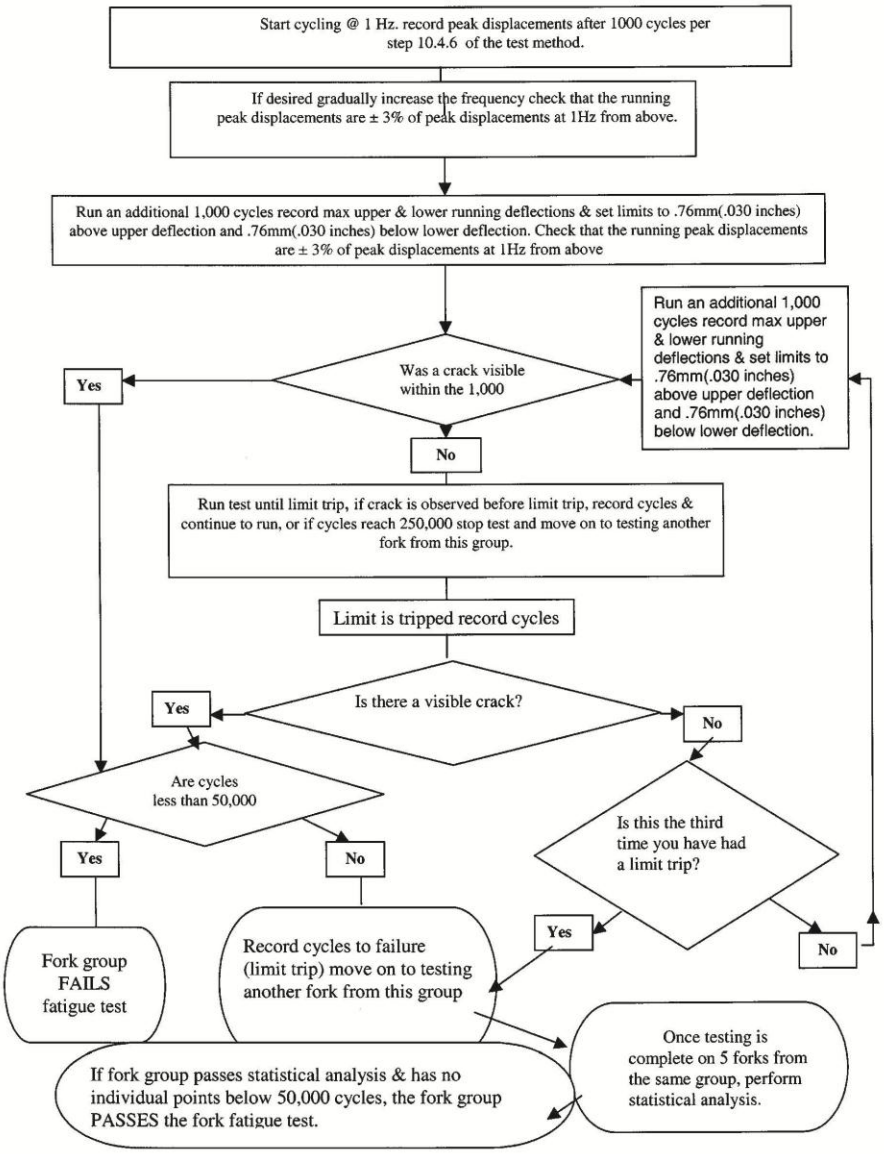

NOTE—This is an aid for following the Test Methods. In case of conflict, follow the wording in the Test Methods.

FIG. 4 Flowchart for Fork Fatigue Testing

Appendix B: Materials Samples and Test Results

Heat Affected Zone Cross Section

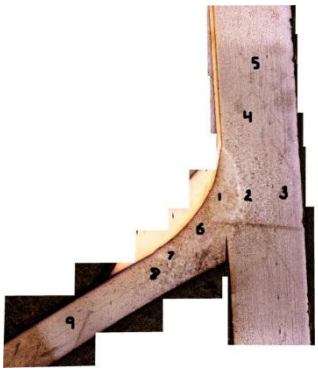

Point	HK	HV	HK	HV	HK	HV		Average HV		Standard Dev
1	287	275	297	285	294	282		280.6667	Weld	5.131601
2	258	244	289	277	295	284		268.3333	ST HAZ 1	21.36196
3	235	220	239	225	229	213		219.3333	ST HAZ 2	6.027714
4	267	254	252	239	263	250		247.6667	ST HAZ 1	7.767453
5	225	208	218	202	211	194		201.3333	ST HAZ 2	7.023769
6	287	275	297	285	294	282		280.6667	Weld	5.131601
7	322	314	322	314	290	278		302	FB HAZ 1	20.78461
8	276	264	262	248	267	255		255.6667	FB HAZ 2	8.020806
9	261	248	244	231	263	249		242.6667	FB HAZ 2	10.11599
						364			Unaffected	

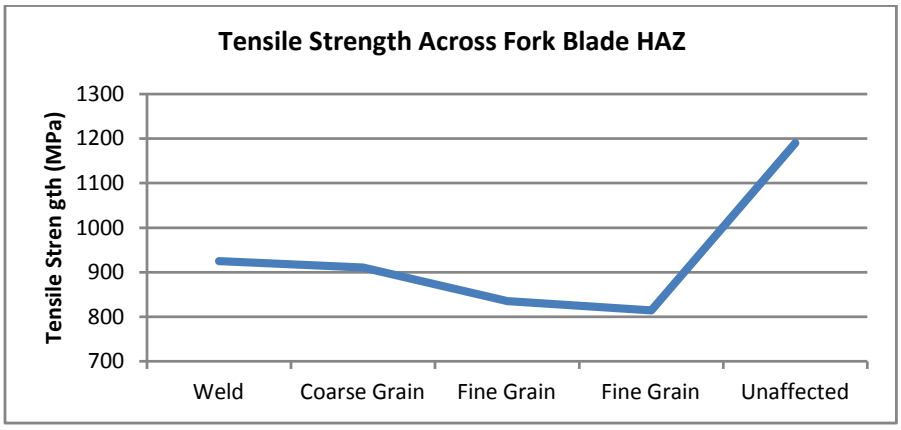

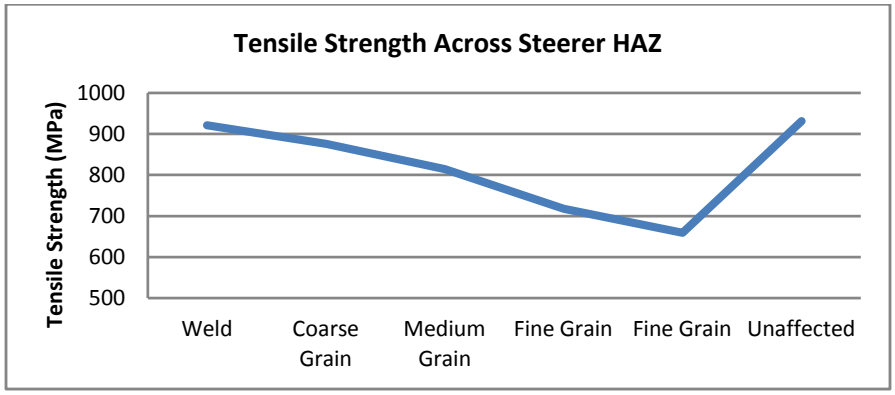

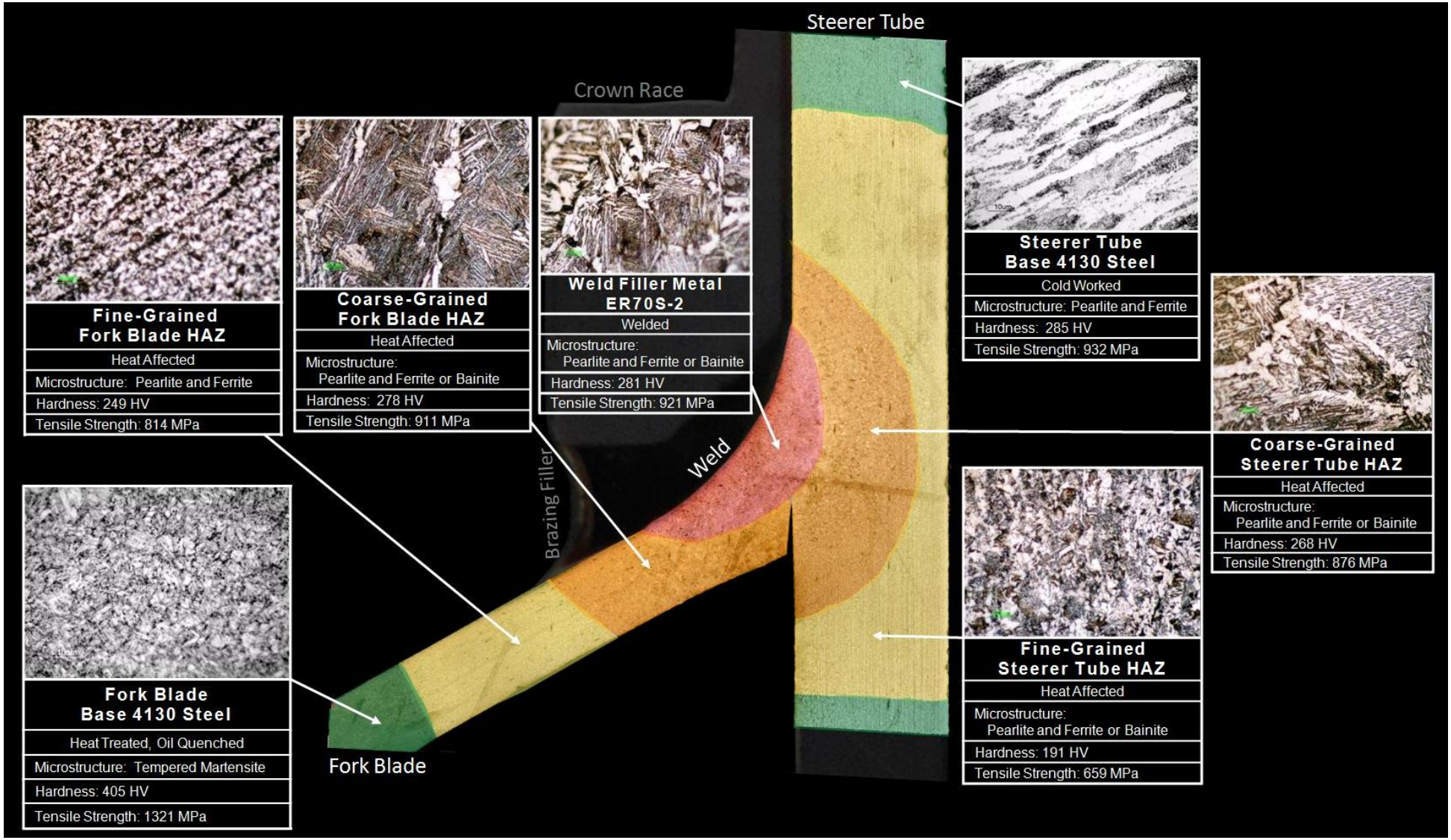
Steerer Tube
Crown Race
Fine-Grained
Fork Blade HAZ
Heat Affected
Microstructure: Pearlite and Ferrite
Hardness: 249 HV
Tensile Strength: 814 MPa
Coarse-Grained
Fork Blade HAZ
Heat Affected
Microstructure:
Pearlite and Ferrite or Bainite
Hardness: 278 HV
Tensile Strength: 911 MPa
Weld Filler Metal
ER70S-2
Welded
Microstructure:
Pearlite and Ferrite or Bainite
Hardness: 281 HV
Tensile Strength: 921 MPa
Steerer Tube
Base 4130 Steel
Cold Worked
Microstructure: Pearlite and Ferrite
Hardness: 285 HV
Tensile Strength: 932 MPa
Coarse-Grained
Steerer Tube HAZ
Heat Affected
Microstructure:
Pearlite and Ferrite or Bainite
Hardness: 268 HV
Tensile Strength: 876 MPa
Brazing Filler
Weld
Fork Blade
Base 4130 Steel
Heat Treated, Oil Quenched
Microstructure: Tempered Martensite
Hardness: 405 HV
Tensile Strength: 1321 MPa
Fork Blade
Fine-Grained
Steerer Tube HAZ
Heat Affected
Microstructure:
Pearlite and Ferrite or Bainite
Hardness: 191 HV
Tensile Strength: 659 MPa

Steerer Tube Gradient Top to Bottom

Knoop	Vickers	Rockwell B	
HK	HV	HR	
228	212	93.9	
228	212	93.9	
219	203	92.5	
176	161	83.6	ST HAZ 2
215	199	91.8	ST HAZ 2
255	242	97.8	ST HAZ 1
272	260	100	ST HAZ 2
275	263	100	ST HAZ 1
252	239	97.4	ST HAZ 1
193	177	87.7	ST HAZ 2
220	203	92.7	
222	206	93	
227	210	93.8	
216	200	92	

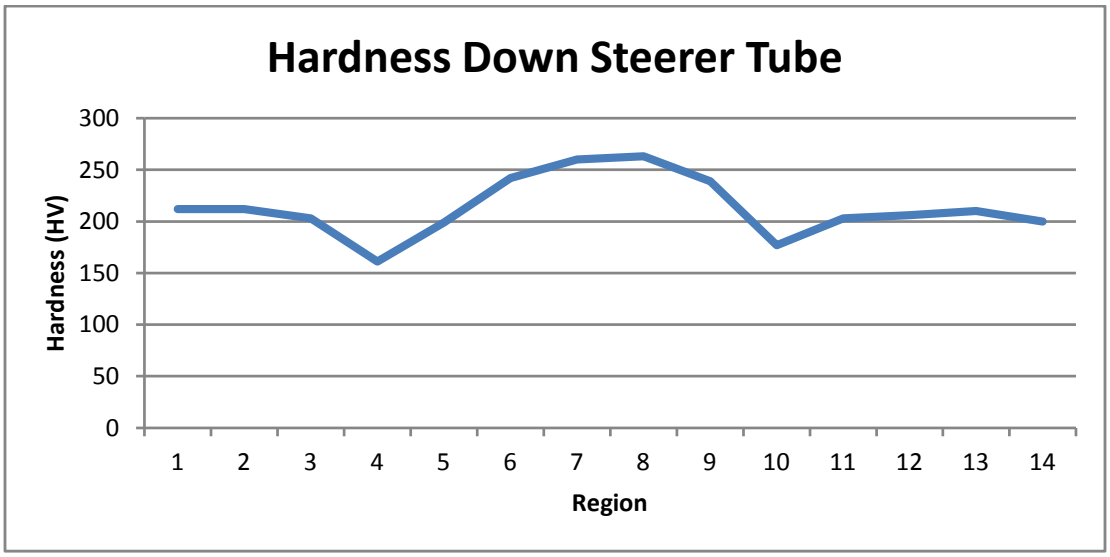

Section of Front Face of Fork with Welds

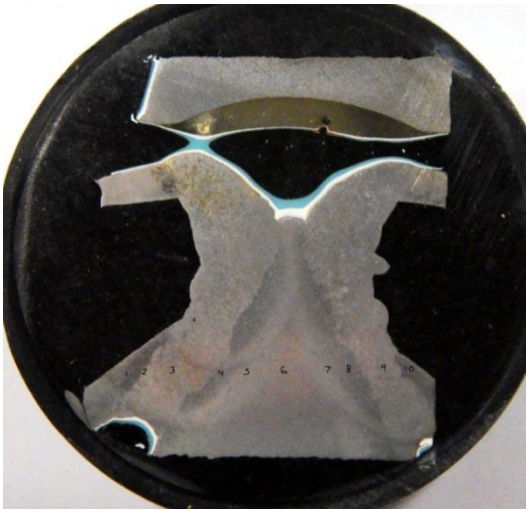

Point	HK	HV	HK	HV	HK	HV			Average HV	Standard Dev		HB	UTS
1	378	369	397	388	386	377			378	9.539392	FB HAZ 1	358	1235.1
2	346	339	326	319	300	289			315.666667	25.16611	FB HAZ 1	300	1035
3	300	287	351	345	354	347			326.333333	34.07834	Weld	309	1066.05
4	278	266	275	263	281	268			265.666667	2.516611	ST HAZ 1	252	869.4
5	267	254	242	228	250	237			239.666667	13.20353	ST HAZ 1	227	783.15
6	225	209	214	198	221	204			203.666667	5.507571	ST HAZ 2	194	669.3
7	250	236	270	258	261	247			247	11	ST HAZ 1	235	810.75
8	315	306	294	282	300	289			292.333333	12.34234	ST HAZ 1	277	955.65
9	276	264	285	273	301	290			275.666667	13.20353	Weld	262	903.9
10	406	395	442	426	416	403			408	16.09348	FB HAZ 1	386	1331.7

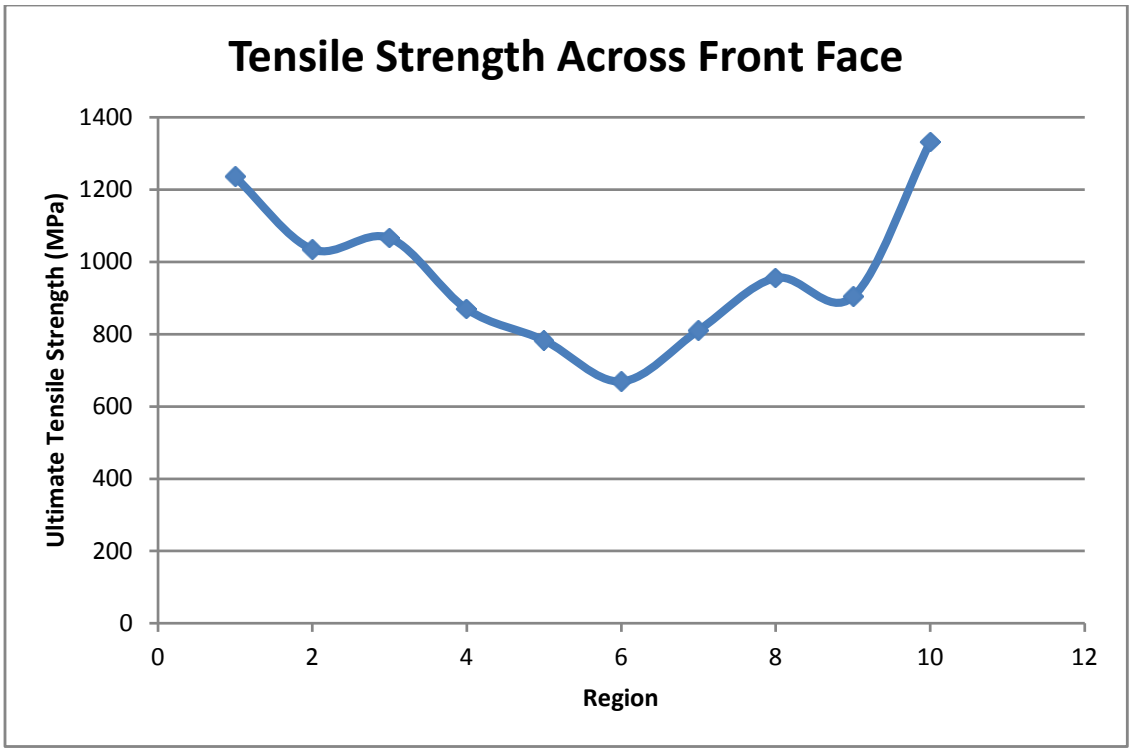

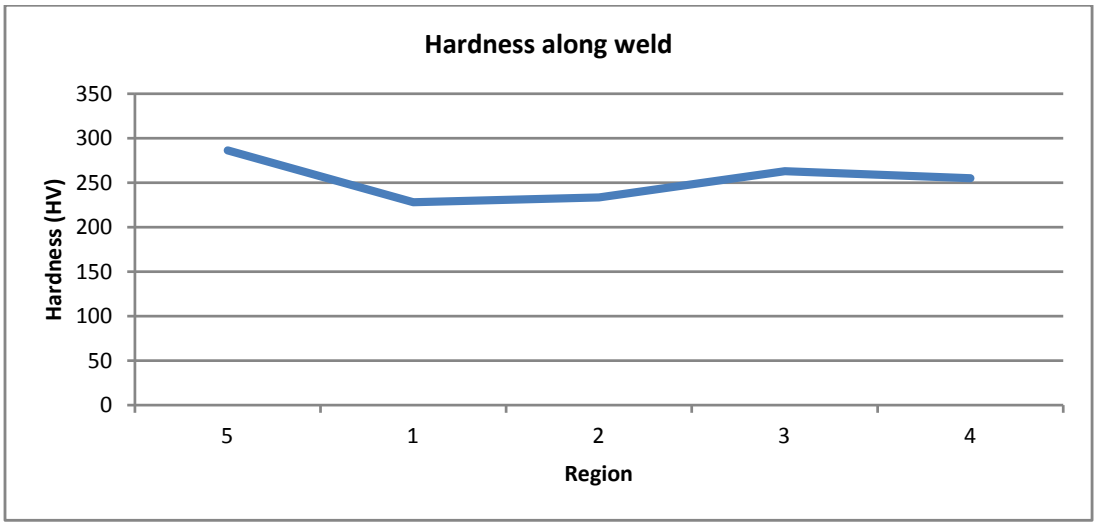

	Average Vickers	Brinell	UTS
FB HAZ 1	367.2222	348	1200.6
Weld	301	286	986.7
ST HAZ 1	261.1667	248	855.6
ST HAZ 2	203.6667	193	665.85

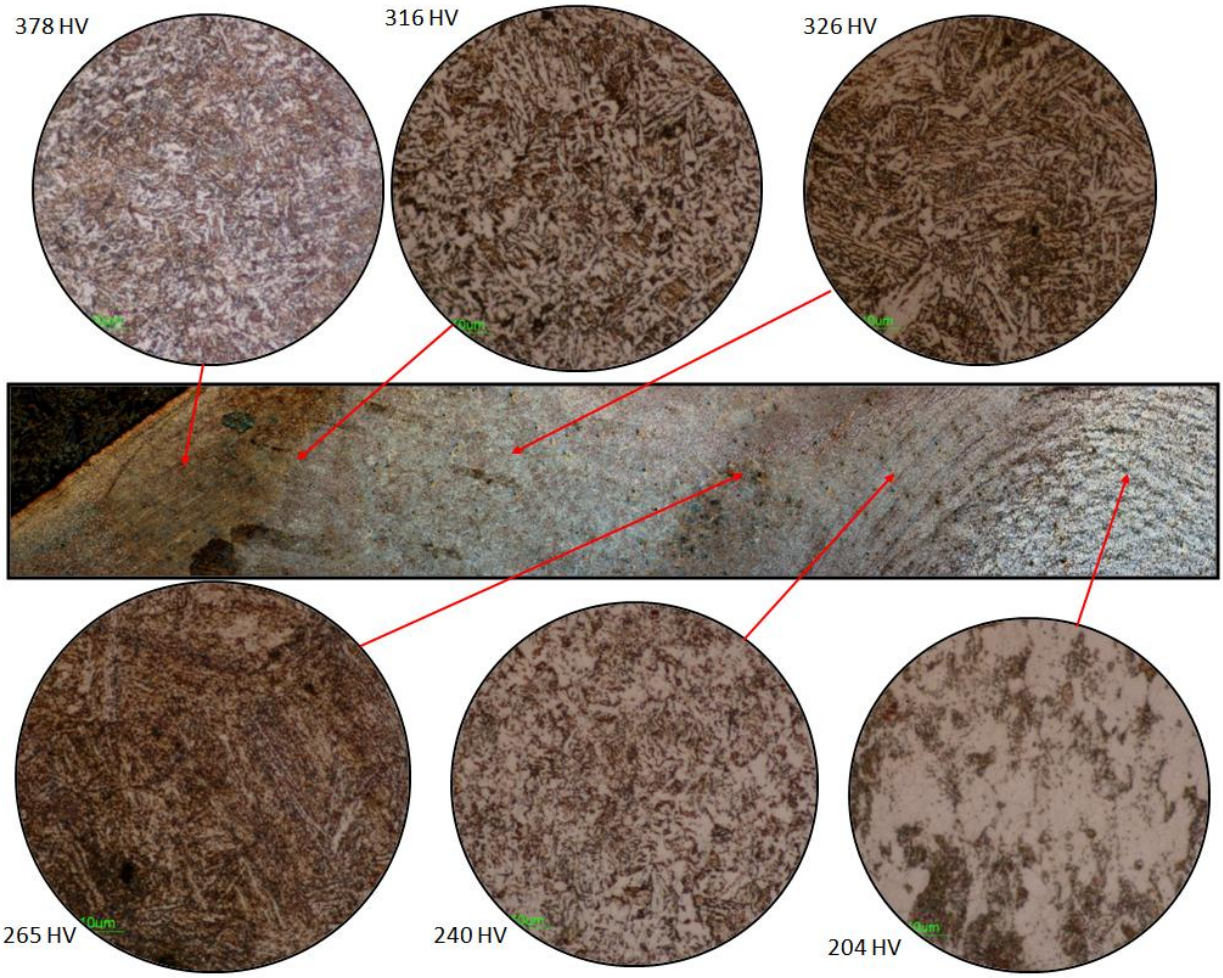
378 HV
316 HV
326 HV
265 HV
240 HV
204 HV

Oblique Section through the Heat Affected Zone

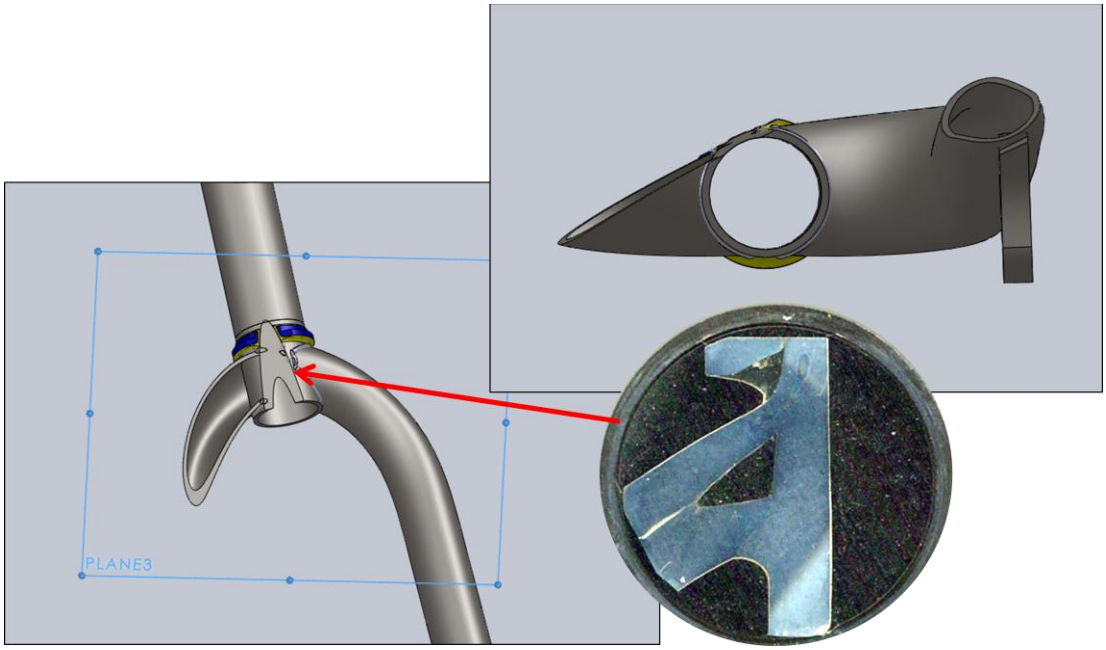

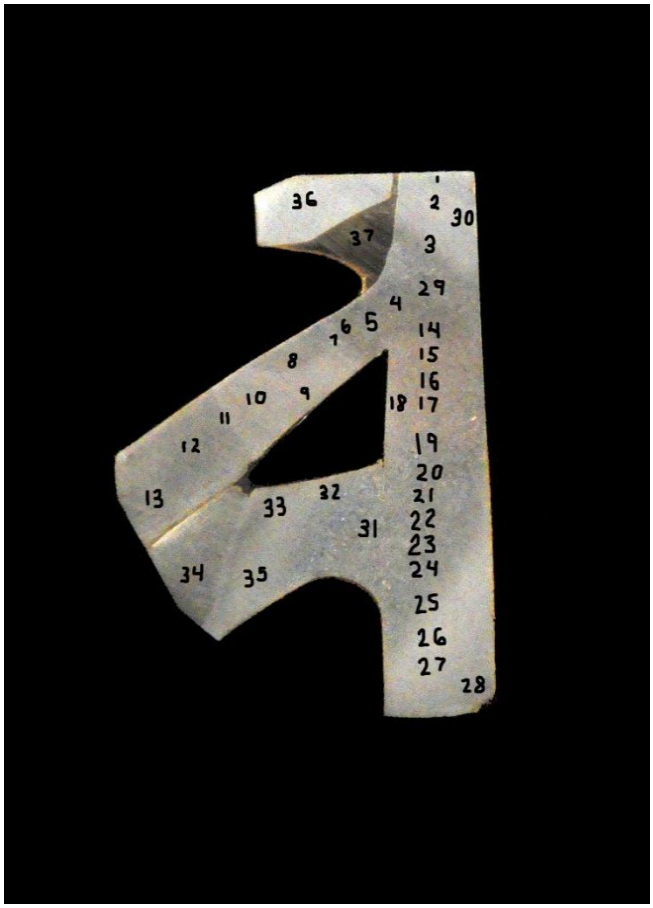

Point	HK	HV	HK	HV	HK	HV		Average HV	Standard Dev	
1	230	214	224	208	223	206		209	4.163332	ST HAZ 2
2	226	210	234	219	254	240		223	15.3948	ST HAZ 2
3	244	230	259	245	269	256		244	13.05118	ST HAZ 2
4	287	275	274	261	281	268		268	7	Weld
5	248	235	231	215	235	220		223	10.40833	FB HAZ 2
6	208	192	239	226	234	219		212	17.95364	FB HAZ 2
7	262	249	250	237	264	251		246	7.571878	FB HAZ 2
8	210	194	234	220	225	209		208	13.05118	FB HAZ 2
9	247	233	243	229	237	223		228	5.033223	FB HAZ 2
10	231	215	236	221	237	223		220	4.163332	FB HAZ 2
11	264	252	290	279	281	268		266	13.57694	FB HAZ 2
12	306	295	335	327	337	330		317	19.39931	Un FB
13	343	336	336	329	331	323		329	6.506407	Un FB
14	280	268	274	261	300	289		273	14.57166	ST HAZ 1
15	293	282	321	312	308	298		297	15.01111	ST HAZ 1
16	291	279	320	312	281	268		286	22.89833	ST HAZ 1
17	255	242	295	283	272	259		261	20.59935	ST HAZ 1
18	308	298	289	277	280	268		281	15.3948	ST HAZ 1
19	282	270	309	299	386	274		281	15.71623	ST HAZ 1
20	281	268	282	269	270.3	258		265	6.082763	ST HAZ 1
21	287	275	299	288	304	294		286	9.712535	ST HAZ 1
22	302	291	289	277	315	306		291	14.50287	Weld
23	316	307	342	336	312	303		315	18.00926	Weld
24	307	297	306	296	299	288		294	4.932883	Weld
25	270	257	280	267	311	301		275	23.06513	ST HAZ 1
26	286	274	270	257	289	277		269	10.78579	ST HAZ 1
27	274	261	261	247	262	248		252	7.81025	ST HAZ 2
28	223	206	209	192	214	197		198	7.094599	ST HAZ 2
29	274	261	313	303	297	285		283	21.07131	Weld
30	236	222	244	231	221	205		219	13.20353	ST HAZ 2
31	289	277	308	298	272	259		278	19.51922	FB HAZ 1
32	271	258	296	284	310	299		280	20.74448	FB HAZ 1
33	271	259	249	236	259	246		247	11.53256	FB HAZ 2
34	322	314	347	341	335.4	328		328	13.50309	Un FB
35	313	304	270	258	274	261		274	25.73584	FB HAZ 2
36	267	255	306	296	304	293		281	22.85461	Crown

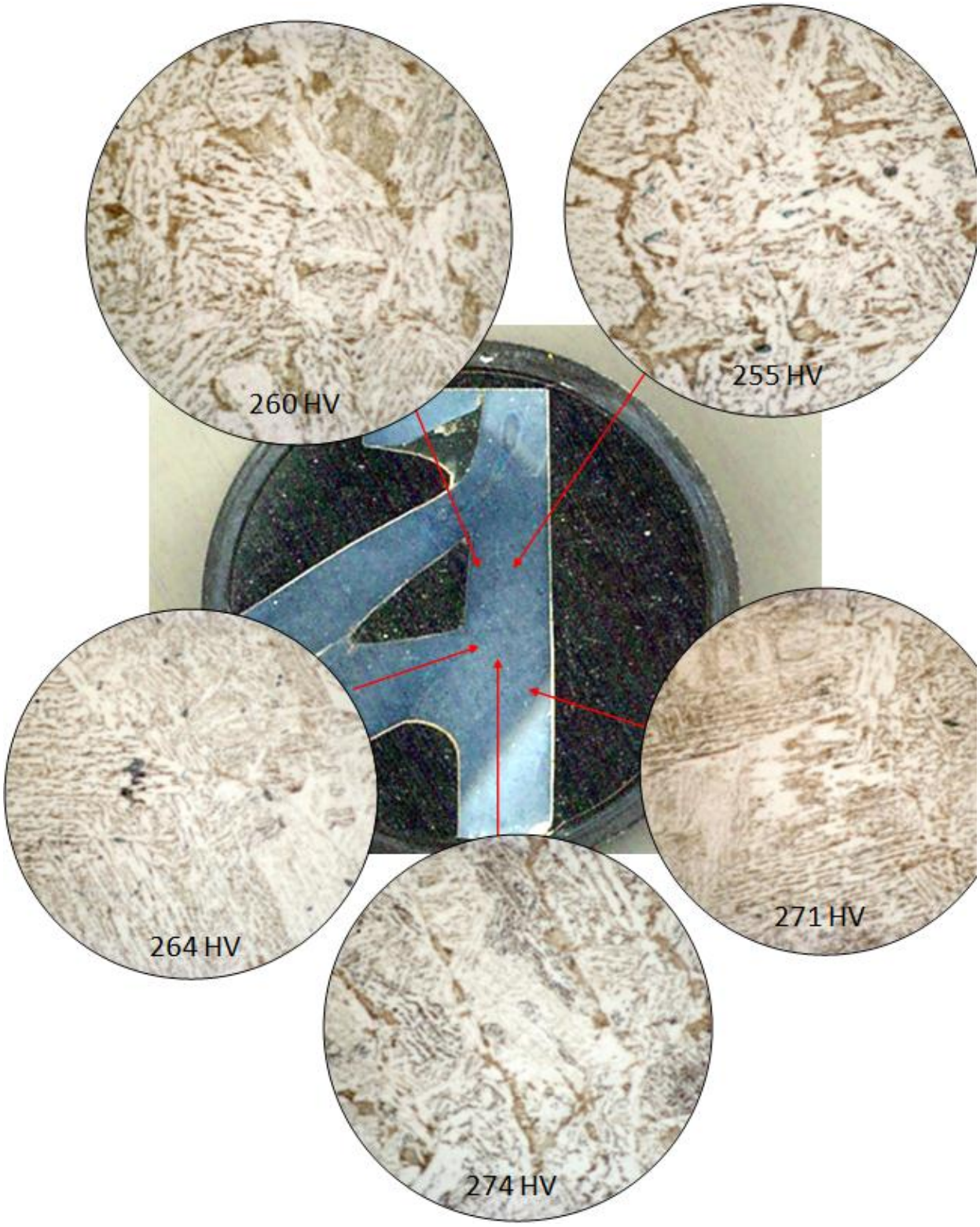
260 HV
255 HV
264 HV
271 HV
274 HV

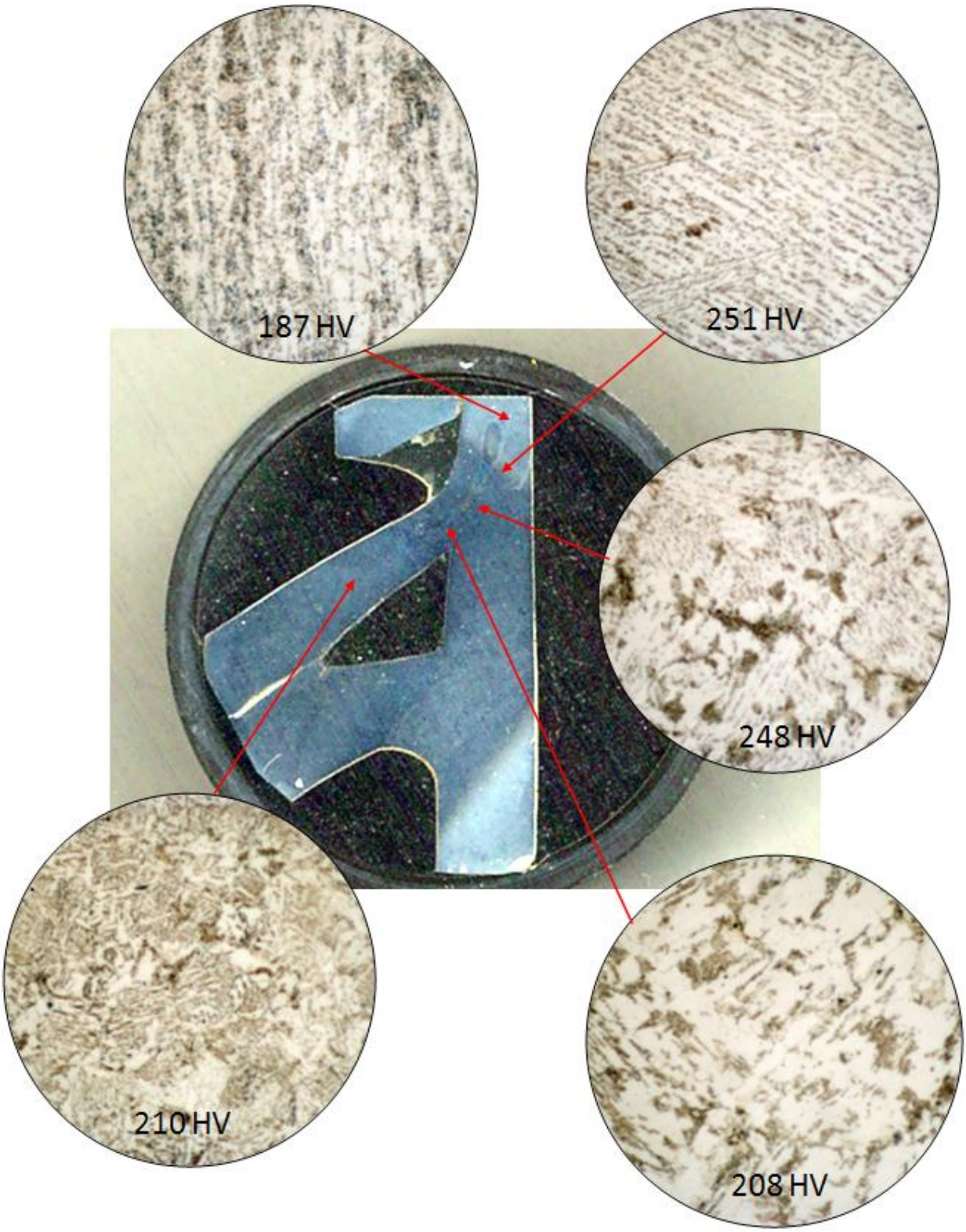
187 HV
251 HV
248 HV
210 HV
208 HV

Fork Blades

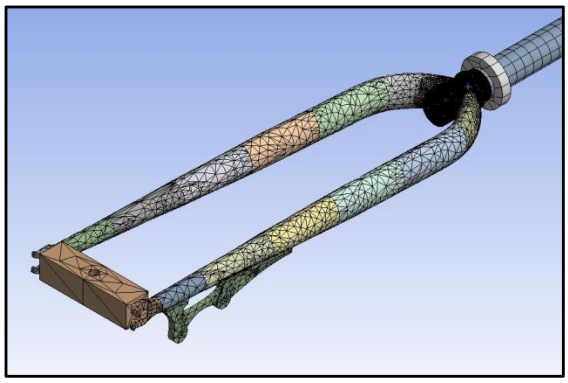

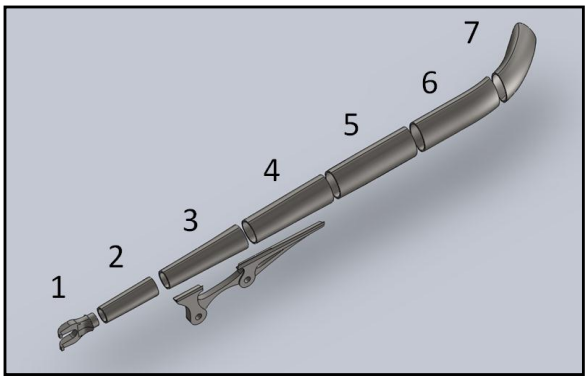

	HK	HV	Average HV	Standard Deviation	Brinell	UTS
1	383.3	375	362	13.00	343	1183.35
	369.1	362				
	355.2	349				
2	392	382	383	21.03	362	1248.9
	418.1	405				
	370.8	363				
3	371.6	364	360	4.04	341	1176.45
	368.3	361				
	363.3	356				
4	383.8	375	370	5.03	350	1207.5
	379.4	371				
	372.5	365				
5	364.9	358	357	1.73	338	1166.1
	361.7	355				
	364.9	358				
6	368	361	362	1.00	343	1183.35
	369	362				
	371	363				
7	391	382	373	10.15	353	1217.85
	384	375				
	369	362				

Average HV	367
Average UTS	1198
Average HB	347
Standard Dev	9.2

Appendix C: Fractographic Analysis of the Fatigue Fracture

Next Page

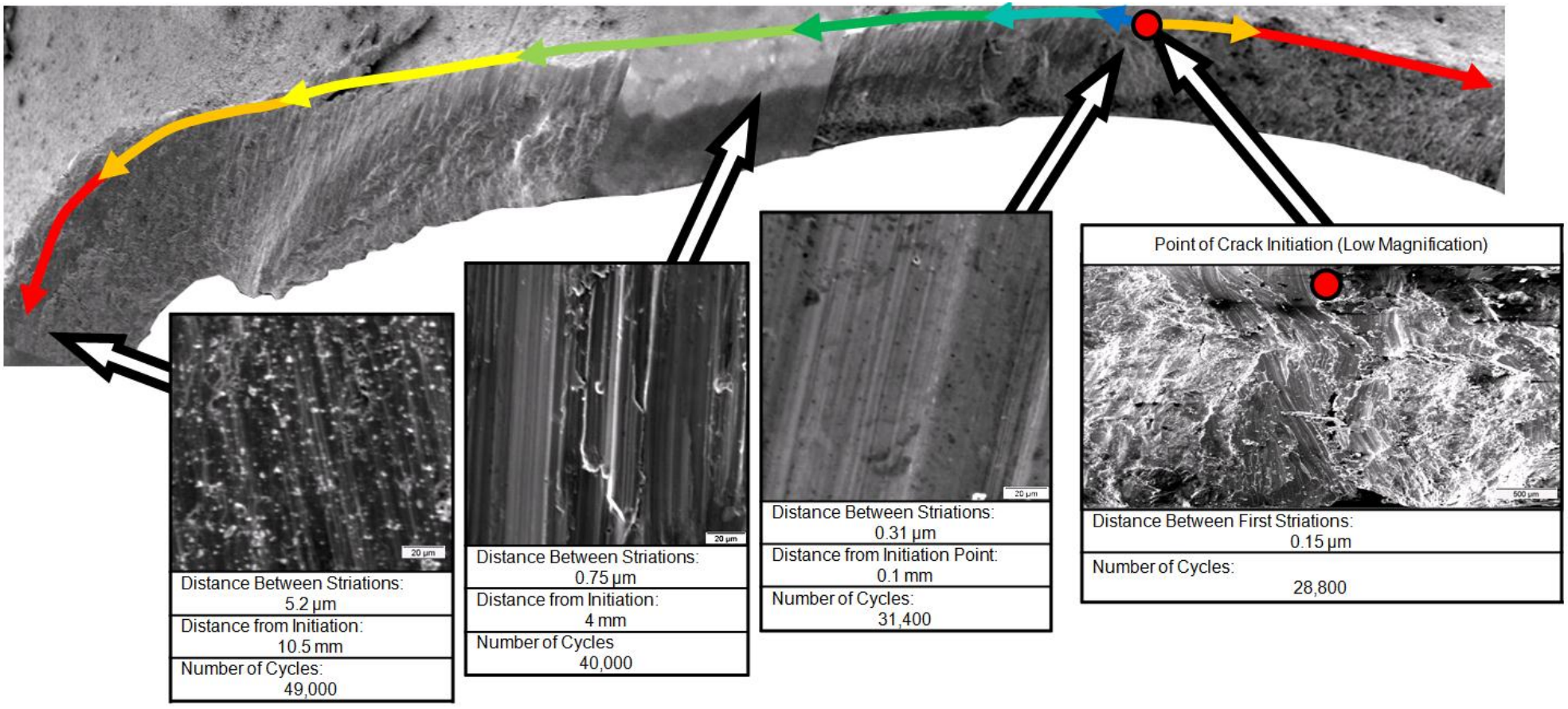
Point of Crack Initiation (Low Magnification)
Distance Between First Striations:
0.15 µm
Number of Cycles:
28,800
Distance Between Striations:
0.31 µm
Distance from Initiation Point:
0.1 mm
Number of Cycles:
31,400
Distance Between Striations:
0.75 µm
Distance from Initiation:
4 mm
Number of Cycles
40,000
Distance Between Striations:
5.2 µm
Distance from Initiation:
10.5 mm
Number of Cycles:
49,000

Appendix D: Chemical Analysis of the Materials

	Fork Blade	Steerer 1	Steerer 2	Steerer Average	Front Face
C	0.336	0.334	0.324	0.329	0.31
Si	0.185	0.232	0.231	0.2315	0.228
Mn	0.79	0.449	0.448	0.4485	0.446
P	0.012	0.011	0.011	0.011	0.01
S	0.005	0.0018	0.0017	0.00175	0.0018
Cr	1.15	0.87	0.87	0.87	0.86
Ni	0.156	0.03	0.028	0.029	0.028
Mo	0.171	0.162	0.159	0.1605	0.159
Al	0.028	0.04	0.04	0.04	0.04
Cu	0.211	0.016	0.016	0.016	0.016
Co	0.017	0.0072	0.0067	0.00695	0.0064
Ti	0.0027	0.0031	0.0031	0.0031	0.0029
Nb	0.026	0.0045	0.0043	0.0044	<0.0010
V	0.067	0.007	0.0065	0.00675	0.0038
W	<0.0070	<0.0070	<0.0070	0	<0.0070
Pb	<0.0010	<0.0010	<0.0010	0	<0.0010
B	<.0002	<.0002	<.0002	0	<0.0002
Sb	0.0053	0.0016	0.0011	0.00135	<0.0010
Sn	0.014	0.0013	0.0011	0.0012	0.0008
Zn	0.0022	0.0024	0.0024	0.0024	0.0028
As	0.019	0.0027	0.0037	0.0032	0.001
Bi	0.0085	0.0079	0.0076	0.00775	0.0072
Ta	0.032	0.023	0.022	0.0225	<0.0070
Ca	0.0006	0.0022	0.0021	0.00215	0.0016
Ce	<0.0020	<0.0020	<0.0020	0	<0.0020
Zr	0.0027	0.0027	0.0023	0.0025	0.0023
La	<0.0003	<0.0003	<0.0003	0	<0.0003
Se	0.023	0.024	0.02	0.022	0.21
N	0.011	0.0059	0.0053	0.0056	0.0086
Fe	96.7	97.8	97.8	97.8	97.8

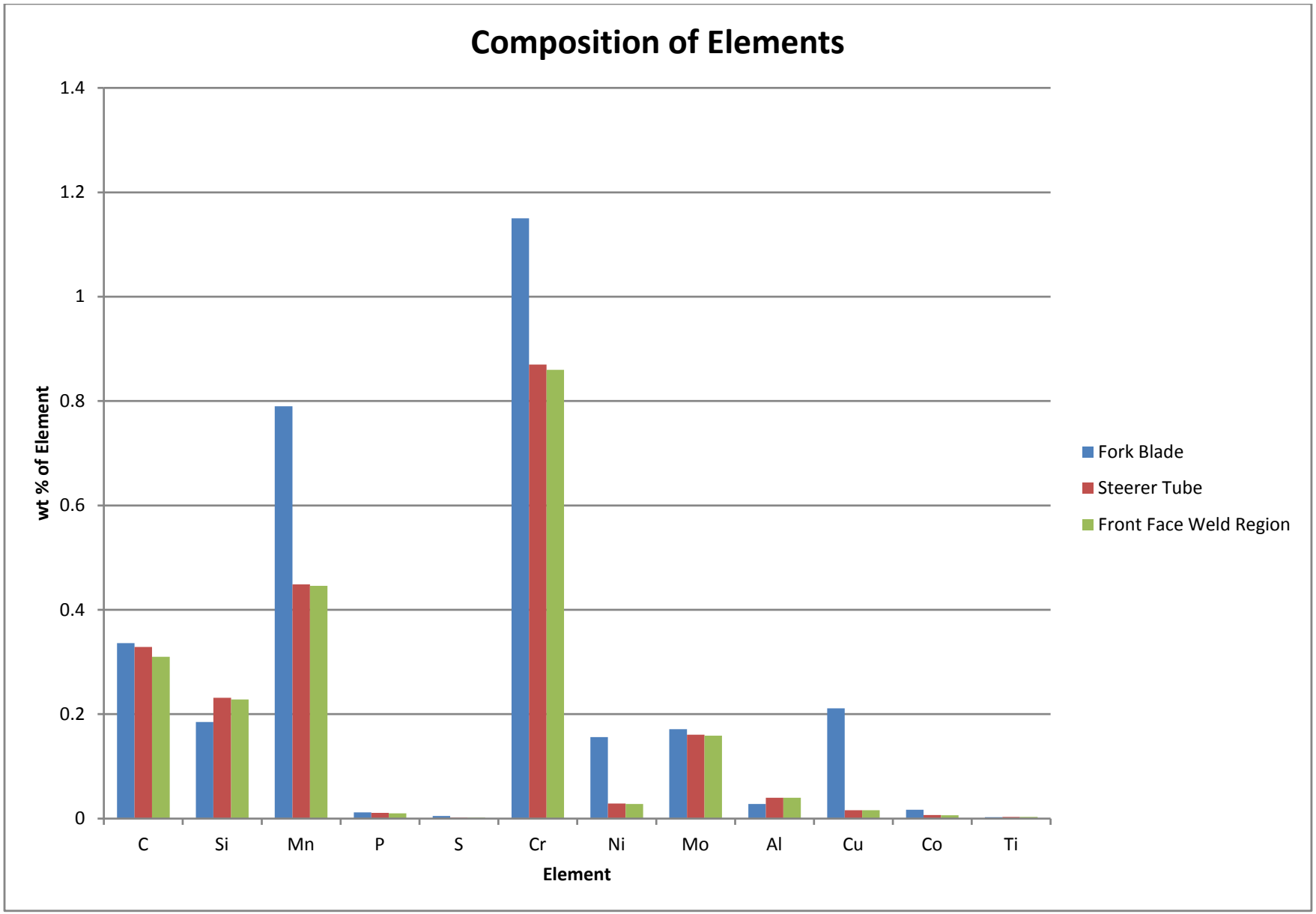
Composition of Elements
1.4
1.2
1
0.8
0.6
0.4
0.2
0
wt % of Element
C
Si
Mn
P
S
Cr
Ni
Mo
Al
Cu
Co
Ti
Element
Fork Blade
Steerer Tube
Front Face Weld Region

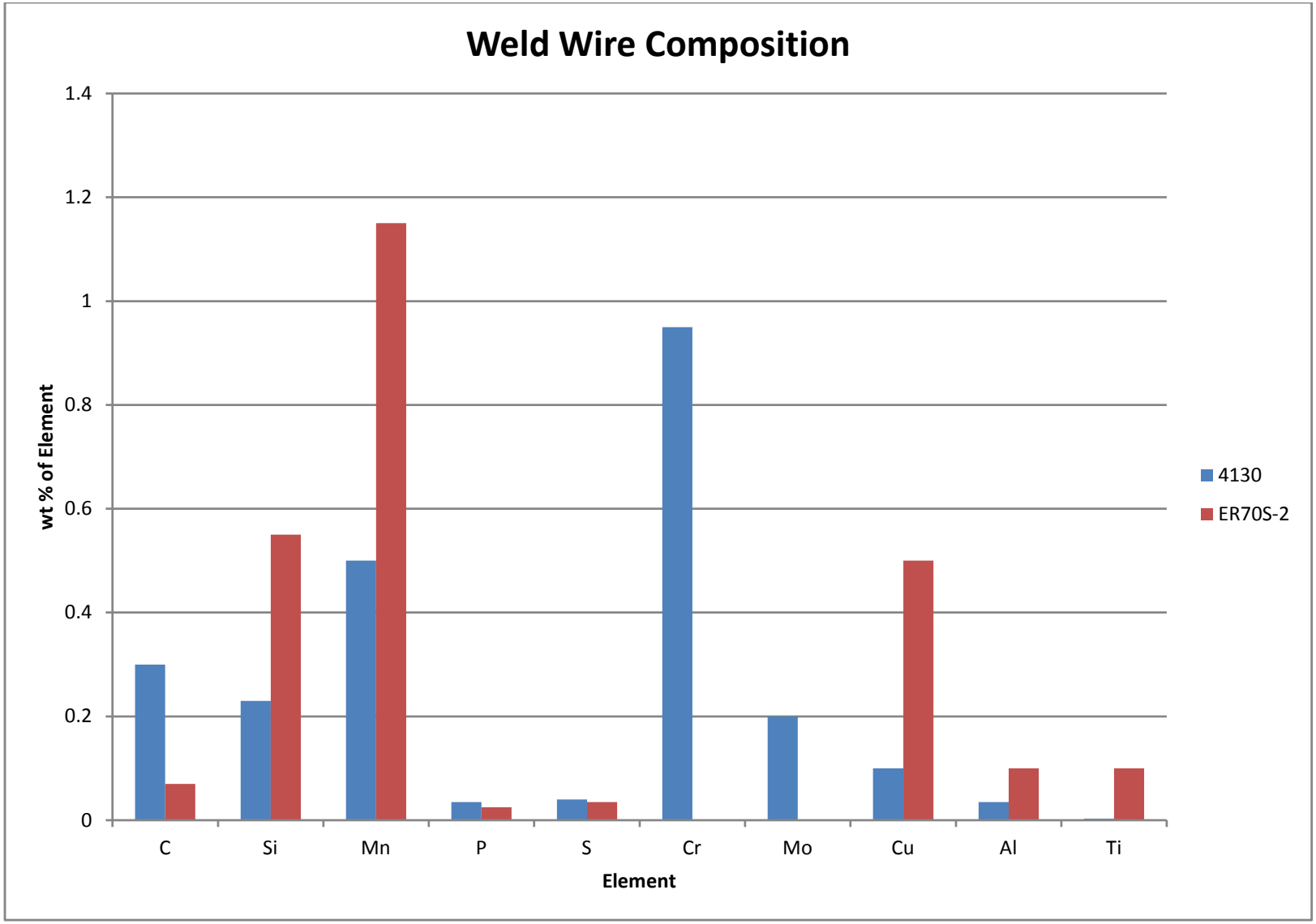
Weld Wire Composition
1.4
1.2
1
0.8
0.6
0.4
0.2
0
wt % of Element
C
Si
Mn
P
S
Cr
Mo
Cu
Al
Ti
Element
4130
ER70S-2

Appendix E: X-Ray Diffraction Results

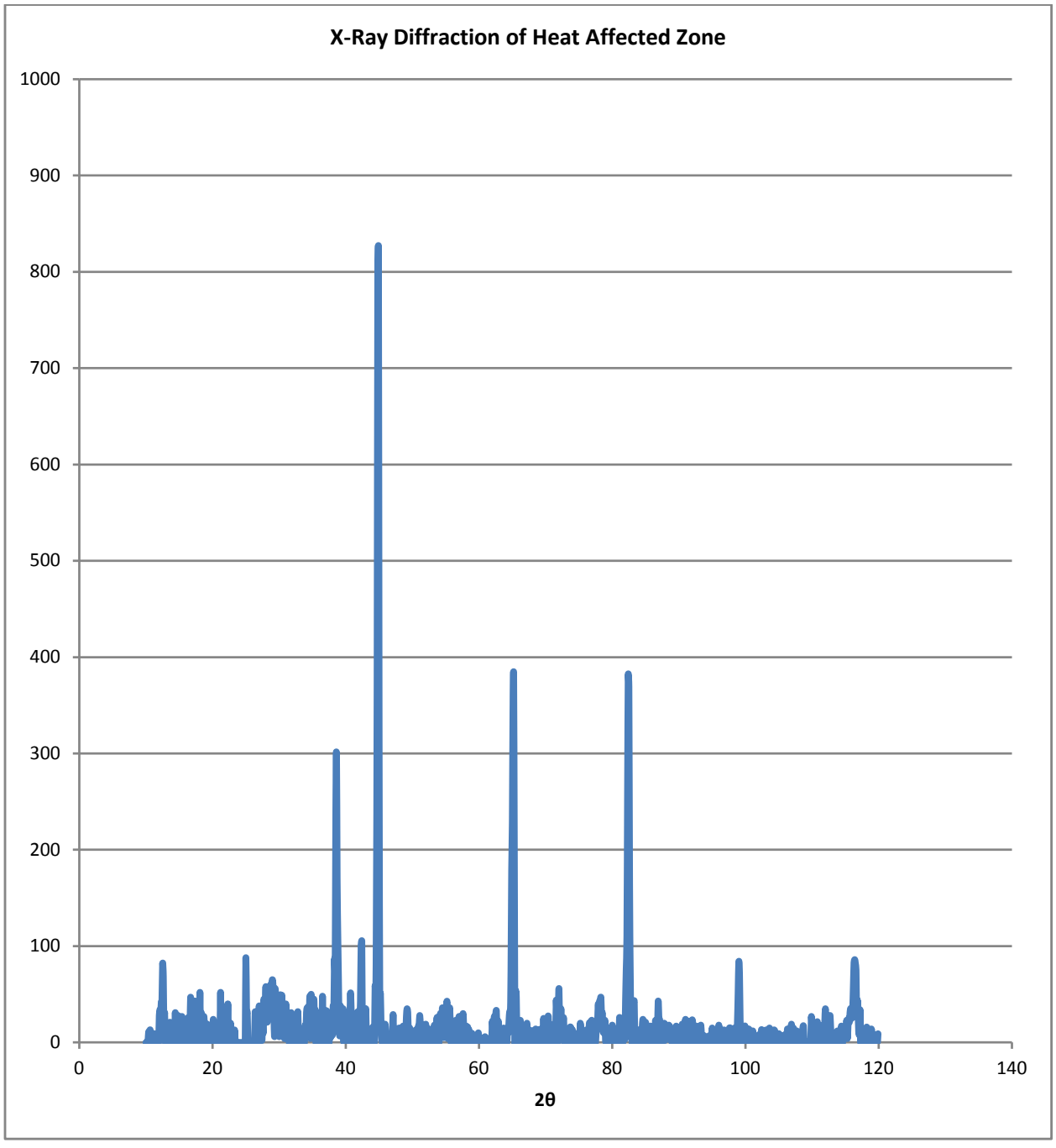

Appendix F: Fe-C Phase Diagram

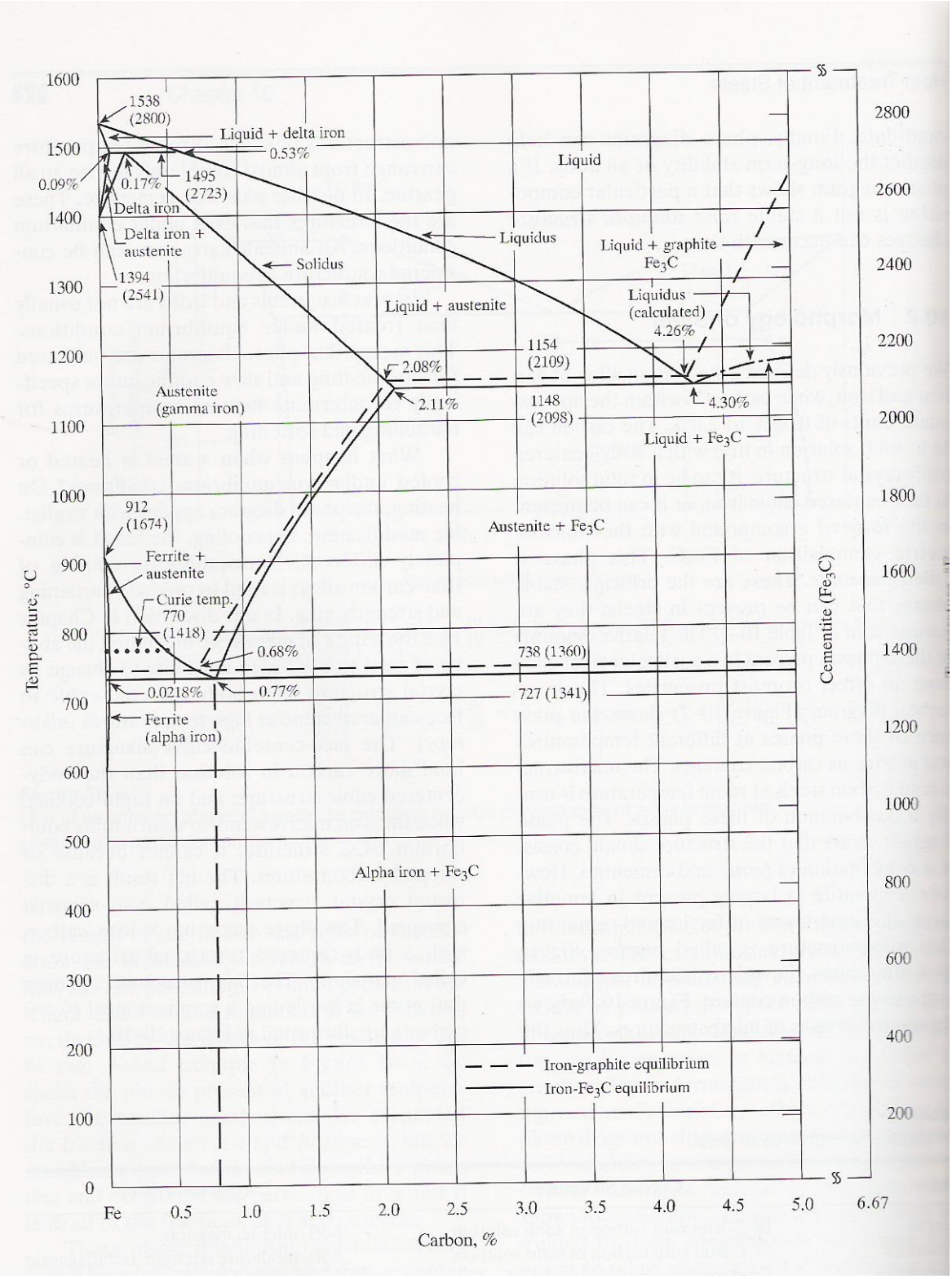

Appendix G: Temperature Evaluation of HAZ

Maximum Temperature Distribution in HAZ

- Calculations assume that at the boundary of the HAZ and unaffected steerer tube the temperature is equal to the eutectic temperature

```
T_E = 1630;
T_i = 20;
α = k / (ρ * C_p);
k = 46;
d = .01;
l = .112;
N_zones = l / d;
t_t = 300;
t_D = t_t / N_zones;
C_p = 470;
ρ = 7850;
Clear[x]
T_xt = (Erf[x / (2 * (α * t_D) ^ .5)]) * (T_i - T_E) + T_E;
```

```
Plot[T_xt, {x, 0, .1}, PlotRange → {0, 2000},
 AxesLabel → {"Distance from Weld (m)", "Temperature (C)"},
 PlotLabel → "Temperature from Weld"]
```

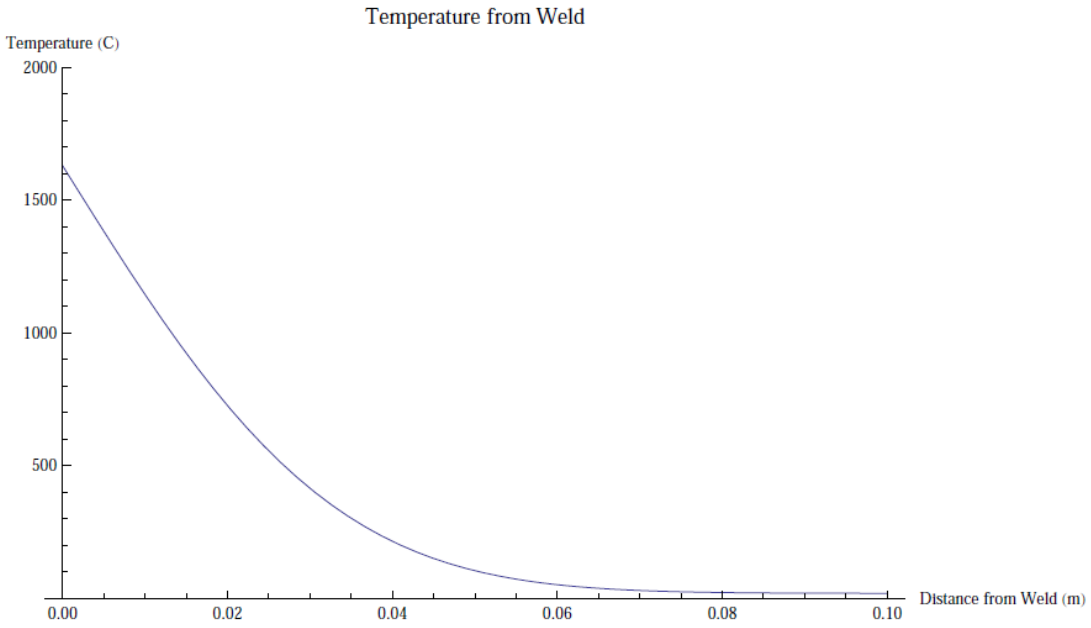

Boundary between HAZ and unaffected ST is at x = 0.02

```
x = 0.02;
```

```
T_xt
```

```
726.802
```

```
Table[T_xt, {x, 0, 0.1, 0.005}]
```

```
{1630., 1383.01, 1145.07, 924.245, 726.802, 556.734,
 415.611, 302.795, 215.912, 151.452, 105.378, 73.6535, 52.6088,
 39.1599, 30.8802, 25.9694, 23.1635, 21.6191, 20.8, 20.3816, 20.1757}
```

Appendix H: Fatigue Properties for FEA

Next Page

Steerer Tube

UTS	6.90E+08	
Sm	1.00E+04	6.21E+08
Se	1.00E+07	3.45E+08
Limit	1.00E+10	3.45E+08

Fork Blade

UTS	1.20E+09	
Sm	1.00E+04	1.08E+09
Se	1.00E+07	5.99E+08
Limit	1.00E+10	5.99E+08

ST HAZ 1

UTS	8.66E+08	
Sm	1.00E+04	7.79E+08
Se	1.00E+07	4.33E+08
Limit	1.00E+10	4.33E+08

FB HAZ 1

UTS	9.14E+08	
Sm	1.00E+04	8.23E+08
Se	1.00E+07	4.57E+08
Limit	1.00E+10	4.57E+08

Weld

UTS	9.52E+08	
Sm	1.00E+04	8.57E+08
Se	1.00E+07	4.76E+08
Limit	1.00E+10	4.76E+08

Dropout

UTS	7.00E+08	
Sm	1.00E+04	6.3E+08
Se	1.00E+07	3.5E+08
Limit	1.00E+10	3.5E+08

DBM

UTS	8.11E+08	
Sm	1.00E+04	7.3E+08
Se	1.00E+07	4.06E+08
Limit	1.00E+10	4.06E+08

Crown

UTS	7.83E+08	
Sm	1.00E+04	7.05E+08
Se	1.00E+07	3.92E+08
Limit	1.00E+10	3.92E+08

Braze

UTS	3.50E+08	
Sm	1.00E+04	3.15E+08
Se	1.00E+07	1.75E+08
Limit	1.00E+10	1.75E+08

Steerer Tube Upper

UTS	9.31E+08	
Sm	1.00E+04	8.38E+08
Se	1.00E+07	4.66E+08
Limit	1.00E+10	4.66E+08

FB1

UTS	1.18E+09	
Sm	1.00E+04	1.06E+09
Se	1.00E+07	5.92E+08
Limit	1.00E+10	5.92E+08

FB2

UTS	1.25E+09	
Sm	1.00E+04	1.12E+09
Se	1.00E+07	6.25E+08
Limit	1.00E+10	6.25E+08

FB3

UTS	1.18E+09	
Sm	1.00E+04	1.06E+09
Se	1.00E+07	5.88E+08
Limit	1.00E+10	5.88E+08

FB4

UTS	1.21E+09	
Sm	1.00E+04	1.09E+09
Se	1.00E+07	6.04E+08
Limit	1.00E+10	6.04E+08

FB5

UTS	1.17E+09	
Sm	1.00E+04	1.05E+09
Se	1.00E+07	5.83E+08
Limit	1.00E+10	5.83E+08

FB67

UTS	1.20E+09	
Sm	1.00E+04	1.08E+09
Se	1.00E+07	5.99E+08
Limit	1.00E+10	5.99E+08

Appendix I: Calculations for Flow Through Pneumatic Cylinder

Definition of Variables

Rd= Rod Diameter

$Rd := \frac{5}{8}$

s= Stroke

$s := 6$

b= Cylinder Bore Diameter

$b := 1.5$

d= diameter of fitting

$d := \frac{7}{16}$

$F := 166$

$P2 := 14.4$

$P3 := 14.4$

Equations

$A1(b) := \pi \cdot \left(\frac{b^2}{4}\right)$

$A2(b, Rd) := \pi \left(\frac{b^2}{4}\right) - \pi \left(\frac{Rd^2}{4}\right)$

$V1(b, s) := A1(b) \cdot \frac{s}{2}$

$V2(b, Rd, s) := A2(b, Rd) \cdot \frac{s}{2}$

$P1(b, F) := \frac{F}{A1(b)} + 14.4$

$V3(b, Rd, s, F) := \frac{(P1(b, F) \cdot V1(b, s) + P2\, V2(b, Rd, s))}{P3}$

$Vf(b, Rd, s, F) := 2 \cdot V3(b, Rd, s, F)$

$Afit(d) := \pi \frac{d^2}{4}$

$V1 := V1(b, s)$

$V2 := V2(b, Rd, s)$

$P1 := P1(b, F)$

$v(b, Rd, s, F, d) := \frac{Vf(b, Rd, s, F)}{Afit(d)\, 12}$

Results

$A1(b) = 1.767$

$A2(b, Rd) = 1.46$

$V1 = 5.301$

$V2 = 4.381$

$P1 = 108.337$

$V3(b, Rd, s, F) = 44.266$

$Vf(b, Rd, s, F) = 88.532$

$Afit(d) = 0.15$

$v(b, Rd, s, F, d) = 49.076$ ft/s